LAPPEENRANTA UNIVERSITY OF TECHNOLOGY

LUT School of Energy Systems

LUT Mechanical Engineering

Shahriar Afkhami

INVESTIGATION ON THE WELDABILITY OF COLD-FORMED ULTRA-HIGH STRENGTH STEELS S700MC AND S1100

Examiners: Prof. Timo Björk

           M.Sc. Riku Neuvonen

ABSTRACT

Hollow sections and cold-formed steels have a key role in modern structures and machinery. In addition, to benefit from full potentials of cold-formed steels, it is usually required to weld them to other parts of the structure. However, data provided by relative standards, such as Eurocode 3, do not cover newly developed high strength grades of steels, including Ultra-high strength steels. Thus, further study is necessary to complete available data in standards. Regarding this matter, having a good weldability for cold-formed ultra-high strength steels seems to be vital for development for contemporary steel structures. Thus, newly developed ultra-high strength steels S700MC and S1100 were selected to be investigated in this study. To do so, bended base metals with different levels of cold-forming were welded to straight (virgin) steel plates. Next, welded joints were investigated via microstructural analysis, hardness measurement, tensile test, and Charpy impact test to assess the weldability of cold-formed base metals. Results show that final joints had acceptable characteristics, and cold-formed base metals showed good weldability. However, this conclusion was true if the pre-strain values recommended by Eurocode 3 and manufacturer were satisfied. Beyond that criteria, some premature failures occurred in the cold-formed materials after welding.

ACKNOWLEDGEMENTS

TABLE OF CONTENTS

APPENDIX

      Appendix I: macrographs of fractured tensile specimens.

LIST OF SYMBOLS AND ABBREVIATIONS

A	Bending angle
A_{c1}	Eutectoid transformation temperature of steels
A_g	Gross cross-section
Ar	Argon
C_{eq}	Carbon equivalent
CE_I	Carbon equivalent factor 1
CE_{II}	Carbon equivalent factor 2
CO_2	Carbon dioxide
d'	Ligament size of sub-size specimen for Charpy test
D'	Ligament size of normal specimen for Charpy test
e'	Fracture energy density of sub-size specimen
E'	Fracture energy density of normal specimen
F_2	Dimensionless shape factor to calculate welding heat input
F_3	Dimensionless shape factor to calculate welding heat input
F_u	Tensile strength of virgin material
F_y	Yield strength of virgin material
F_{ya}	Average yield strength of a cross-section
F_{yb}	Basic yield strength
F_{yc}	Yield strength of bended material
I	Welding electric current
K	K-factor
k	Numerical coefficient for calculating the average yield strength of a cross-section
K'	Energy of rupture
n	Number of bended members of a steel structure
P_{cm}	Cold cracking sensitivity index
P_{SR}	Reheat cracking susceptibility index 1
Q	Welding heat input
R_s	Reheat cracking susceptibility index 2

r	Bending inner radius
s'	Cross sectional area of sub-size specimen for Charpy test
S'	Cross sectional area of normal specimen for Charpy test
t	Thickness
t_o	distance between inside surface of the bended material and its neutral axis
T_o	Preheat temperature
$t_{8/5}$	Cooling time from 800°C to 500°C
U	Welding electrical potential
v	Welding speed
$\Delta G1$	Reheat cracking susceptibility index 3
ε	Thermal efficiency of a welding procedure
AHSS	Advanced high-strength steels
AWS	American welding society
BA	Bending allowance
CEN	Carbon equivalent number
CET	Equivalent carbon content
CEV	Carbon equivalent value
CGHAZ	Coarse grain HAZ
DBTT	Ductile to brittle transition temperature
FGHAZ	Fine grain HAZ
FZ	Fusion zone
HAZ	Heat affected zone
HSLA	High-strength low-alloy
HSS	High strength steel
HV	Hardness Vickers
ICHAZ	Intercritical HAZ
LW	Laser welding
MAG	Metal active gas
NGLW	Narrow gap laser welding
SCHAZ	Subcritical HAZ
SEM	Scanning electron microscopy

SMAW	Shielded metal arc welding
TIG	Tungsten inert gas
TRIP	Transformation induced plasticity
TWIP	Twinning-induced plasticity
UHSS	Ultra-high strength steel
(U)HSSs	High strength steels and ultra-high strength steels

1   INTRODUCTION

Construction, manufacturing, and assembling of steel structures are currently resource-intensive industries. In other words, they induce elevated levels of numerous stresses on natural resources and also introduce a huge amount of various waste materials and pollution into nature. To avoid these negative effects, material preservation and sustainability are two of the crucial factors dealing with contemporary constructional and industrial projects. Hence, it is of utmost importance to use environmentally friendly materials with closed processing and consumption cycles in modern structures. (Crawford 2011, pp. 1-24; Aksel & Eren 2015, p. 51.)

Steel is one of the eco-friendly and versatile materials, which can be reprocessed and recycled without a major loss in its quality. It is widely used in civil structures and construction due to its strength, performance, and economical advantages. Furthermore, it is a durable, recyclable, and nature-friendly material. (Aksel & Eren 2015, p. 51.) According to their characteristics and applications, steels can be divided into several groups, such as structural steels, wear resistant steels, stainless steels etc. One of these groups consists of steels for structural purposes. These steels are known as structural steels and can be classified as carbon steels, high-strength low-alloy (HSLA) steels, heat treated carbon steels and heat treated constructional alloy steels. Typical stress-strain curves and mechanical properties of these steels are presented in figures 1 and 2 for comparison. (Brockenbrough & Merritt 1999, p.1.)

By development of steel manufacturing and processing technologies, advanced high-strength steels (AHSS) have emerged as a new generation of HSLA steels (Guo et al. 2016, pp. 1-2). Mandal et al. (2016, p. 126) categorized these steels into three distinct generations. The first generation comprises ferrite-based dual phase steels, martensitic steels and transformation induced plasticity (TRIP) steels. The second generation is austenite-based and high-manganese twinning-induced plasticity (TWIP) steels. Finally, the third generation is based on multiphase microstructures.
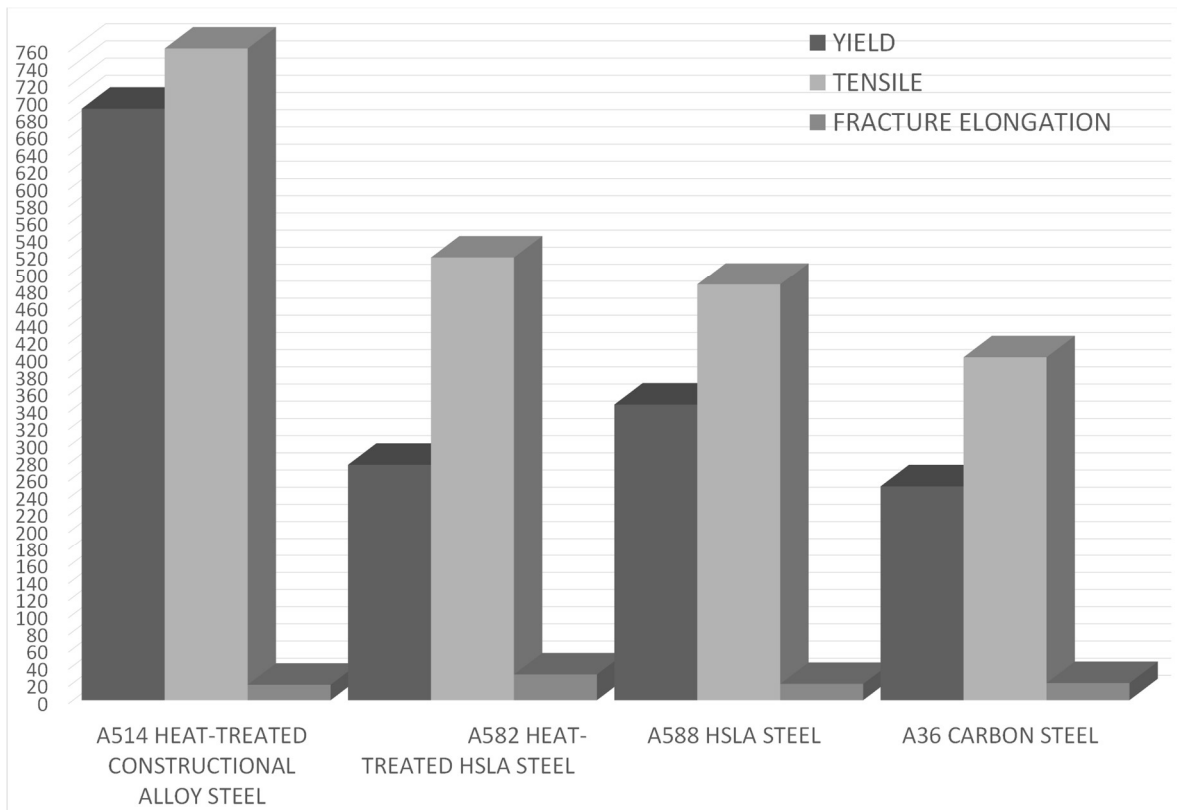
Figure 1. Typical mechanical properties of some structural steels (data from Brockenbrough & Merritt (1999, p. 2) and AZOM (2018)).
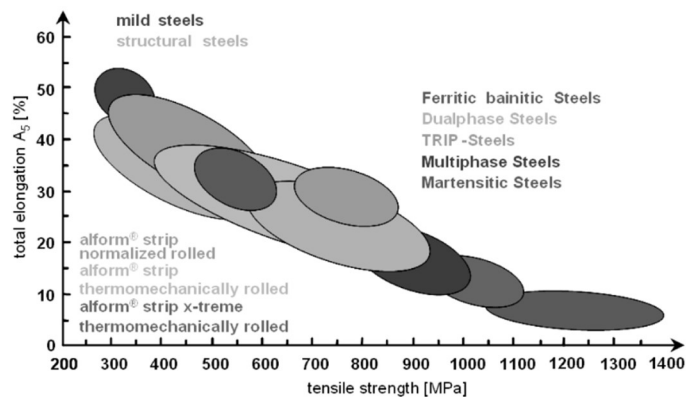
Figure 2. Strengths and fracture elongations of different classes of structural steels, HSLA and ultra-high strength steels (Rauch et al. 2012, p. 2; reprint with permission).

The third generation, having yield strengths up to 950 MPa, are also known as ultra-high strength steels (UHSS); However, strength levels of these steels have currently reached values far higher than 950 MPa. Thus, the term "ultra-high strength steels" generally refers to structural steels with very high levels of strengths. (Maity & Kawalla 2011, p. 309.) According to Porter (2015, p. 2), high strength (HSS) and ultra-high strength (UHSS) steels

provide a good solution for saving energy, preserving raw materials, and reducing carbon dioxide emissions.

These steels have a significant role in modern transportation systems and every other application where the weight of the target structure is a critical factor, especially due to its stability and mobility. Higher strength levels of manufacturing materials lead to the possibility of using thinner walls, applying smaller weld beads, replacement of welds by mechanical joints, and cost savings in fabrication. Therefore, UHSSs have got a major role in industries such as automobile manufacturing and construction through the past recent decades. (Porter 2015, pp. 1-2.) This achievement is also due to the improvements of safety, economical and environmentally friendly aspects of modern manufacturing (Matsuoka, Hasegawa & Tanaka 2007, p. 13). Furthermore, according to figure 3, UHSSs facilitate sustainable construction by increasing the energy efficiency and the durability of final product (Aksel & Eren 2015, p. 51).
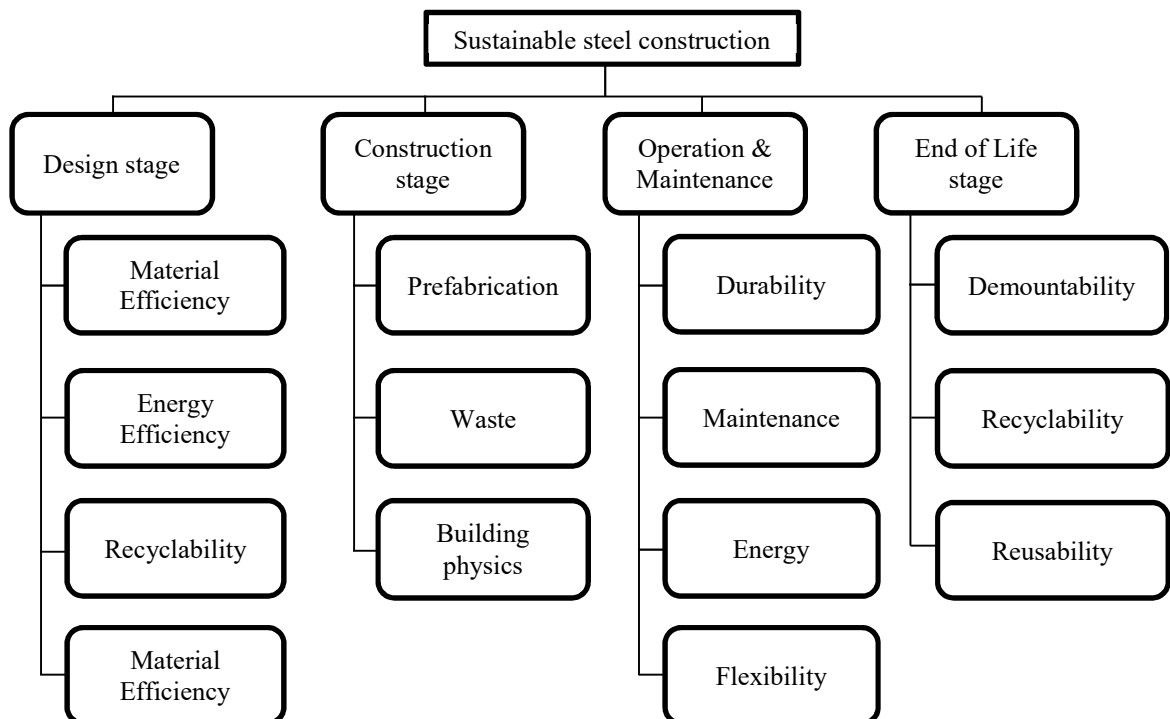

Figure 3. Effective parameters of sustainability in steel construction according to Aksel and Eren (2015, p.51).

Various structural steels are used in the forms of cold-formed or tubular hollow sections to improve their efficiency, applicability, and versatility (Ritakallio & Björk 2014, p. 107). Furthermore, Hollow sections made of high-strength and ultra-high strength steels are essentials of energy absorbent parts in automobile industry. These materials improve passenger's safety and reduce weight and fuel consumption of vehicles. However, these applications are not possible without joining these sections into each other. (Hamedon, Mori & Abe 2014, p. 2074; Porter 2015, pp. 1-3)

Welding is the most cost-effective and common joining method for UHSSs, which can produce satisfying strong joints without any defects in steel structures. Among diverse types of welding processes, gas metal arc welding (GMAW) is capable of continuous deposition of welds with low hydrogen content. By exploitation of the shielding gas, GMAW does not need any slag removal between its subsequent runs. Therefore, GMAW is a fast, economic, and simple welding process, which is highly approved for different industrial purposes. (Porter 2015, p. 3; Kou 2003, p. 19-22; Shome & Tumuluru 2015, p. 5)

1.1   Objectives, research problem and research questions

Numerous shapes of cold-formed steels, such as hollow sections, are widely used in steel construction and structures; however, their weldability and post welding reliability are still in question due to the potential negative effects of cold-forming and welding processes. For example, one of these negative effects is the loss of toughness due to the strain ageing near the welded joints. This loss results in an increase in the ductile to brittle transition temperature (DBTT) and causes premature failures of structures made of hollow sections, especially at low ambient temperature. (Ritakallio & Björk 2014, pp. 107-115)

Although some restrictions and regulations are considered to perform welding near the cold-formed areas of steels by Eurocode 3, part EN1993-1-8, these rules are approved only for typical steel grades up to high-strength steels. Hence, welding of cold-formed ultra-high strength steels requires more investigation to examine the suitability of these rules for UHSSs. This issue is of utmost importance since the types and magnitudes of appropriate loads for a welded structure are limited to the capacity of its critical joints. (Ritakallio & Björk 2014, pp. 107-115)

Currently, cold-formed steels and hollow sections made of high-strength and ultra-high strength structural steels are widely used in the construction and automobile industries. These types of steel are more energy efficient, economical, and highly effective for weight reduction of steel structures and automobiles bodies. Thus, Standards such as EN 1993-1-10 and EN 1993-1-12 aims to stablish some criteria for welding HSSs with strength ranges up to 700 MPa. To do so, these standards present some criteria correlating permissible material thickness and its Charpy energy to give a measure for the quality of the welded. In addition, they provide some additional rules for welding steels with strength values as high as 700 MPa. However, literature and European standards still lack data on welding criteria of cold-formed sections made of ultra-high strength steels, especially steels with strength values higher than 700 MPa. Thus, obtaining and providing more comprehensive and accurate data are presently in high demand.

This study tends to evaluate and investigate effects of prior cold work and cold-forming on the final characteristics of welded joints between UHSSs. In this study, bending is the process used to induce effects of cold work on the steel plates. The evaluation is carried out by comparing mechanical properties of the welded specimens with different degrees of cold-forming (bending). This research aims to answer three main questions; firstly, what are the suitable criteria for welding cold-formed UHSSs? Secondly, are the design rules and regulation in EN1993-1-8 applicable for UHSSs? Finally, what are the differences between welded cold-formed UHSSs and original ones? In conclusion, the essence of this work is summarized in the answers of the questions.

1.2   Framework

The conceptual framework of this research and flowchart of its procedures are presented in table 1 and figure 4 respectively.

Table 1. The conceptual framework of the research

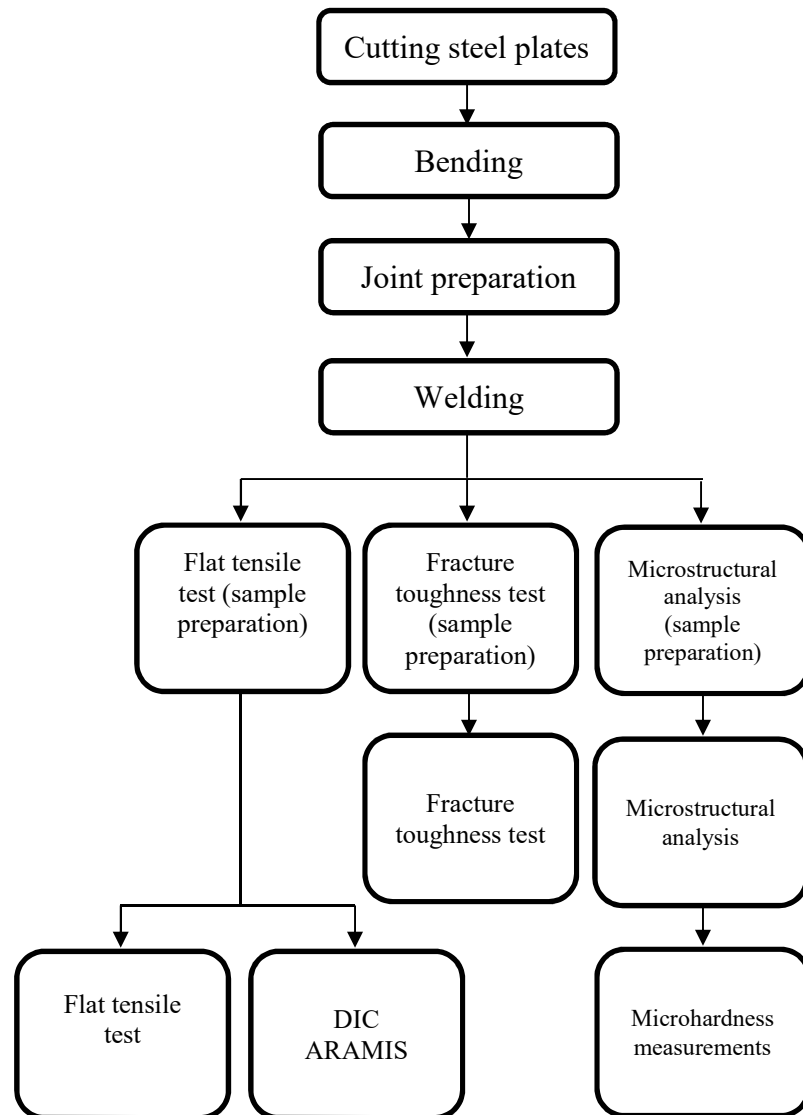| Scope	Variable	Domain of influence	Type of influence				
Weldability of cold-formed ultra-high strength steels	Degree of cold-forming (bending radius)	Mechanical properties	Yield strength	Tensile strength	Hardness	Notch toughness	Fracture mechanism
		Microstructure	Types of phases in different areas				

Figure 4. Successive steps of the research.

2 LITERATURE REVIEW

High strength and ultra-high strength steels and their welding procedures have been subjects of many studies recently. As time goes on, steel manufacturing technologies have been developed, and manufacturing stronger steels with higher levels of toughness and ductility has become possible for steel manufacturers worldwide. Thus, available literature about welding these steels consist of several steel grades and different welding procedures.

2.1   Ultra-high strength steels

Structural steels with very high yield and tensile strengths are referred as ultra-high strength steels. Although these steels have been used in automobiles and steel structures for a long time, there is no universally accepted strength range for them yet. This issue might be due to the continuous development of their grades and strengths. Currently, the yield strength of commercial UHSSs has reached up to 1400 MPa and it is still in development. Unique mechanical properties of UHSSs are usually achieved by grain refinement during their austenitizing process and further thermo-mechanical processing. (Maity & Kawalla 2011, p. 309.)

In comparison to high-strength steels, UHSSs undergo some additional hardening processes through their manufacturing procedures to achieve higher levels of strengths. These processes include different multi-stage cooling and rolling patterns to reach desired final microstructure and strength. The desired microstructure consists of various phases including irregular ferrite, bainite, martensite, remaining austenite, or their combination. Furthermore, the strengths of UHSSs depend on their carbon content and prior austenite grain size, while their formability depends on their second phase constituent (for example, volume ratio of self-tempered martensite to the background phase). (Spindler et al. 2005, pp. 1-19.)

2.1.1 S700MC

S700MC is a hot-rolled, high strength structural steel with a bainitic microstructure. In addition, it has a minimum yield strength of 700 MPa and acceptable formability. (Górka 2016, pp. 617-618.) Due to its high strength and formability, it is usually used in load bearing structures and components. Chemical composition and mechanical properties of S700MC, according to its manufacturer, are presented in table 2 and table 3 respectively. (SSAB 2016a, p. 33.)

Table 2. Chemical composition of S700MC (SSAB 2016a, p. 34).

steel grade	C (max %)	Si (max %)	Mn (max %)	P (max %)	S (max %)	Al (max %)	Nb (max %)	V (max %)	Ti (max %)
S700MC	0.120	0.210	2.100	0.020	0.010	0.015	0.090	0.200	0.150
CEV= 0.39 CET= 0.25									

Table 3. Mechanical properties of S700MC at ambient temperature (SSAB 2016a, p33).

Thickness (mm)	Minimum yield strength (MPa)	Tensile strength (MPa)	Minimum elongation (%)	Impact toughness at -40 ℃ (J)
2-10	700	750-950	12	27

2.1.2 S1100

S1100 is a hot-rolled ultra-high strength structural steel suitable for cold-forming with minimum yield strength of 1100 MPa. It is usually used in load-bearing structures. General requirements of S1100 according to its manufacturer are presented in table 7 and table 8. (SSAB 2016a, p. 72.)

Table 4. Chemical composition of S1100 (SSAB 2016a, p. 73).

steel grade	C (max %)	Si (max %)	Mn (max %)	P (max %)	S (max %)	Cr (max %)	Cu (max %)	Ni (max %)	Mo (max %)	B (max %)
S1100	0.210	0.500	1.400	0.020	0.005	0.800	0.300	3.000	0.700	0.005
CEV= 0.70 CET= 0.40										

Table 5. Mechanical properties of S1100 at ambient temperature (SSAB 2016a, p.72)

Thickness (mm)	Minimum yield strength (MPa)	Tensile strength (MPa)	Minimum elongation (%)	Impact toughness at -40 ℃ (J)
4.0-4.9	1100	1250-1550	8	-
5.0-40.0	1100	1250-1550	10	27

2.2   Weldability of (U)HSSs

Typical problems associated with the welding of (U)HSSs are cracking of heat affected zone (HAZ), HAZ softening, toughness deterioration and lack of ductility. Majority of these difficulties arise from using inappropriate heat inputs, cooling rates and wrong material selection. Possibility and frequency of the occurrence for these problems define the essence of weldability of steel. (Tasalloti, Kah & Martikainen 2017, pp. 29-30.) Many of these problems are directly related to carbon content of steels, which is one of the basic parameters defining their weldability. In addition, the carbon content of (U)HSSs controls their strength and hardness at their as-quenched state. (Klein et al. 2012, pp. 108-112.)

Other alloying elements are also influential on the weldability of steel. Elements such as manganese, nickel, chromium, and molybdenum prevent any unwanted phase transformation prior to martensite formation in this material. In addition, some of the precipitate former elements hinder grain growth and its consequence hardness drop during any heating and annealing process. (Klein et al. 2012, pp. 108-112.) Regarding (U)HSSs, it is possible to minimize the amount of these alloying elements and the carbon contents to improve their weldability. In addition to controlling the alloying elements, it is practical to reduce their susceptibility to cold cracking via optimized thermomechanically controlled processes. (Rauch et al. 2012, p. 103.)

Weldability of (U)HSSs is generally defined by two factors. The first one is the absence of microstructural defects, and the other one is the suitability of their mechanical properties after welding. (Rauch et al. 2012, p. 103.). Lack of weldability might show itself as cracking and deterioration of mechanical properties after welding, which is usually caused by excessive grain growth. However, steels produced by thermomechanical processes are not very sensitive to cold cracking, and they do not have a high tendency to grain growth due to their low contents of carbon and other alloying elements. Regarding (U)HSSs, HAZ softening and embrittlement are usually two serious concerns of welding these steels. (Jiang, Jhang, Chen 2016, p. 705.)

2.2.1 Hardenability and weldability

According to (Jiang et al. 2016, p. 707), it is possible to evaluate hardenability and weldability of low carbon steels by calculating their carbon equivalent number (CEN) via the formula presented by Suzuki and Yurioka (equation 1). Steels with CEN lower than 0.45% are expected to have good weldability.

$$\text{CEN} = C_{wt\%} + 0.5 \left(\frac{Si_{wt\%}}{24} + \frac{Mn_{wt\%}}{6} + \frac{Cu_{wt\%}}{15} + \frac{Ni_{wt\%}}{20} + \frac{Cr_{wt\%} + Mo_{wt\%} + Nb_{wt\%} + V_{wt\%}}{5} + 5B_{wt\%} \right) \tag{1}$$

2.2.2 Susceptibility to cold cracking

By calculating CEN and carbon content, it is possible to investigate the susceptibility of cold cracking as shown in figure 5 (Abson & Rothwell 2013, pp. 437-473). For steels with niobium contents more than 0.04 wt%, such as S700MC, cold cracking susceptibility also can be evaluated by cold cracking sensitivity index (P_{cm}) calculated by equation 2. Steels with P_{cm} lower than 0.20% are less sensitive to cold cracking. (Jiang et al. 2016, p. 707.)

$$P_{cm} = C_{wt\%} + \frac{Si_{wt\%}}{30} + \frac{Mn_{wt\%} + C_{wt\%} + Cr_{wt\%}}{20} + \frac{Mo_{wt\%}}{15} + \frac{Ni_{wt\%}}{60} + \frac{V_{wt\%}}{3} + \frac{Nb_{wt\%}}{2} + 5B_{wt\%} \tag{2}$$

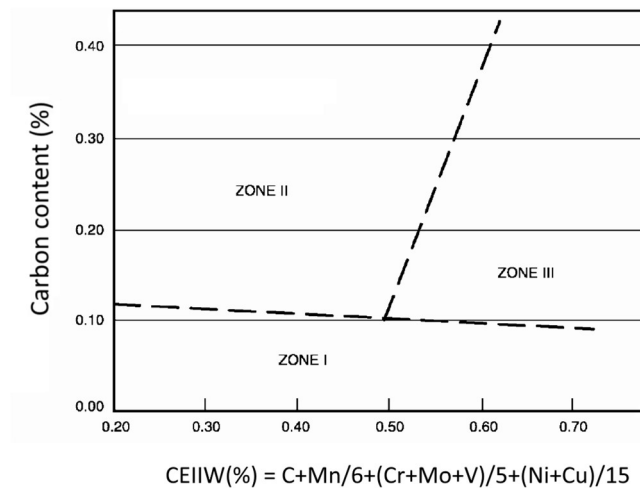CEIIW(%) = C+Mn/6+(Cr+Mo+V)/5+(Ni+Cu)/15

Figure 5. Influence of carbon content and CEN on the susceptibility of steels to HAZ cold cracking according to AWS D1.1: zone I has good weldability; zone II is weldable with caution; and, zone III is difficult to weld (Yurioka 2004, p. 22; reprint with permission).

Estimation of hardness value from chemical composition is another method to evaluate susceptibility of steels to cold cracking and excessive brittleness. This value should not exceed 350 HV for structural steels, such as S700MC and S1100, to avoid any type of cold cracking. (Garašić et al. 2010, p. 328.) In addition, the expression for the maximum hardness value (HV_{max}) can take into account both measures of carbon content and cooling rate via equations 3 to 10 (Nicholas & Abson 2008, pp. 18-19):

$$t_m = 10^{\frac{611.3C_{wt\%}+605.7C_{eq}-239}{1009.5C_{wt\%}+52.8}} \tag{3}$$

$$t_b = 10^{\frac{1413.3C_{wt\%}+30\ .7C_{eq}-3}{1009.5C_{wt\%}+52.8}} \tag{4}$$

For $t_m \leq t_{8/5} \leq t_b$:

$$HV_{max} = 0.5 \times \left\{2019 \times \left[C_{wt\%} \times \left(1 - 0.5\log t_{8/5}\right) + 0.3 \times \left(C_{eq} - C_{wt\%}\right)\right]\right\} + \left[66 \times \left(10.8\log t_{8/5}\right)\right] + 0.5 \times \left\{406C_{wt\%} + 164CE_I + 183 - (369C_{wt\%} - 149CE_I + 100) \times \tan^{-1}\frac{\log t_{8/5}-2.822CE_{II}+0-262}{0.526-0.195CE_{II}}\right\} \tag{5}$$

For $t_{8/5} \leq t_m$:

$$HV_{max} = 0.5 \times \left\{802C_{wt\%} + 305 + 406C_{wt\%} + 164CE_I + 183 - \left(369C_{wt\%} - 149CE_I + 100\right) \times \tan^{-1}\frac{\log t_m-2.822CE_{II}+0.262}{0.526-0.195CE_{II}}\right)\right\} \tag{6}$$

For $t_{8/5} \geq t_b$

$$HV_{max} = 0.5 \times \left[305C_{eq} + 101 + 406C_{wt\%} + 164CE_I + 183 - (369C_{wt\%} - 149CE_I + 100) \times \tan^{-1}\frac{\log t_{8/5}-2.822CE_{II}+0.262}{0.526-0.195CE_{II}}\right] \tag{7}$$

Where:

$$C_{eq} = C_{wt\%} + \frac{Si_{wt\%}}{11} + \frac{Mn_{wt\%}}{8} + \frac{Cu_{wt\%}}{9} + \frac{Ni_{wt\%}}{17} + \frac{Cr_{wt\%}}{5} + \frac{Mo_{wt\%}}{6} + \frac{V_{wt\%}}{3} \tag{8}$$

$$CE_I = C_{wt\%} + \frac{Si_{wt\%}}{24} + \frac{Mn_{wt\%}}{6} + \frac{Cu_{wt\%}}{15} + \frac{Ni_{wt\%}}{40} + \frac{Cr_{wt\%}}{6} + \frac{Mo_{wt\%}}{4} + \frac{V_{wt\%}}{5} +$$

$$\frac{Nb_{wt\%}}{5} + 10B_{wt\%} \tag{9}$$

$$CE_{II} = C_{wt\%} + \frac{Si_{wt\%}}{30} + \frac{Mn_{wt\%}}{5} + \frac{Cu_{wt\%}}{5} + \frac{Ni_{wt\%}}{20} + \frac{Cr_{wt\%}}{4} + \frac{Mo_{wt\%}}{6} + 10B_{wt\%} \tag{10}$$

2.2.3 Susceptibility to hot cracking

According to Jiang et al. (2016, p. 707), it is possible to assess sensitivity to hot cracking and susceptibility to reheat cracking of steels by their respective index. Hot cracking susceptibility index (HCS) and reheat cracking susceptibility index (P_{SR}) can be calculated from equation 11 and equation 12 respectively. Hot cracking is not expected when $Mn_{wt\%}$ to $S_{wt\%}$ ratio is more than 25 and HCS is less than 4.

$$\text{HCS} = \left[C_{wt\%} \times \frac{S_{wt\%} + P_{wt\%} + \frac{Si_{wt\%}}{25} + \frac{Ni_{wt\%}}{100}}{3M_{wt\%} + C_{wt\%} + Mo_{wt\%} + V_{wt\%}} \right] \times 10^3 \tag{11}$$

$$P_{SR} = Cr_{wt\%} + Cu_{wt\%} + 2Mo_{wt\%} + 5Ti_{wt\%} + 7Nb_{wt\%} + 10V_{wt\%} - 2 \tag{12}$$

In addition to P_{SR}, $\Delta G1$ (equation 13) and R_S (equation 14) are presented to indicate susceptibility of steels to reheat cracking. Steels with P_{SR} values lower than zero, $\Delta G1$ less than 2 or R_S less than 0.03 are less sensitive to reheat cracking. Although these equations are presented to evaluate the crack susceptibility of steels, these predictions must be considered with experimental data to evaluate steel weldabilities. (Nicholas & Abson 2008, pp. 18-19.)

$$\Delta G1 = 10C_{wt\%} + Cr_{wt\%} + 3.3Mo_{wt\%} + 8.1V_{wt\%} - 2 \tag{13}$$

$$R_S = 0.12Cu_{wt\%} + 0.19S_{wt\%} + 0.10As_{wt\%} + P_{wt\%} + 1.18Sn_{wt\%} + 1.49Sb_{wt\%} \tag{14}$$

2.3 Cold-formed hollow sections

Structural hollow sections are either cold-formed or hot-finished, based on their manufacturing method. For many applications, Cold-formed hollow sections are more economical than hot-finished ones; In addition, from an aesthetic point of view, they have the advantage of featuring smooth finished surfaces. Thus, they are more widely available

and employed in steel structures. When using them for any specific application, it is important to have no restrictions on applying hollow sections in compliance with standards dealing with steel structures. Some of the potential restrictions are the influence of corner radii, weldability, welding on the corner (cold-formed) areas and the possibility of brittle fracture, loss of ductility, softening etc. Some of typical profiles of cold-formed sections are presented in figure 6. (Puthli & Packer 2013, pp. 150-156; Yu 2000, pp. 3-5.)
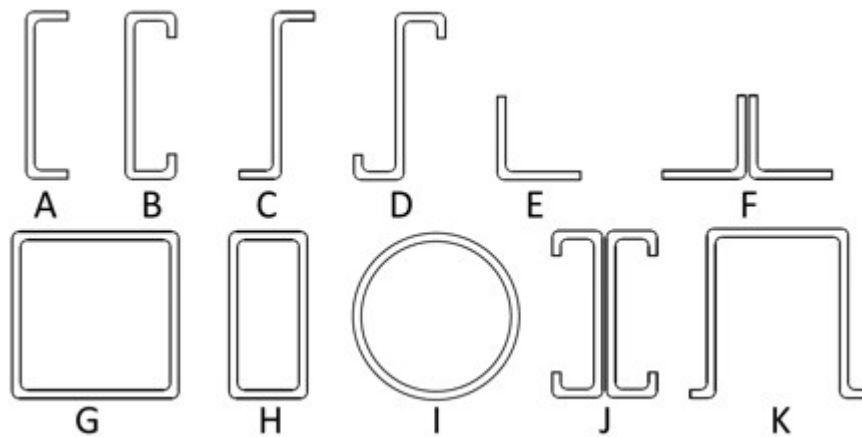

Figure 6. Cold-formed sections usually used in steel structures according to Yu (2000, p. 4).

2.3.1 Effects of cold-forming on materials properties

Cold-forming, also known as pre-strain or prior cold work in some studies, has some significant effects on physical and mechanical properties of steels. Although excessive strain and deformation results in rupture of metallic materials, controlled amounts of cold-forming drastically change mechanical properties of steels. From microstructural point of view, controlled pre-strain does not interrupt mechanical integrity and consistency of the material along its grains and their boundaries but induces different levels of plastic distortion on the microstructural features. Furthermore, cold-forming leads to the formation of dislocations. These distortions and dislocations hinder the mobility of grains while encouraging the mobility of atoms. All the aforementioned phenomena result in strain hardening, strain aging, and Bauschinger effect (as shown in figure 7). (Sloof & Schuster 2000, p. 518; Arreola-Herrera et al. 2014, pp. 445-450.)
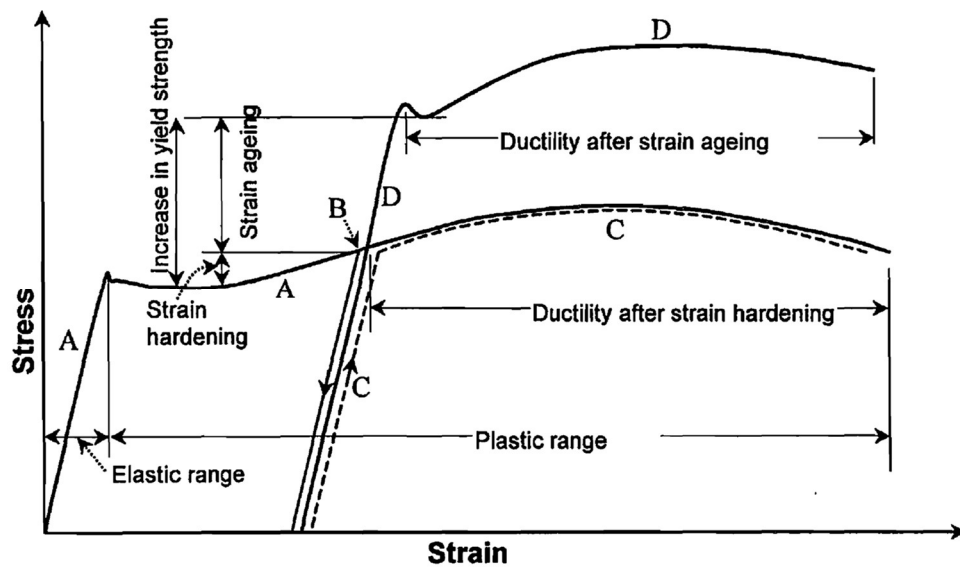
Figure 7. Effect of pre-strain on mechanical properties of mild steel (Sloof & Schuster 2000, p. 518).

Controlled pre-strain and cold-forming result in work hardening, increase in yield and tensile strengths, increase in hardness, decrease in ductility (as fracture elongation), and fracture toughness, but they may ease crack initiation and growth. In addition, they increase ductile to brittle fracture transition temperature (DBTT) and encourage material brittleness. Previous studies show that the extents of these consequences are not the same for various materials, and pre-strain has greater effects on materials with low ductility, low strain hardening capacity, or a high fraction of secondary particles (such as precipitation hardening steels). (Ochodek & Boxan 2014, pp. 88-92; Cosham, Hopkins & Palmer 2004, pp. 1-6.)

According to Ashraf, Gardner & Nethercot (2005, pp. 37-52), quality and degree of changes in mechanical properties after a bending process, as a type of cold-forming, depend upon the yield strength and tensile strength of the virgin material, its thickness, the bending inner radius, and the degree of bending (from 0° to 180°). To consider all these factors on an individual part of a steel structure, the general equation provided by Karren (equation 15) can be used to estimate the yield strength of the material after its bending process. In addition, expression presented by Eurocode 3, EN 1993-1-3: part 3.2, can be used to calculate approximate increase in the average yield strength of a steel structure due to its cold formed members (equation 18). (Macdonald et al. 1997, 513-521; Sloof & Schuster 2000, p. 520.)

$$\frac{F_{yc}}{F_y} = \frac{B}{\left(\frac{r}{t}\right)^m} \tag{15}$$

Where F_{yc} is the yield strength of the bended material, and F_y is the yield strength of its counterpart (virgin material). B and m can be calculated from equations 16 and 17:

$$B = 3.69 \times \frac{F_u}{F_y} - 0.819 \times \left(\frac{F_u}{F_y}\right)^2 - 1.79 \tag{16}$$

$$m = 0.192 \times \frac{F_u}{F_y} - 0.068 \tag{17}$$

$$F_{ya} = F_y + (F_u - F_y) \times \left(\frac{k \times n \times t^2}{A_g}\right) \quad \text{if} \quad F_{ya} \leq \frac{(F_u + F_y)}{2} \tag{18}$$

Where F_u is the tensile strength of the virgin material (MPa), F_{ya} is the average yield strength of a cross-section (MPa), A_g is the gross cross section (mm²), k is a numerical coefficient (k is 5 for bending), n is the number of normal bends with internal radius $r \leq 5t$, and t is the thickness of the steel members before cold-forming. There are also some experimental equations to correlate this increase in strengths to increase in hardness and decrease in ductility (Macdonald et al. 1997, 513-521).

2.4 Bending of (U)HSSs

Bending is the deformation of materials about one axis, which is usually used as a manufacturing process to form metallic materials into desired shapes. It can produce a variety of different shapes, including cold-formed hollow sections. This manufacturing process is associated with various parameters and limitations including bend allowance, bend deduction, K-factor and springback effect. (Diegel 2002.). Bending can be used to increase the fatigue durability of (U)HSSs and their steel structures. In addition, this process lowers the production costs. (Schuler 1998, pp. 366-373.)

It is usually desirable to use small radii for bending process to minimize its consequence springback effect, have a better sectional stiffness and have less limited design features. However, by decreasing the bending radius to material thickness ratio (r/t), likelihood of crack formations and shear fractures increase accordingly. In addition, due to the possibility

of local failures and shear fractures, general forming curves and bendability calculations are not very reliable for UHSSs and need more study. (Keeler, Kimchi & Mooney 2017, p. 90.) Excessively small bending radii may result in cracks and premature failures; thus, chosen r/t for the bending process should be large enough to be beyond the shear fracture limit of the material. Therefore, this criterion should be used to analyze the bendability of UHSSs, in addition to the common forming limits. For every type of steel, the minimum r/t ratio relies on its strength and elongation, and lower strength levels and higher elongations lead to smaller r/t ratios. (Keeler et al. 2017, p.30.) Suitability of the chosen inside bending radius depends on the type of the material, its thickness and bending direction. For example, the most appropriate direction for the bending process is transverse to the direction of its prior rolling. (Schuler 1998, 366-367.)

2.4.1 K-factor, bending allowance and springback

According to Diegel (2002), K-factor is the determining parameter regarding the location of the neutral axis for metal plates, and it is used to calculate their bending allowance, deduction, and springback. The only accurate method to find the actual K-factor value is to carry out some bending trials and reverse engineer the K-factor values from the measured bending allowance via equation 19, equation 20, and figure 8. (Diegel 2002; Mojarad 2017.)

$$BA = \frac{\pi \times (r + K \times t) \times A}{180} \tag{19}$$

$$K = \frac{t_0}{t} \tag{20}$$

Where BA is the bending allowance, r is the inside bend radius, K is known as K-factor, A is the bend angle, t is material thickness, and t_0 is the distance between inside surface of the bended material and its neutral axis. (Mojarad 2017.)

As a rule of thumb, approximate K-factors of metals for air bending, based on their hardness and strength, are presented in table 6 (Diegel, 2002). According to SSAB (2016a, p. 13), it is possible to bend (U)HSSs to some extends by standard bending machinery and bending methods. Bendability of some of these steels are presented in table 7. Three basic

characteristics of (U)HSSs which result in their good bendability (despite their high strengths) are having uniform properties, close thickness tolerances and high surface quality.
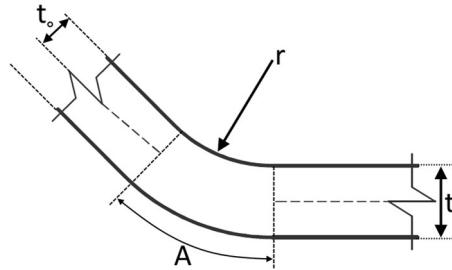

Figure 8. Schematic view of a bended sheet metal and its bending variables.

Table 6. General values of K-factor applicable in air bending (Diegel 2002, p.5).

r/t	Soft metals	Normal metals	Hard metals
$0 < r/t \leq 1$	0.33	0.38	0.40
$1 < r/t \leq 3$	0.40	0.43	0.45
$3 < r/t$	0.50	0.50	0.50

Table 7. Mechanical properties of the UHSSs manufactured by SSAB (SSAB 2016a, p. 9).

Hot rolled plates						
Name	Thickness (mm)	Yield strength (MPa)	Tensile strength (MPa)	Elongation (%)	Bendability (r/t)	Impact toughness at -40°C (J)
Strenx 700	4-53	700	780-930	14	1.5	69
Strenx 900	4-53	900	940-1100	12	2.5	27
Strenx 960	4-53	960	980-1150	12	2.5	40
Strenx 1100	5-40	1100	1250-1550	10	3.0	27
Strenx 1300	4-10	1300	1400-1700	8	4.0	27
Hot rolled strips						
Strenx 600MC	2-10	600	650-820	16	1.1	27
Strenx 650MC	2-10	650	700-880	14	1.2	27
Strenx 700MC	2-10	700	750-950	12	1.2	27
Strenx 900MC	3-10	900	930-1200	8	3.0	27
Strenx 960MC	3-10	960	1000-1250	7	3.5	27
Strenx 1100MC	3-8	1100	1250-1450	7	4.0	27

2.4.2 Welding of cold-formed structural steels

According to Androić, Dujmović & Pišković (2014, p. 930) and Puthli & Packer (2013, p. 151), exercise of welding on a bended or cold-formed section of a steel structure is acceptable if only it fulfills the conditions mentioned in table 8, based on the criteria provided by EN 1993-1-8. Adjacent areas mentioned in this table are within a length of 5×t from either side of the cold-formed corners. As an example, a hollow section which is not weldable in its cold-formed areas is presented in figure 9.

Table 8. Conditions and acceptance criteria for welding of cold-formed regions and their adjacent areas. Data from EN 1993-1-8 (2005, p. 49) and Puthli & Packer (2013, p. 152).

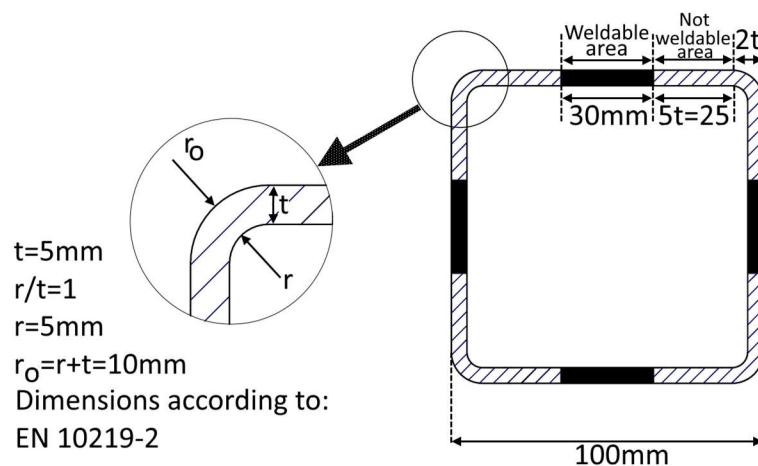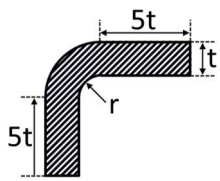| r/t | Strain due to cold forming | Maximum thickness (mm) | | Fully killed steel |
| | | Generally, | | |
		Predominantly static loading	Where fatigue predominates	
≥ 25	$\leq 2\%$	Any	Any	Any
≥ 10	$\leq 5\%$	Any	16	Any
≥ 3.0	$\leq 14\%$	24	12	24
≥ 2.0	$\leq 20\%$	12	10	12
≥ 1.5	$\leq 25\%$	8	8	10
≥ 1.0	$\leq 33\%$	4	4	6

Figure 9. Welding limitations (if the criteria of table 8 are not satisfied) for a cold-formed hollow section according to EN 1993-1-8.

2.5   Welding processes for joining UHSSs

UHSSs can be welded by laser beam, electron beam, electrical resistance and electric arc. However, characteristics and applicability of the resultant welded joints are very contingent upon the choice of the welding process and its parameters. These parameters include welding heat input, cooling rate and type of the filler material. The most typical welding processes used for joining (U)HSSs are shielded metal arc welding (SMAW), gas metal arc welding (GMAW), gas tungsten arc welding (GTAW) and laser welding (LW). (Kah, et al. 2014, p. 362; Tasalloti, Kah & Martikainen 2017, 29-30; Shome & Tumuluru 2015, 4-7.)

As mentioned before, the most typical problems associated with welding of (U)HSSs are HAZ softening, aging, and cold cracking. However, in comparison to medium and high carbon steels, (U)HSSs are more resistant to cold cracking due to their low carbon contents and small carbon equivalent values. In addition, it is possible to minimize the possibility of cold cracking and the degree of HAZ softening by choosing the proper process parameters. The parameters include preheat and interpass temperatures, which are governed by carbon equivalent values (CEV and CET, presented in equations 21 and 22). Higher CEV or CET necessitate using higher preheat and interpass temperatures. (SSAB 2015a, p. 4; SSAB 2016b, p. 22.)

$$\text{CEV} = C_{wt\%} + \frac{Mn_{wt\%}}{6} + \frac{Mo_{wt\%}+Cr_{wt\%}+V_{wt\%}}{5} + \frac{Ni_{wt\%}+Cu_{wt\%}}{15} \qquad (21)$$

$$\text{CET} = C_{wt\%} + \frac{Mn_{wt\%}+Mo_{wt\%}}{10} + \frac{(Cr_{wt\%}+C_{\ wt\%})}{20} + \frac{Ni_{wt\%}}{40} \qquad (22)$$

To prevent cold cracking in steels, hydrogen content or stress levels in the joint areas must be kept as low as possible. Thus, in addition to choosing proper interpass and preheat temperatures, it is necessary to use low hydrogen consumables, avert any impurity in the weld zone, arrange the right welding sequence, set the joint gap to a maximum of 3 mm, and avoid using welding consumables with strength levels higher than necessary. Minimum recommended preheat and interpass temperatures for different (U)HSSs are presented in figures 10 and 11 respectively. (SSAB 2015a, p. 5.)
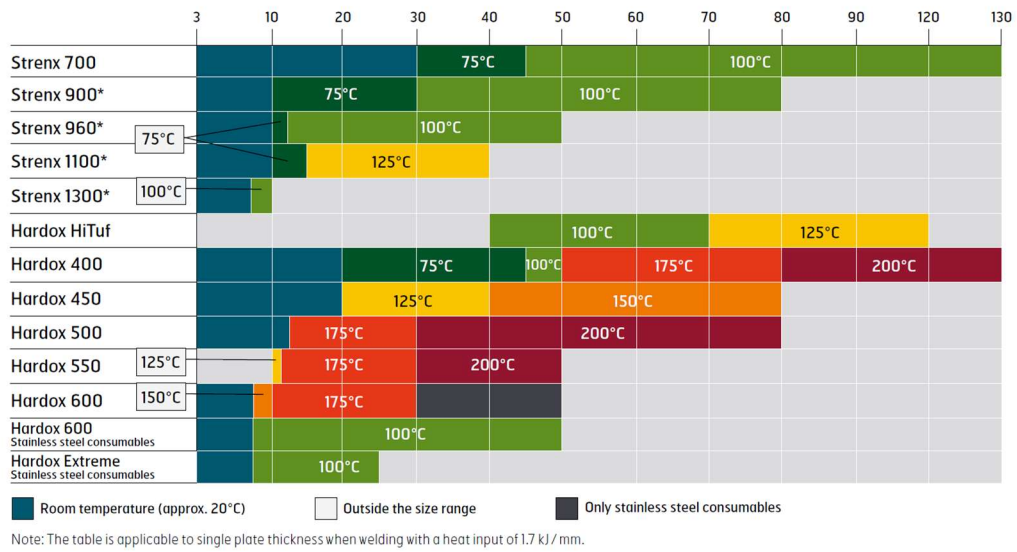
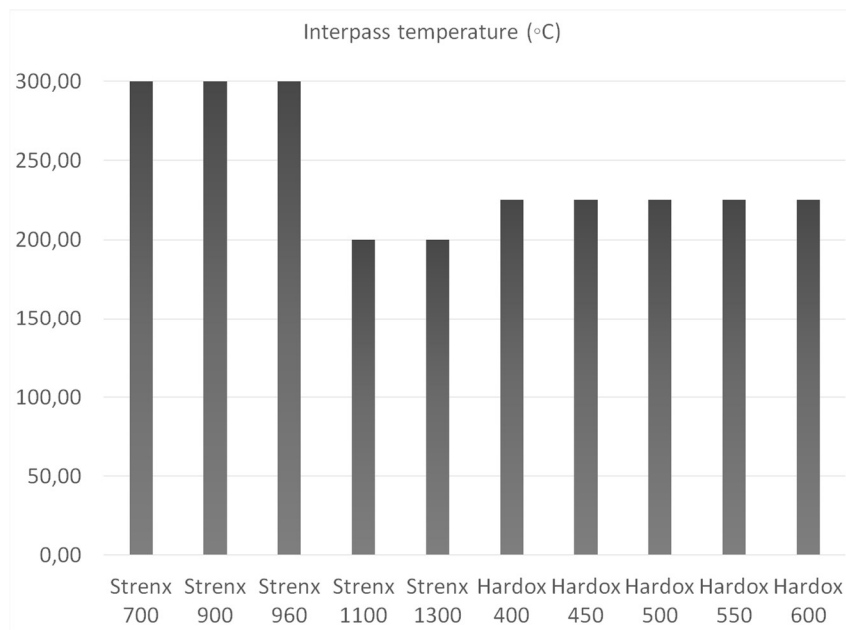**Figure 10.** Minimum recommended preheating temperatures for (U)HSSs (SSAB 2015a, p.5).

Figure 11. Maximum recommended interpass temperatures for some of (U)HSSs. Data from (SSAB 2015a, p.5).

2.5.1 Welding heat input, cooling time and other parameters.

To avoid a wide and brittle HAZ, it is important to control the amount of heat input during the welding process. Furthermore, the hardness values depend on the carbon content of the material and cooling rate of the welding process. The cooling rate is expressed as $t_{8/5}$ for any specific welding procedure (Hubmer et al. 2017, pp. 1-11). According to EN-1011-2 (2001, pp. 41-42), this parameter can be derived from equation 23 (for two-dimensional heat flow) and equation 24 (for three-dimensional heat flow) as follows:

$$t_{8/5} = (4300 - 4.3T_0) \times 10^5 \times (\tfrac{Q}{t})^2 \times \left(\frac{1}{(500-T_0)^2} - \frac{1}{(800-T_0)^2}\right) \times F_2 \tag{23}$$

$$t_{8/5} = (6700 - 5T_0) \times Q \times \left(\frac{1}{500_0} - \frac{1}{800-T_0}\right) \times F_3 \tag{24}$$

Where T_0 is preheating temperature in °C, t is the thickness in mm, Q is welding heat input in KJ/mm (calculated from equation 25), F_2 and F_3 are dimensionless shape factors which must be determined according to table 9.

$$Q = \frac{\varepsilon \times U \times I}{v \times 100} \tag{25}$$

Where ε is thermal efficiency of the welding procedure according to table 10, I is the welding current in amperes, U is welding electrical potential in volts, v is welding speed in mm/sec. critical thickness which marks the transition between two-dimensional and three-dimensional heat flows can be derived from figure 12. (EN 1011-2 2001, p. 41.) Recommended heat inputs, consumables and shielding gases are presented in figure 13, figure 14, and table 11 respectively. To avoid cold and hydrogen cracking, the joint gap should not exceed 3 mm. Furthermore, to achieve a good impact toughness and minimize distortion, it is recommended to keep the welding heat input as low as possible and use multi-pass welding for thicknesses higher than 6 mm (figure 15). (SSAB 2015a, pp. 1-16; SSAB 2015b, pp. 1-20.)
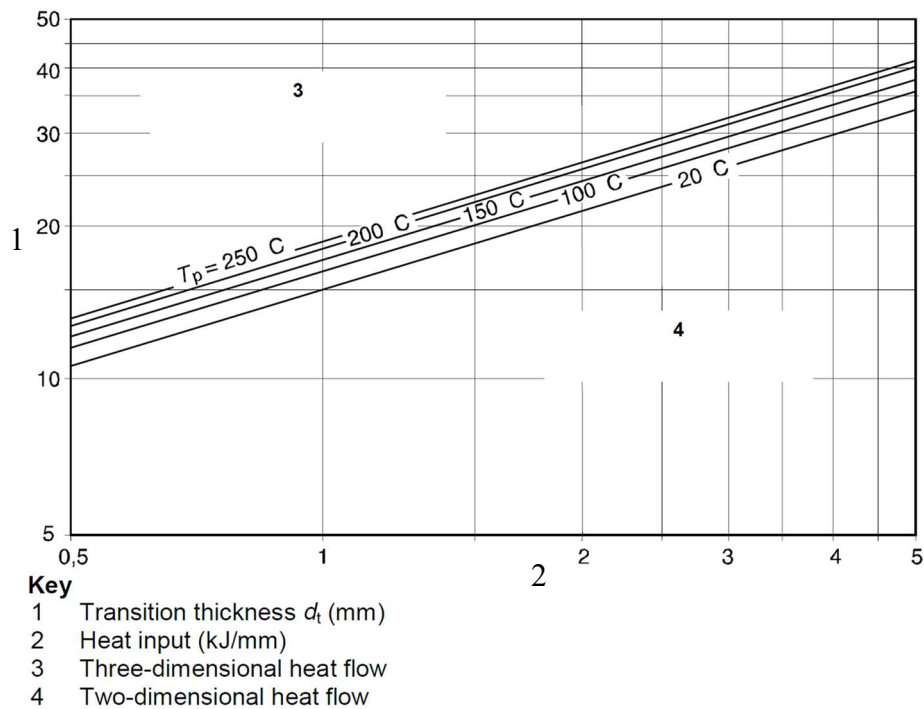
Key
1   Transition thickness d_t (mm)
2   Heat input (kJ/mm)
3   Three-dimensional heat flow
4   Two-dimensional heat flow

Figure 12. The critical thickness between two-dimensional and three-dimensional heat flow as a function of heat input for different preheat temperatures (EN 1011-2 2001, p. 45; reprint with permission[1]).

Table 9. Shape factors according to joint design according to EN 1011-2 (2001, p.42).

Type of weld		Shape Factor	
Name	Schematic view	*F2*	*F3*
Bead on plate		1.00	1.00
Between runs, butt weld		0.90	0.90
Single run, Fillet weld on a corner		0.67 – 0.90	0.67
Single run, fillet weld in a T-joint		0.45 – 0.67	0.67

Table 10. Thermal efficiency factor for different welding processes (EN 1011-1, p.12).

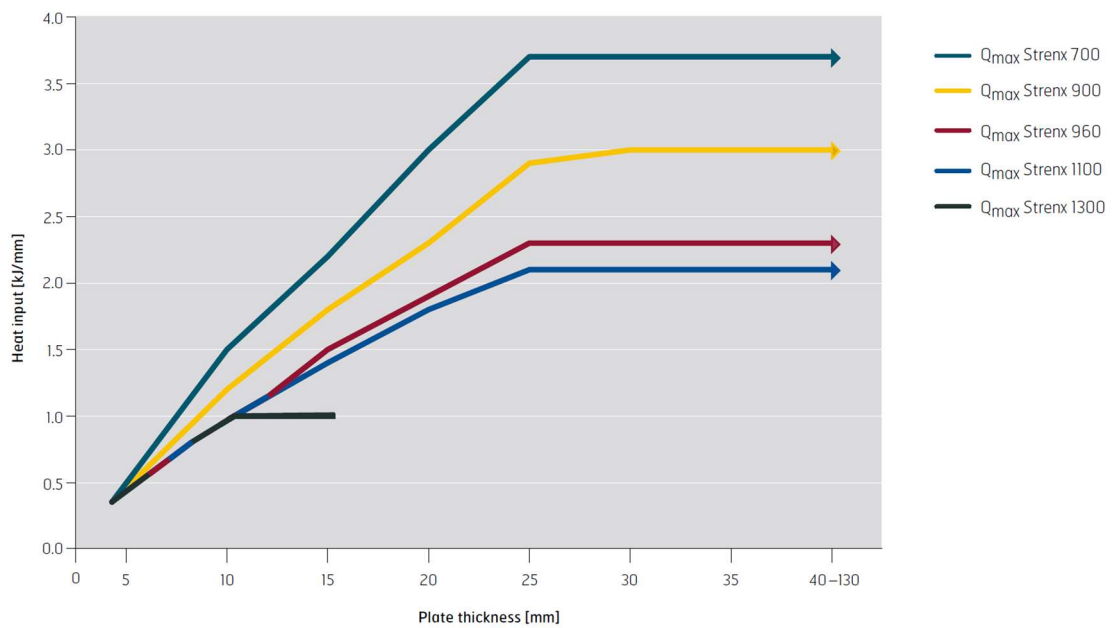| Welding Process	ε
Submerged arc welding	1.0
Manual metal-arc welding	0.8
Metal-inert gas welding	0.8
Metal-active gas welding	0.8
Self-shielded tubular-cored arc welding	0.8
Self-shielded tubular-cored arc welding with active gas	0.8
Self-shielded tubular-cored arc welding with inert gas	0.8
Tungsten-inert gas welding	0.6
Plasma arc welding	0.6

Figure 13. Recommended heat input for different (U)HSSs according to their thicknesses (SSAB, 2015a, p. 8).

32

Table 11. Instances of different shielding gases suitable for welding (U)HSSs (SSAB, 2015a, p.13).

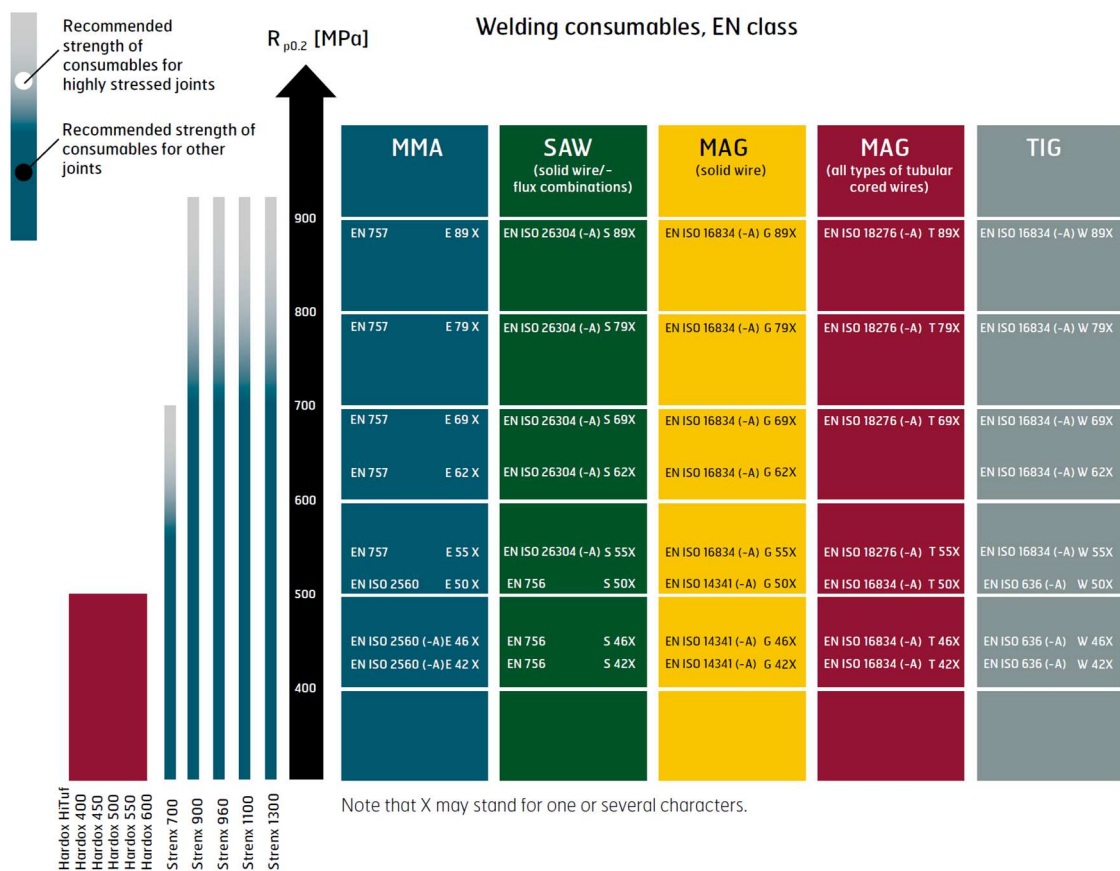| Welding method	Arc type	Shielding gas (Volume %)
Metal active gas (MAG), solid wire MAG, metal cored wire	Short arc	$Ar + 12\%\text{-}25\ \% \ CO_2$
MAG, solid wire MAG, metal cored wire	Spray arc	$Ar + 8\%\text{-}25\ \% \ CO_2$
MAG, flux cored wire	Short arc	$Ar + 15\%\text{-}25\ \% \ CO_2$; Pure CO_2
MAG, flux cored wire	Spray arc	$Ar + 8\%\text{-}25\ \% \ CO_2$
MAG, all types	All arc types	$Ar + 15\%\text{-}25\% \ CO_2$
Tungsten inert gas (TIG)	-	Pure Ar

Figure 14. Welding consumable for (U)HSSs according to American welding society (AWS) (SSAB, 2015a, p.11).
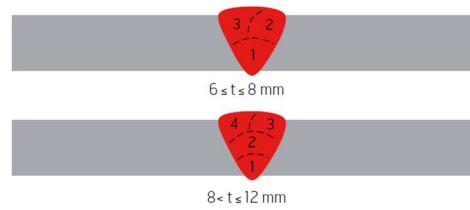
Figure 15. Recommended number of passes for welding thick sections of (U)HSSs using a single V joint preparation to fulfill the required impact toughness of welded joints (SSAB 2015b, p.14).

In conclusion, applying low heat inputs ensures better toughness values for the weld metal and HAZ; in addition, it increases joint strength. Although a post-weld heat treatment can be carried out in the joint area to prevent some welding defects, it is not usually required. Finally, to achieve the essential fracture toughness values for welded joints, their cooling rates should be in a specific range. (SSAB 2016b, pp. 4-15.) Recommended cooling rates to achieve fracture toughness of 27 J at -40 ºC are presented in table 12.

Table 12. Recommended values of $t_{8/5}$ for some (U)HSSs (SSAB 2017, p. 13).

Steel Grade	$t_{8/5}$ as the cooling time (s)
700	5-25
900	5-20
960-1300	5-15
700MC, 650MC, 600MC, 700MH	1-20
900MC, 960MC, 960MH	1-15
1100MC	1-10

2.6   Welded UHSSs

High and ultra-high strength steels are appealing to steel manufacturers due to their technical and economical values. In addition, welding, as an efficient manufacturing method, is a frequently used process for industrial purposes. (Kah et al. 2014, p. 357) Thus, welding of (U)HSSs have recently been the subject of many studies. Among various welding processes, laser welding, as a non-contact and clean welding process with a low heat input, and Gas-metal arc welding, as a versatile and economical welding process, which is suitable for mass manufacturing, are the two most attractive welding processes for joining (U)HSSs in industry. (Guo et al. 2017, pp. 1-2; Guo et al. 2015, p.197.)

Numerous studies have been carried out on the effects of these processes on microstructures and mechanical properties of (U)HSSs. As an example, Guo et al. (2017, pp. 1-15) recently compared properties of S960 welded by ultra-narrow gap laser welding and gas-metal arc welding. According to their results, the FZ of ultra-NGLW joint was martensitic while the FZ of the GMAW joint had a ferritic microstructure accompanied with some amount of martensite. Furthermore, joint welded by GMAW had a lower tensile strength and a softened heat affected zone. However, it showed higher impact toughness than ultra-NGLW ones. Welding parameters and joint preparation used in this study are presented in table 13 and figure 16. All samples welded by GMAW failed from HAZ softened areas.

Table 13. Optimized GMAW parameters for welding an 8 mm thick steel S960 via multi-pass technique (Guo et al. 2017, p. 3).

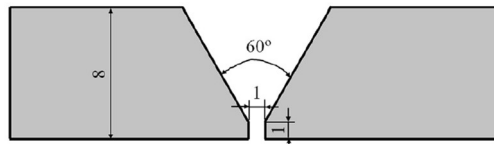| Pass No.	Voltage (V)	Current (A)	Welding speed (m/min)	Wire feeding rate (m/min)	Shielding gas flow rate (l/min)	Heat input (Kj/mm)
1	27	175	0.40	4.0	22	0.57
2	27	165	0.46	4.0	22	0.46
3	27	168	0.26	4.0	22	0.84

Figure 16. Schematic of the joint design for Gas-metal arc welding of an 8mm thick S960 plate used by Guo et al. (2017, p. 3, reprint with permission).

Siltanen, Tihinen & Kömi (2015, pp. 1-9) investigated weldability of 6 mm thick samples made from direct quenched S960 and welded by laser-GMAW hybrid welding. According to their results, it was possible to achieve good mechanical properties in the FZ by this welding method. In addition, although an undermatching filler material was used for the welding procedure, the resultant joint was as strong as the base material. They attributed these satisfying results to low carbon content and carbon equivalent of S960 QC.

Garašić et al. (2010, pp. 327-335) studied the probability of cold cracking in S960 welded joints. At the end of their study, they attributed the occurrence of such cracks to the level of air humidity and the range of service temperature. In addition, they concluded higher cooling rates and increased hydrogen contents of the weld metal encouraged cold cracking in welded

metals. Accordingly, by applying proper welding parameters, it was possible to avoid cold cracking in final welds.

In another study, Němeček, Mužík & Míšek (2012, pp. 67-74) studied Laser welded, MAG welded and TIG welded UHSS joints made of steel with yield strength of 900 MPa and 1200 MPa, respectively. Through their investigation, they found that the martensitic microstructure of the base metals changed into a bainitic microstructure after MAG welding. Furthermore, the most obvious difference between the joints welded by different welding processes was their tensile properties. Samples welded by laser welding had the highest strengths.

Lee et al. (2014, pp. 559-565) investigated the joint properties of dual phase UHSS DP780 welded by Laser, TIG, and MAG welding methods. They concluded that the size of the FZ increased with increasing the heat input, while the hardness increased with increasing the cooling rate. In addition, the strength of the joint produced by metal active gas welding method had a noticeable decrease due to its wide softened weld metal and heat affected zone. Finally, value of the elongation to failure decreased after welding, regardless of the welding method. This decrease was attributed to the strain localization in the welded samples.

According to Javidan et al. (2016, pp. 16-27), HAZ microstructure of (U)HSSs depended on the type of steel, kind of welding technique, amount of welding heat input, and the material condition after the welding process. Furthermore, according to Gerhards, Reisgen & Olschok (2016, pp. 352-361), neither welding speed nor post weld heat treatment could prevent or improve softened HAZ of (U)HSSs. According to their research, controlling the heat dissipation into the outer areas from the joint was the only effective factor regarding this matter.

Yun et al. (2014, pp. 539-544) studied the correlations of mechanical properties and post weld microstructure for (U)HSSs. According to their study, microstructure of the FZ can be categorized into three basic groups. The first group is acicular ferrite with small amounts of bainite. The second one is a mixture of acicular ferrite and martensite, and the last one is a mixture of bainite and martensite. In comparison to acicular ferrite, weld metal with more

martensite to bainite ratio and more homogenous martensite distribution among bainite blocks had a better combination of strength and toughness.

In a recent study, Kurc-Lisiecka, Piwnik & Lisiecki, (2017, 1651-1657) investigated the weldability of UHSS STRENX 1100MC. According to their research, HAZ softening was the most obvious drawback of the welded STRENX 1100MC. The other negative effect of welding on this material was its drastic decrease (up to 60%) in fracture toughness. In another study, Kurc-Lisiecka (2017, pp. 643-649) attributed this decrease in the fracture toughness to the existence of plate martensite after the welding process.

3   EXPERIMENTAL PROCEDURE

In this study, experimental approach was used to evaluate weldability of (U)HSSs S700MC and S1100. Chemical compositions and mechanical properties of these steels according to their manufacturer are presented in tables 2 through 5 in section 2.1. Through this study, uniaxial tensile tests, microhardness measurements, Charpy impact toughness examinations, and microstructural analysis have been carried out on the welded samples to evaluate their joint quality and weldability of their base metals.

3.1   Bending trials

Two sets of specimens made from different steels, S700MC and S1100, were bended via air bending with various bending radii to emulate different degrees of cold-forming. Schematic cross-sectional views of the bended base metals are presented in figure 17. FEM analysis using ABAQUS was used to simulate bending trials to estimate their degree of cold-forming (plastic pre-strains). A summary of the bended specimens and their bending parameters are presented in tables 14 and 15 respectively. The results of the simulations are also presented in table 14. As an example, figure 18 shows the visualized result of a simulation for a bended sample.

Table 14. General specifications of the bended samples.

Bending Radius (mm)	Material	r/t	Dimensions of the Plate prior the bending (mm)	Degree of bending[*] (Degrees)	Approximate Maximum tensile strain induced by the cold-forming according to FEM (%)
5	S700MC	0.50	200×100×10	90	64
10	S700MC	1.00	200×100×10	90	43
15	S700MC	1.50	200×100×10	90	34
20	S700MC	2.00	200×100×10	90	28
24	S1100	3.00	200×300×8	90	20
26	S1100	3.25	200×300×8	90	11
28	S1100	3.50	200×300×8	90	10
30	S1100	3.75	200×300×8	90	9
37	S1100	4.60	200×300×8	90	7
40	S1100	5.00	200×300×8	90	7
* Bending axis is perpendicular to the rolling direction					

Table 15. Bending parameters

Material	Maximum bending force (KN)	Punch speed (mm/s)	Die opening (mm)	Bending machine
S700MC	1000	9.5	100	Press brake Ursviken Optima 100
S1100	1000	9.5	140	Press brake Ursviken Optima 100
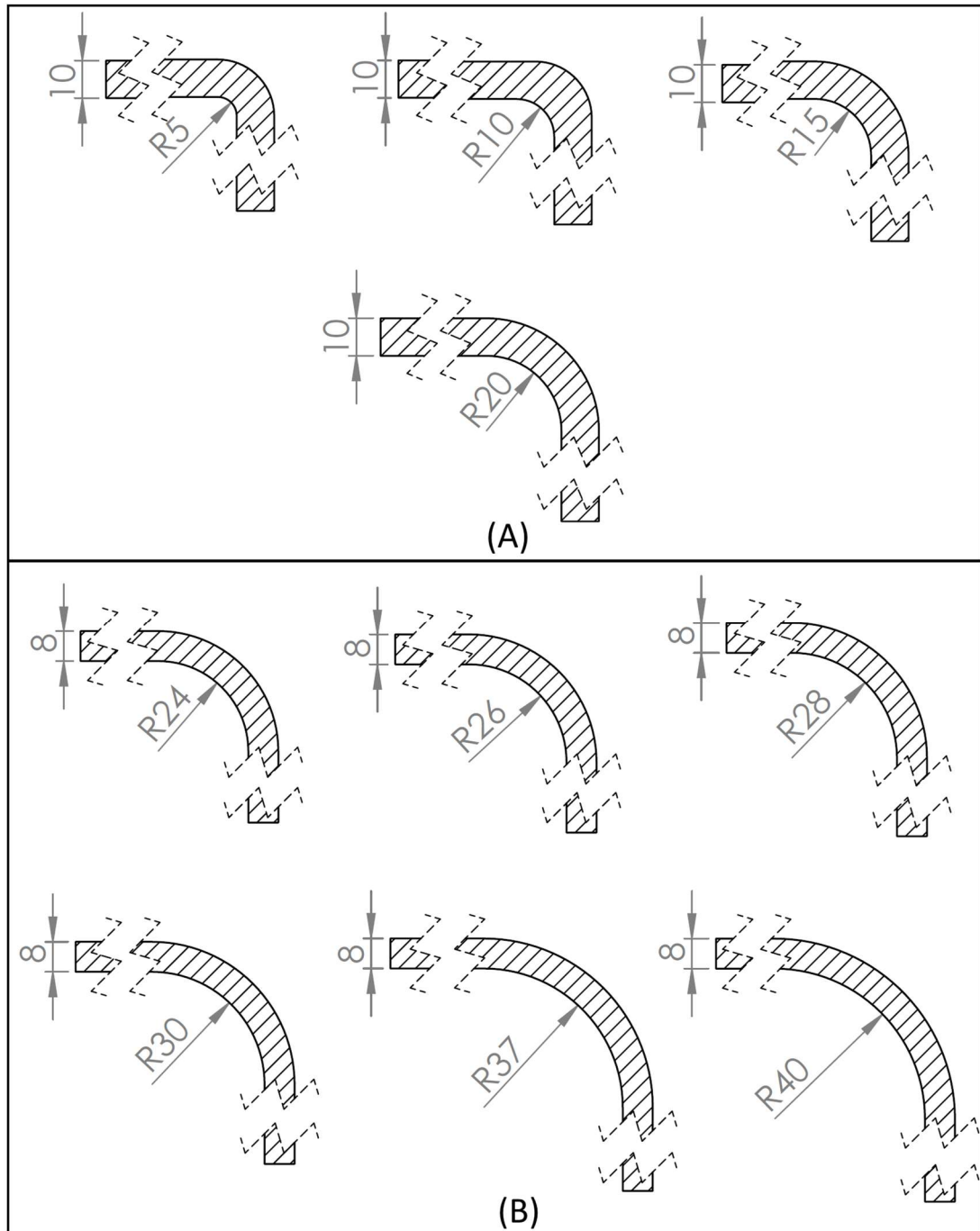
Figure 17. Schematic views of the bended base metals according to their materials and radii: (A) plates made of S700MC; (B) plates made of S1100.
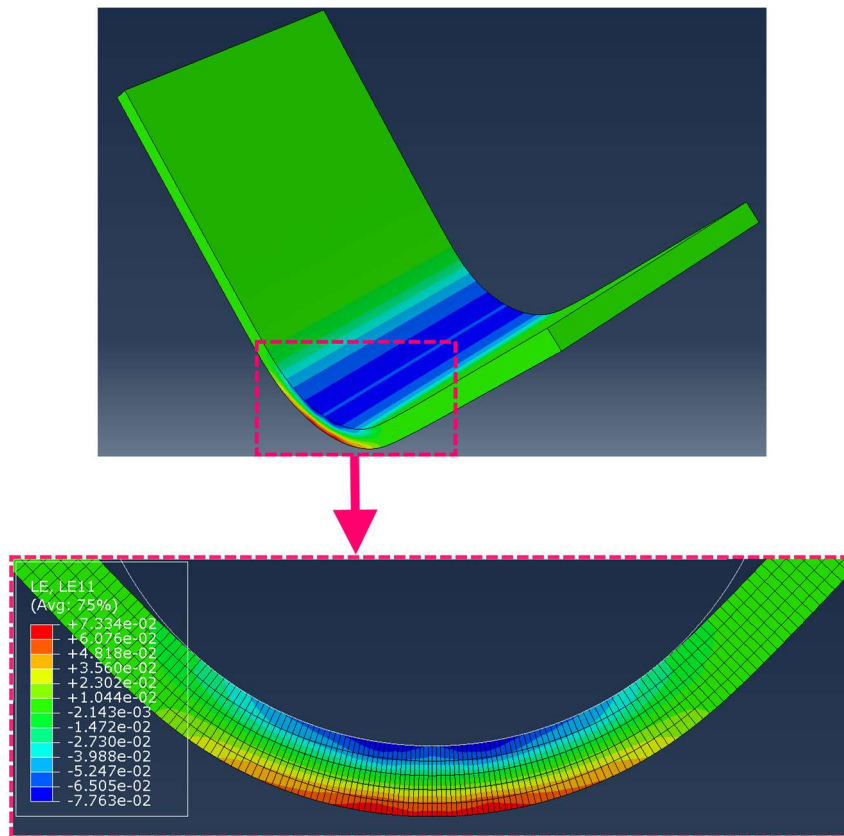
Figure 18. Simulation of an 8 mm thick plate, made of UHSS S1100 (bending radius and angle are 40 mm and 90º respectively).

3.2   Welding trials

As mentioned in section 2.2, it is possible to evaluate the weldability of a low-alloy steel by calculating its values of CEN, P_{cm}, HCS, P_{SR}, $\Delta G1$, and R_S. These values are presented for S700MC and S1100 in table 16. According to this table, excessive hardening, cold cracking, and reheat cracking are some possible difficulties for welding these steels, in addition to HAZ softening and aging. Thus, it is of utmost importance to choose the proper values of heat inputs and filler materials to avoid these defects.

Table 16. Theoretical weldability parameters of the base metals.

Material	CEN	P_{cm}	$\dfrac{\%Mn}{\%S}$	HCS	P_{SR}	$\Delta G1$	R_S
S700MC	0.33	0.34	210	0.70	1.38	0.82	0.02
S1100	0.58	0.47	280	2.76	0.50	3.21	0.06
Green: parametric value is suitable for welding							
Orange: parametric value is not suitable for welding							

Metal active gas (MAG) welding, as an often used joining process with a good control over its welding parameters, was chosen to perform the welding procedures in this study. To avoid cold cracking and benefit from some proper arc properties, a mixture of Argon and carbon dioxide was chosen as the shielding gas (according to table 11). Welding parameters were chosen based on the criteria discussed in the earlier sections; next, welding heat input was calculated and checked by equation 25 and software WeldCalc 2.2[2] respectively. Calculated welding parameters used in practice are summarized in table 17.

Cooling rate, $t_{8/5}$, was also calculated according to the criteria discussed in section 2.5.1 of this study; next, the calculated values were checked by $HV10_{max}$ criterion and recommended values of table 12. These data are summarized in table 18. According to their bending criteria and base metals, 10 sets of welded specimens were prepared and investigated for this study. Table 19 presents a list of the welded samples and their actual welding parameters. In addition, schematic views of the joint designs and a welded joint are presented in figure 19.

Table 17. Calculated welding parameters.

Base material	Material thickness (mm)	Welding heat input (KJ/mm)	Welding voltage (V)	Welding current (A)	Welding speed (mm/s)	Type of the filler material	Filler feeding rate (m/min)	Type of the shielding gas	Shielding gas flow rate (l/min)
S700MC	10	0.65	25	220	7	Böhler alform® 700-MC*	10	92Ar-8CO$_2$	10-15
S1100	8	0.65	25	220	7	Böhler union X96**	10	92Ar-8CO$_2$	10-15
Preheat temperature for all welding procedures: 25 ºC Maximum interpass temperature for all welding procedures: 50 ºC									
* Matching filler material was used to minimize the possibility of cold cracking									
** At the time of this study, no matching filler material was available for S1100; therefore, the closest filler material to its mechanical properties was chosen for its welding procedure.									

Table 18. Calculated values of carbon equivalent and HV_{max}.

Material	C_{ev}	CE_I	CE_{II}	HV_{max}
S700MC	0.468	0.536	0.547	351
S1100	0.917	0.918	1.083	446*
* Due to the carbon equivalent values of S1100, this is the minimum possible theoretical value for its HV_{max}, regardless of the cooling rate.				

---

[2] Weldcalc 2.2 is a web-based freeware developed by SSAB to calculate optimized parameters of arc welding for UHSSs or to check the calculated values to see if they fit in the weldability parametric window or "tolerance box".

Table 19. Welded samples according to their bending condition and base materials.

General welding parameters										
Base material	r/t	Pass No.1		Pass No.2		Pass No.3		Pass No.4		Travel speed (mm/s)	Approximate accumulated heat input (KJ/mm)
		I (amp)	V (volt)	I (amp)	V (volt)	I (amp)	V (volt)	I (amp)	V (volt)		
S700MC	0.50	211	25.3	205	27.0	206	26.6	-	-	7.5	1.75
S700MC	1.00	210	25.3	206	27.0	207	26.7	-	-	7.5	1.75
S700MC	1.50	209	25.3	203	26.8	204	26.8	204	27.0	7.5	2.30
S700MC	2.00	205	25.4	203	27.0	206	26.6	204	27.0	7.5	2.30
S1100	3.00	220	26.0	215	27.5	216	27.8	213	27.4	7.5	2.50
S1100	3.25	219	26.0	215	27.5	216	27.8	213	27.4	7.5	2.50
S1100	3.50	219	26.0	212	27.6	216	27.5	217	27.3	7.5	2.50
S1100	3.75	219	26.0	212	27.4	216	27.4	212	27.4	7.5	2.50
S1100	4.60	219	26.0	216	27.4	215	27.2	210	27.5	7.5	2.50
S1100	5.00	216	26.3	212	27.5	217	27.3	212	27.5	7.5	2.50
Calculated welding heat inputs and cooling times										
Base material	r/t	Pass No.1		Pass No.2		Pass No.3		Pass No.4			
		Heat input (Kj/mm)	$t_{8/5}$ (s)	Heat input (Kj/mm)	$t_{8/5}$ (s)	Heat input (Kj/mm)	$t_{8/5}$ (s)	Heat input (Kj/mm)	$t_{8/5}$ (s)		
S700MC	0.50	0.605	4.25	0.627	4.56	0.621	4.48	-	-		
S700MC	1.00	0.602	4.21	0.630	4.61	0.626	4.55	-	-		
S700MC	1.50	0.599	4.17	0.616	4.40	0.619	4.45	0.624	4.52		
S700MC	2.00	0.590	4.05	0.621	4.48	0.621	4.48	0.624	4.52		
S1100	3.00	0.648	7.62	0.675	8.27	0.681	8.42	0.661	7.93		
S1100	3.25	0.645	7.55	0.675	8.27	0.681	8.42	0.661	7.93		
S1100	3.50	0.645	7.55	0.663	7.98	0.673	8.22	0.671	8.17		
S1100	3.75	0.645	7.55	0.658	7.86	0.670	8.15	0.658	7.86		
S1100	4.60	0.645	7.55	0.670	8.15	0.662	7.95	0.655	7.79		
S1100	5.00	0.644	7.52	0.660	7.90	0.671	8.17	0.661	7.93		

3.3 Microstructural analysis

Welded samples were cut into the proper size, grinded with different grades of emery, and polished by diamond paste (1 μm) to reach the required level of surface finish to perform the microstructural analysis. After polishing, samples were etched by Nital[3] solution for 5 seconds to reveal their microstructural features for further investigation. Thereafter, microstructural evaluations were carried out via optical and scanning electron microscopy (SEM). Macrostructural features of the samples were investigated via optical microscopy at the laboratory of welding technology at Lappeenranta University of Technology (LUT), while their microstructural features were studied by scanning electron microscopy at the SEM laboratory located in the department of chemical engineering at LUT.
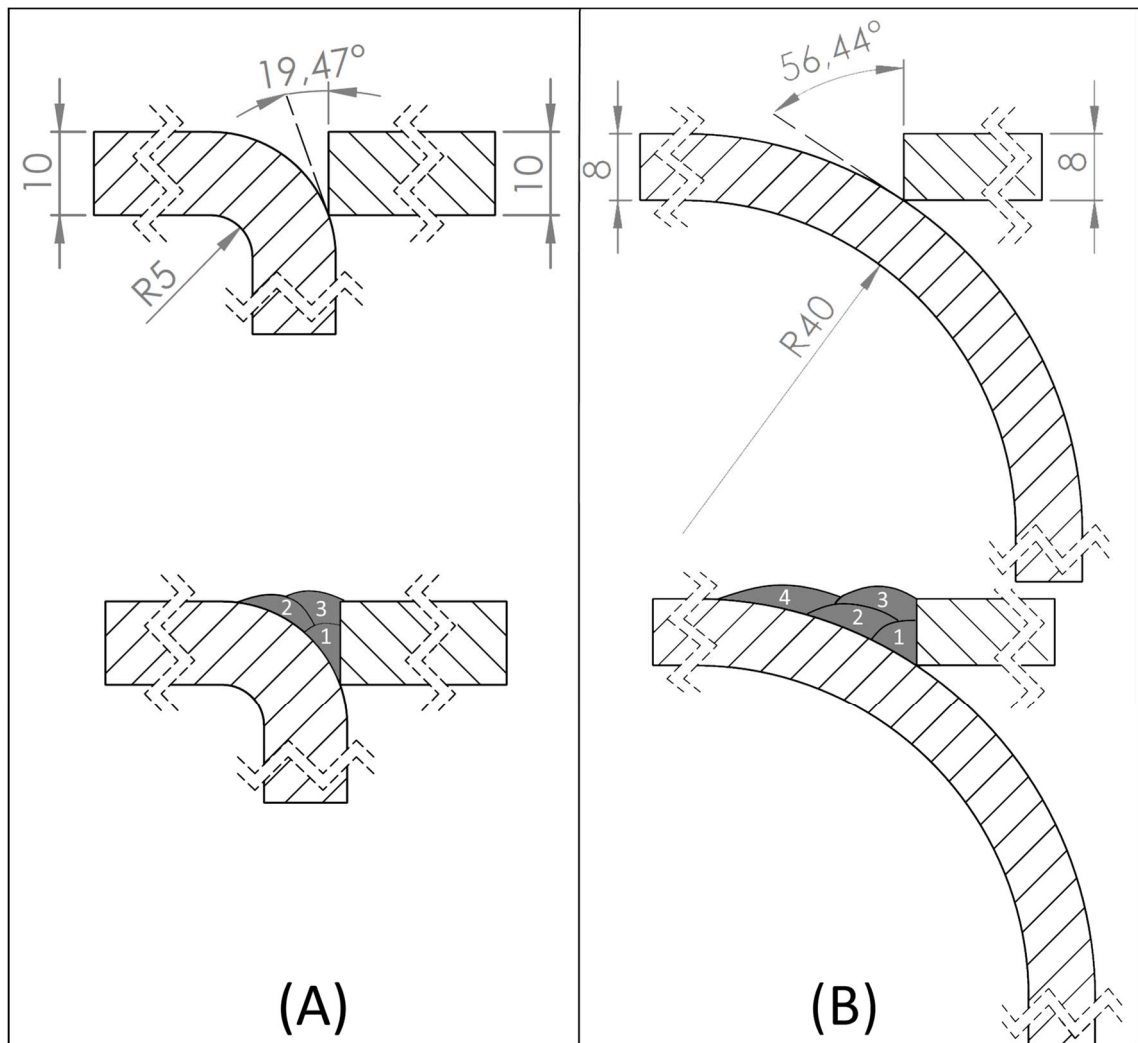
---

[3] 95ml C_2H_5OH + 5ml HNO_3

Figure 19. Schematic views of joint design for (A) sample with 5 mm bending radius (as the minimum bending radius); and, (B) sample with 40 mm bending radius (as the maximum bending radius); all root gaps and root faces are considered as zero.

3.4 Microhardness measurements

Microhardness measurements were carried out according to ISO 6507-1 at the laboratory of welding technology at LUT. Based on their location, microhardness indentations were 0.5 mm to 1.5 mm apart from each other, and measurements were carried out along three separate lines. The first line was located on the upper side of the joint to measure the hardness changes near the surface of the joint and its final welding passes. The second line was on the middle section of the joint to measure the hardness fluctuations along the reheated welding passes. The final line was located on the lower section of the joint to evaluate the hardness variations along the root pass (Figure 20).
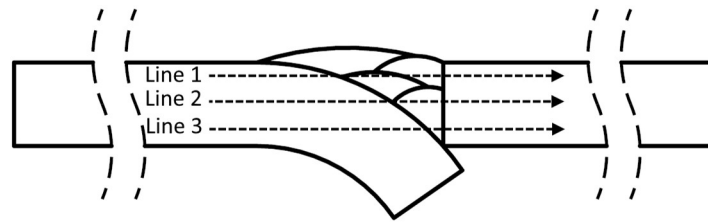
Figure 20. Schematic view of the hardness measurements along the transverse sections of the welded samples.

3.5 Uniaxial tensile tests

Flat test specimens were cut out and prepared from the welded samples in accordance with ASTM E8M. Dimensions of the tensile specimens are presented in figure 21. Tensile tests were carried out with strain rate of 0.004 s^{-1}. During the tests, a digital image correlation (DIC) system recorded the local displacements on the specimen surfaces to measure their elongation values. As an example, a similar DIC system used in another study is presented in figure 22. DIC system used in this study was an ARAMIS non-contact measuring system manufactured and developed by GOM. Data gathered from ARAMIS system were evaluated via GOM^{TM} Correlate 2017 software package, also developed by GOM.
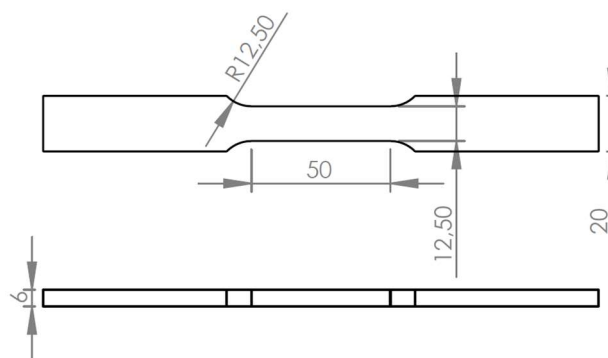
Figure 21. Schematic view of the flat specimen used for uniaxial tensile test.
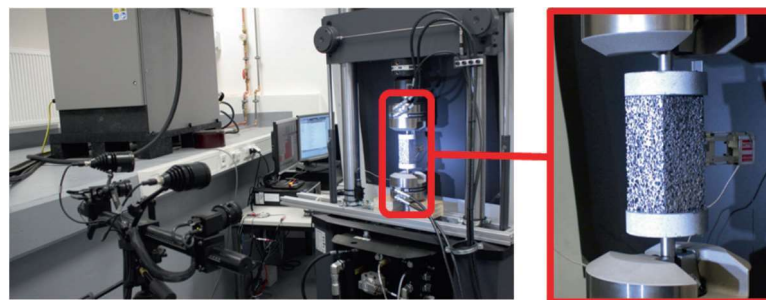
Figure 22. A DIC system used along with a fatigue test set-up (Nesic, Krupp & Michels 2014, p. 272; reprint with permission)

3.6 Notch toughness tests

Sub-size Charpy impact test specimens were prepared according to ASTM E23M, and their notch toughness values were measured at -40 ºC. A schematic view of the specimens is presented in figure 23. Due to the limited thickness range of the welded samples, thickness value of Charpy specimens was also limited to 5 mm; thus, the correction factor calculated by equation 22 was required to extrapolate actual notch toughness values. (Lucon, McCowan & Santoyo 2016, p. 12)

$$e' = \left[K' \times (1 - \frac{d'}{D'})\right] + E' \times \frac{s'}{S'} \tag{26}$$

Where e' and E' are fracture energy densities (J/mm^3) for sub-size and normal specimens respectively. K' is energy of rupture which is considered as 29.3 J for ductile steels. d' and D' are ligament sizes of sub-size and normal specimens respectively (mm). Finally, s' and S' are cross sectional areas of sub-size and normal specimens respectively (mm^2). According to Lucon et al. (2016, p.12), if the sub-size and normal specimens have equal ligament sizes, similar to the specimens used in this study, their fracture energy densities are proportional to their cross-sectional areas. Thus, equation 26 can be changed to equation 27:

$$e' = E' \times \frac{s'}{S'} \tag{27}$$

After breaking the samples, their fracture surfaces were analyzed via micro-photography using a Canon Powershot SX110IS camera and ImageJ^{TM} software package to determine the proportion of shear fracture surface area (SFA) for each broken sample.
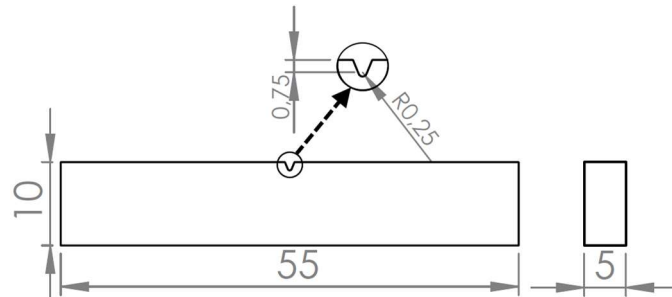
Figure 23. Schematic view of the sub-size notch toughness test specimen and its dimensions according to ASTM E23.

4   RESULTS AND DISCUSSION

Figures 24 and 25 present the overall macrostructural features of the welded samples. According to these figures, except few porosities in some samples, no other weld discontinuity was visible in the welded joints. In addition, no sign of any types of cracks was present in the welded materials and their adjacent heat affected zones. Majority of the porosities occurred between the second and the third passes of the welded joints. Since these passes are located on the curvature of the bended side, they might be a sign of improper torch angle during the welding of the second and the third passes. However, since the occurrence of these discontinuities was quite random, they also might be due to the excess use of the anti-spatter compound between these passes for some welds. (Evans, 2010)
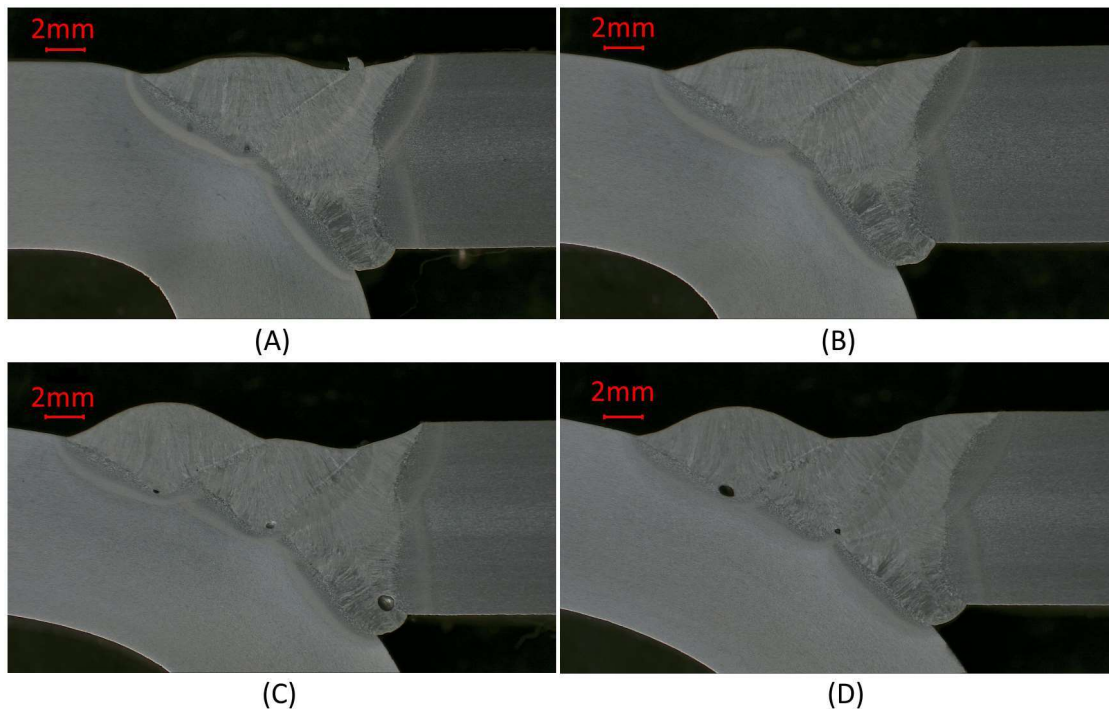
Figure 24. Macroscopic pictures of the welded samples made from S700MC with different bending radii: (A) r = 5 mm, r/t = 0.5; (B) r = 10 mm, r/t = 1; (C) r = 15 mm, r/t = 1.5; (D) r = 20 mm, r/t = 2.
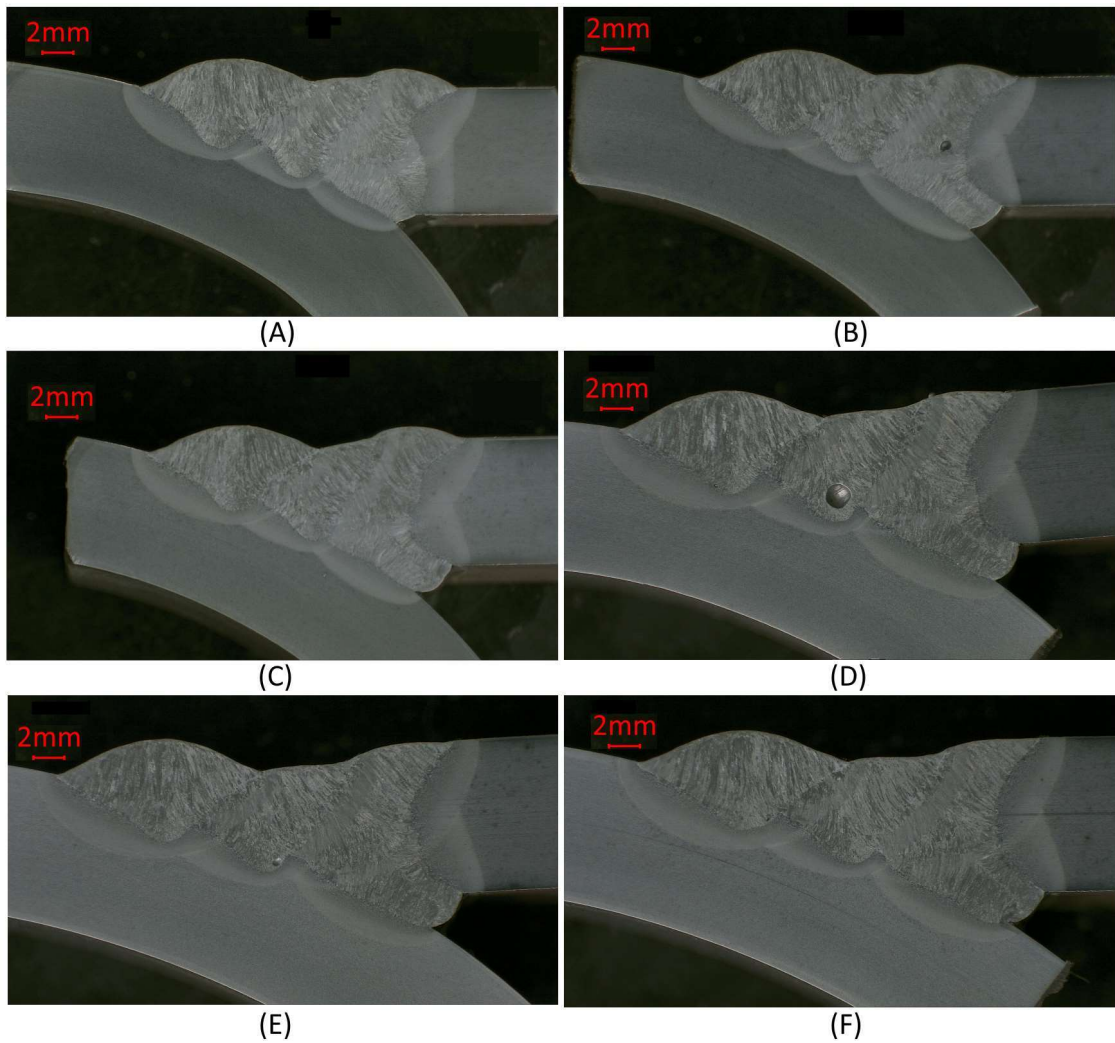
Figure 25. Macroscopic pictures of the welded samples made from S1100 with different bending radii: (A) r = 24 mm, r/t = 3; (B) r = 26 mm, r/t = 3.25; (C) r = 28 mm, r/t = 3.5; (D) r = 30 mm, r/t = 3.75; (E) r = 37 mm, r/t = 4.6; (F) r = 40 mm, r/t = 5.

Materials used as base metals in this study are newly developed S700MC and S1100 developed by SSAB. Specifications of these steels according to their manufacturer are presented in section 2.1. According to some earlier studies, the microstructure of these steels is a mixture of diverse types of bainite, martensite, and occasionally self-tempered martensite. (Guo, et al., 2015; Guo, et al., 2016; Górka, 2015; Kurc-Lisiecka, 2017; Kurc-Lisiecka, et al., 2017)

4.1 S700MC

Figure 26 shows the microstructure of S700MC in its as received condition. According to this figure, microstructure of S700MC consists of a mixture of bainite and martensite, which are in packets extended to prior austenite grain boundaries. In addition to these features, some smooth areas with straight and wavy boundaries (dashed area in figure 26) can be seen in the microstructure. According to Navarro-López et al. (2017, pp. 248-256), although these laths does not have an acicular morphology, their nature can be considered as bainitic. Few elongated bright blocks are also visible along the prior austenite grain boundaries and between bainitic ferrite laths in figure 26.B (indicated by white short dashed arrows). As stated by Navarro-López et al. (2017, p. 250), these blocks are possibly islands of retained austenite entrapped between boundaries of different microstructural features. However, unlike TRIP steels, the amount of this phase in S700MC is not significant enough to have a considerable role on its properties.

Microstructural features of one of the cold-formed specimens is presented in figure 27. According to this figure, similar to its as received condition, microstructure of the bended specimen is a mixture of bainite and martensite. Furthermore, due to its prior deformation, microstructural features of the pre-strained material are more packed with an orientation different from the virgin (as received) material. In other words, laths of martensite and bainite in the cold formed steel are oriented according to the direction of its prior bending process. This change of the direction can alter the interaction between the microstructure and loads applied on the material.

In addition to bending, welding and its resultant heat input have some significant effects on the microstructure of base metals. Majority of these effect are focused along its fusion zone and through the heat affected zone. Microstructure and characteristics of the heat affected zone depend on the type of material, its processing history, and the amount of heat input. To investigate the microstructure of the heat affected zone, the first step is to mark its boundaries by checking a specific material property. Hardness values are usually measured to indicate HAZ boundaries in a welded joint. To do so, hardness profiles of the welded samples made of S700MC are presented in figures 28 to 31.
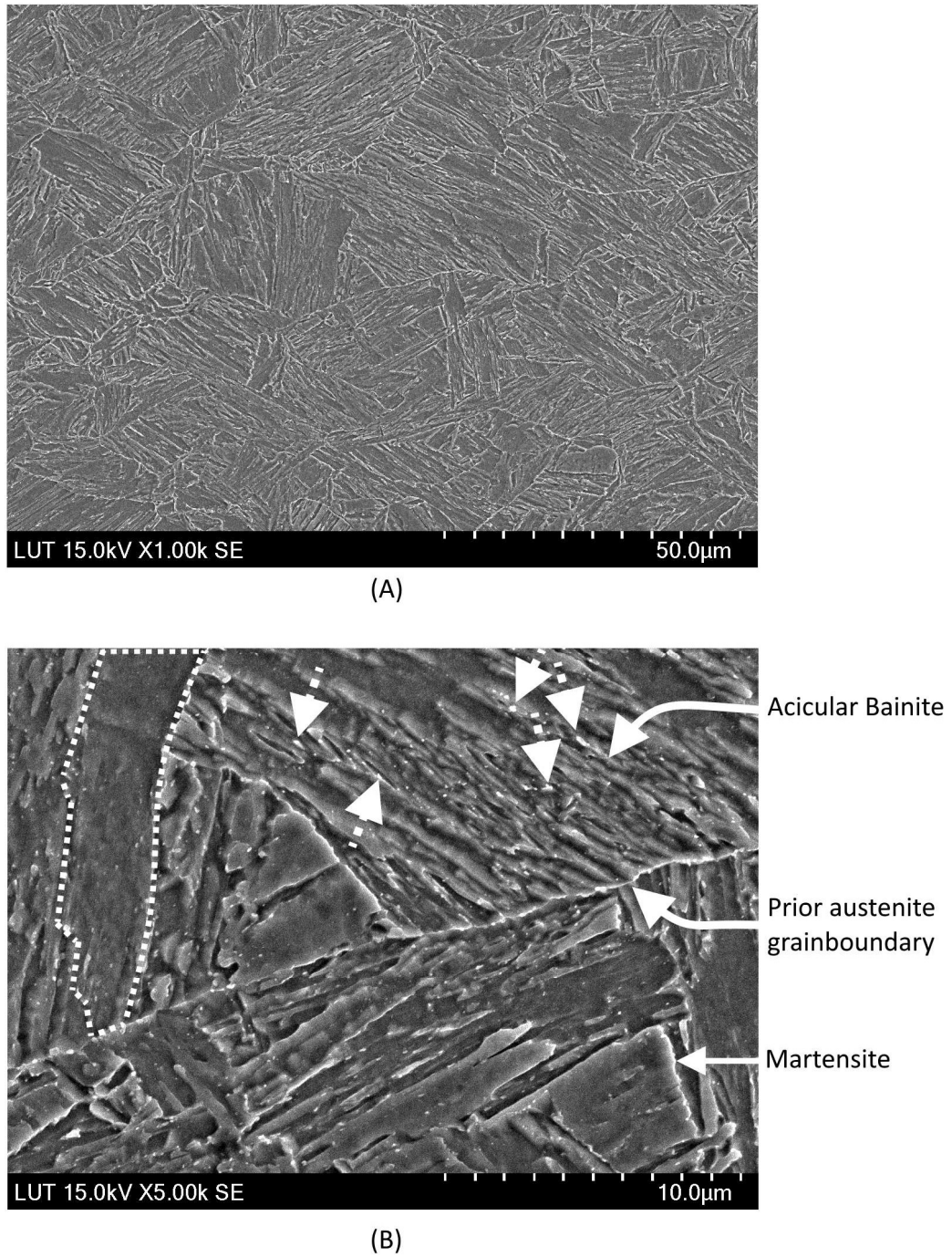
Figure 26. Microstructure of S700MC (as received): (A) Magnification 1000×; (B) magnification 5000×.
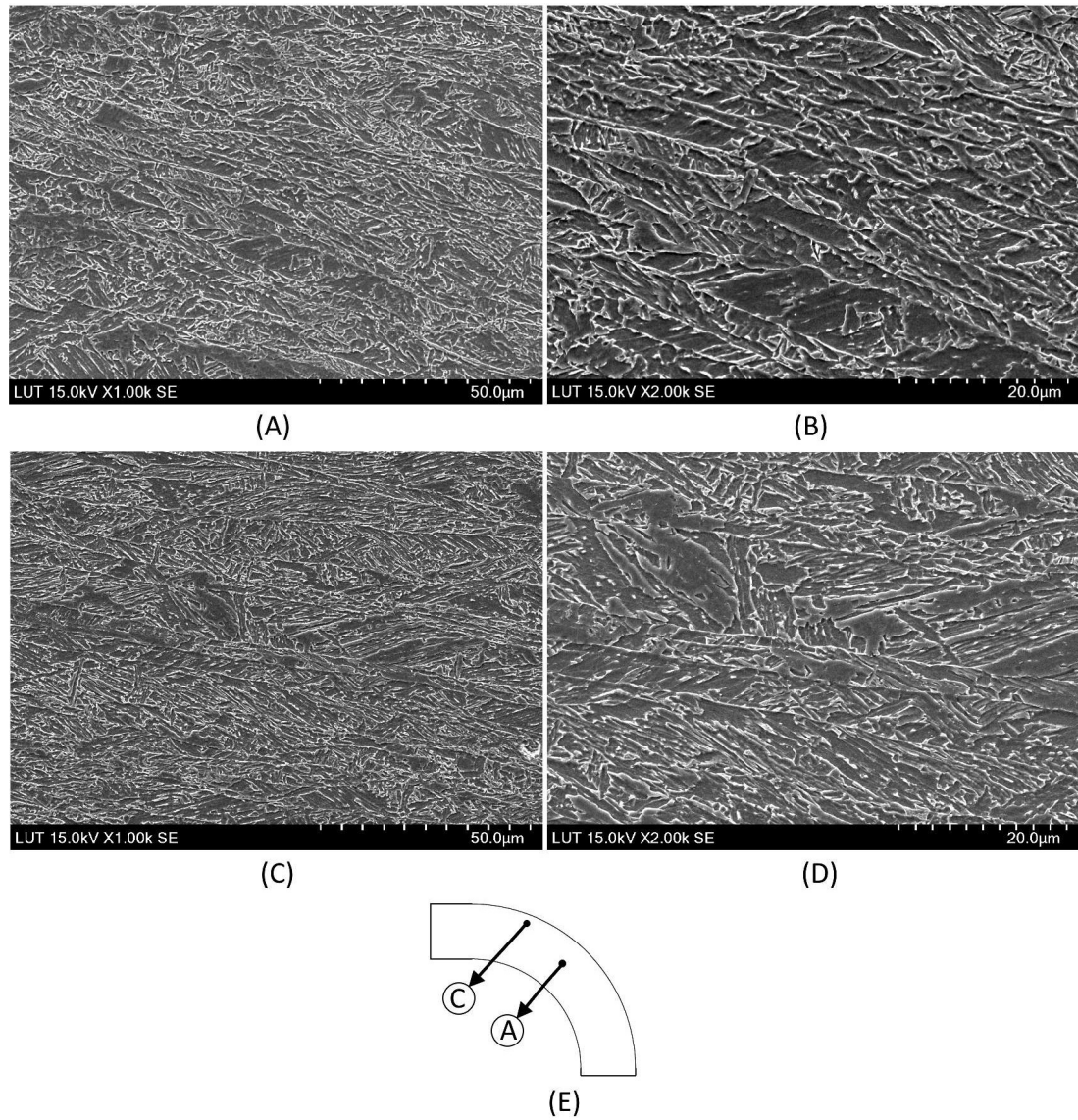
Figure 27. Microstructure of the cold formed S700MC with *r*/*t* = 2: (A & B) on the neutral axis (minimum pre-strain); (C & D): near the outer surface (maximum pre-strain); (E) schematic view of the location of investigated points.
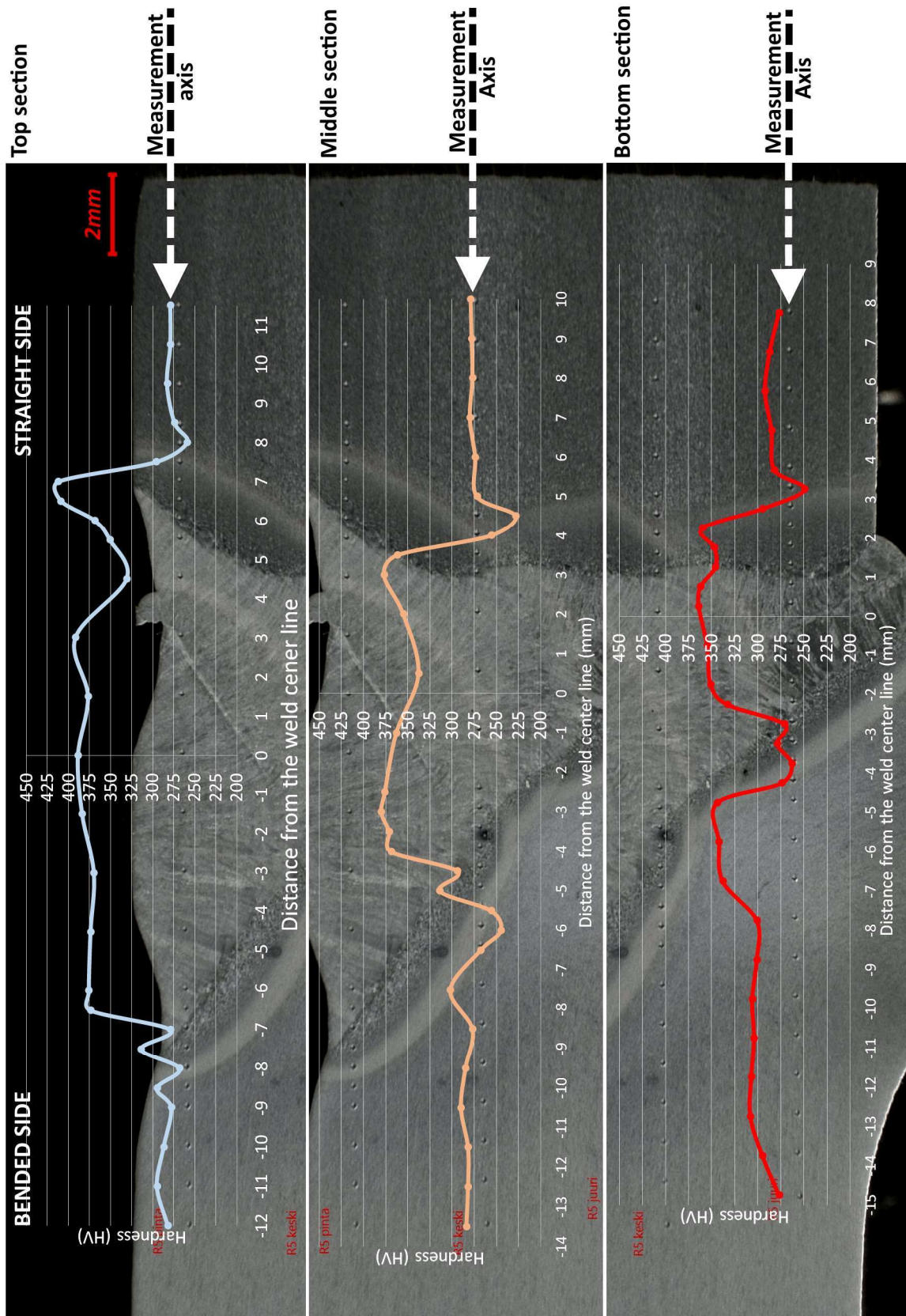
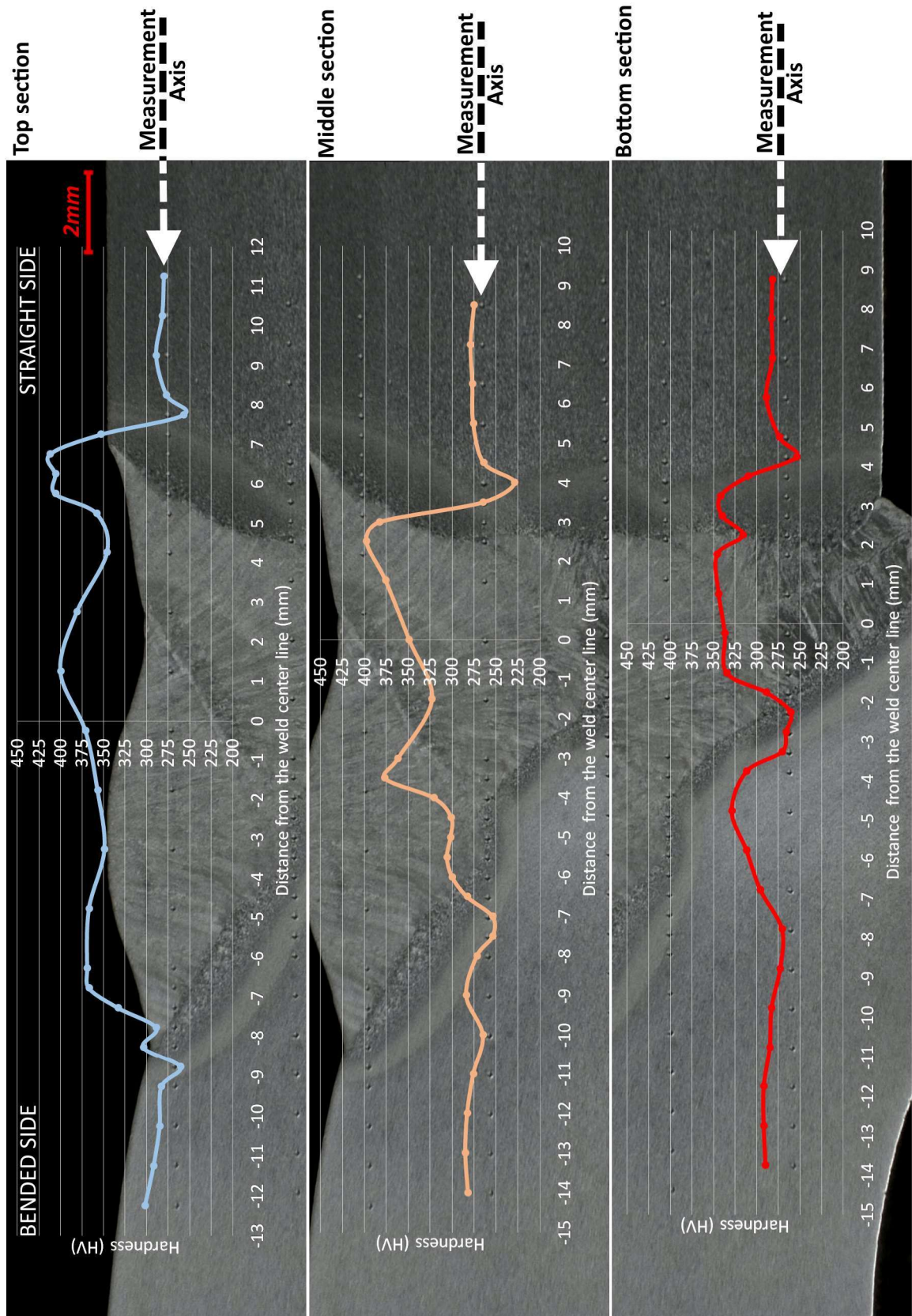**Figure 28.** Hardness profiles of S700MC welded joint with *r* = 5 mm and *r*/*t* = 0.5 on its bended side.

Figure 29. Hardness profiles of S700MC welded joint with *r* = 10 mm and *r*/*t* = 1.0 on its bended side.
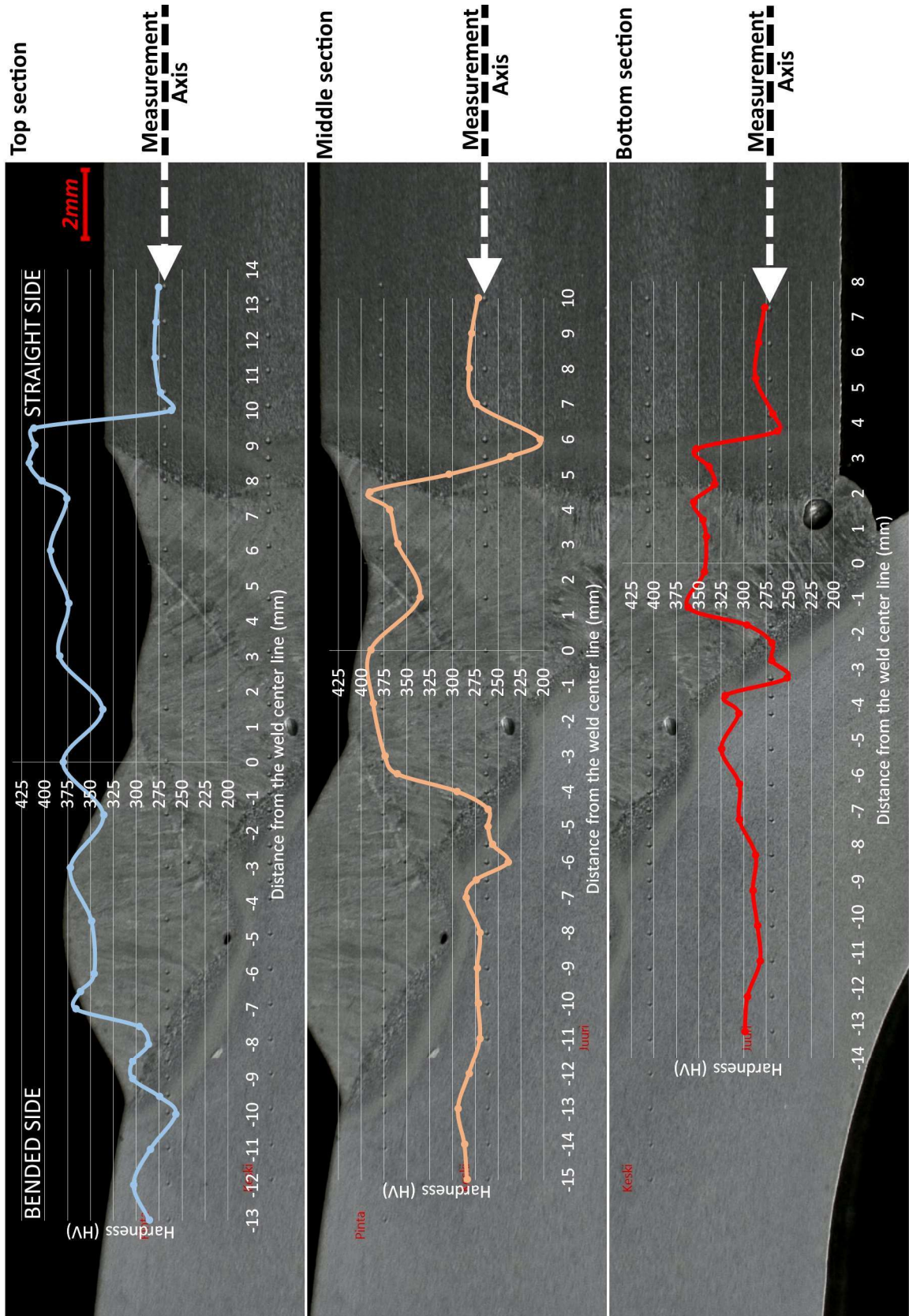
Figure 30. Hardness profiles of S700MC welded joint with *r* = 15 mm and *r/t* = 1.5 on its bended side.

53
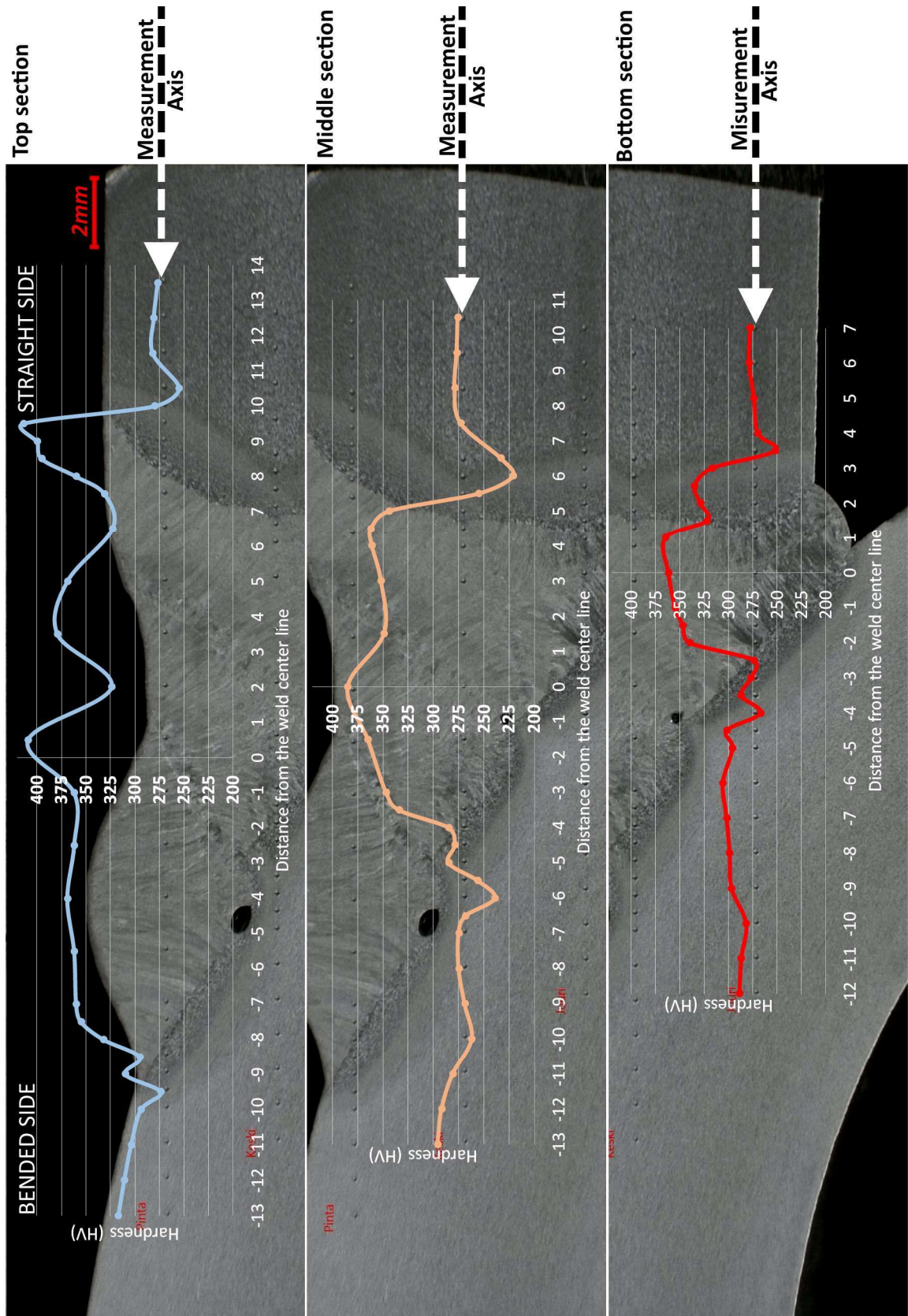
Figure 31. Hardness profiles of S700MC welded sample with *r* = 20 mm and *r*/*t* = 2.0 on its bended side.

According to these figures, fusion zones had the highest hardness values in all the welded joints. However, these values do not represent the hardness characteristics of the welded S700MC, since the FZs are made of low alloy steel Böhler alform® 700-MC as the matching filler material. Heat affected zones of all the welded passes showed the typical pattern of (U)HSSs. HAZ in these steels comprises of four distinct regions, which from FZ to base metal are coarse grain HAZ (CGHAZ), fine grain HAZ (FGHAZ, also known as normalized zone), intercritical HAZ (ICHAZ, also known as partially transformed zone), and subcritical HAZ (SCHAZ, also known as annealed zone). Figure 32 summarizes these sub-regions according to data provided by the manufacturer (SSAB 2016b, pp. 31-33.).
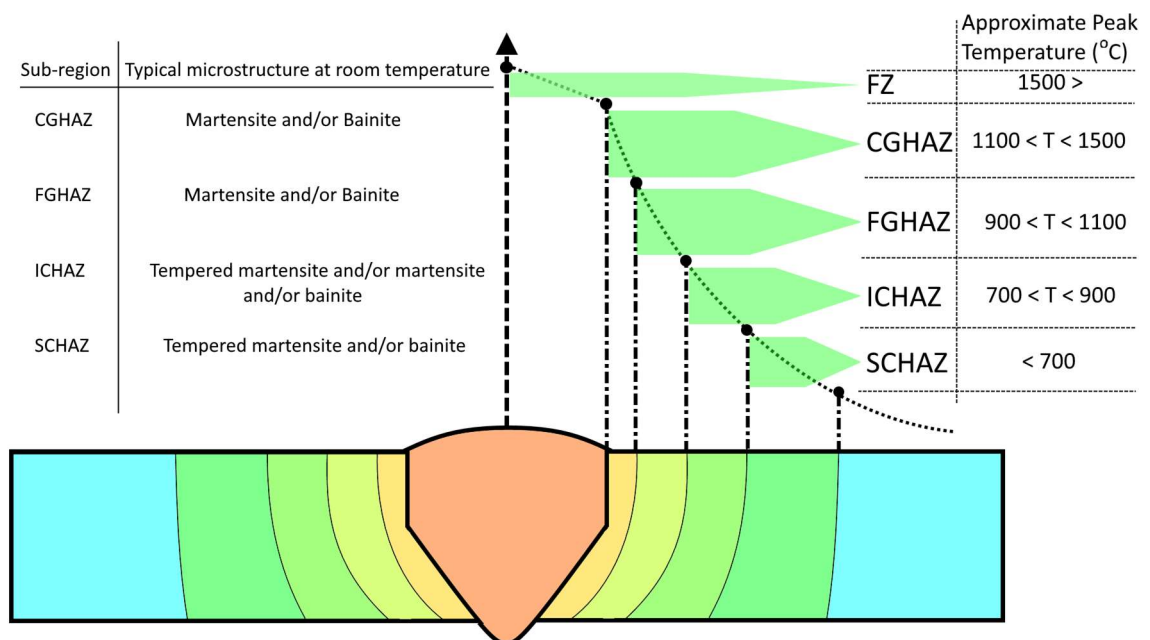
Figure 32. Typical HAZ sub-zones and their characteristics; data from SSAB (2016b, p. 31).

Hardness profiles of the welded sample with $r/t = 2$, according to their respective microstructures, are presented in figure 33. According to this figure, microstructure of the fusion zone (alform® 700-MC) was completely martensitic. By moving from the fusion line into the HAZ, the microstructure changed into a mixture of bainitic ferrite and martensite until it matched the microstructure of the base metal. Although the entire HAZ area seemed to be a mixture of bainite and martensite, the ratio, texture size, and roughness of these phases were different in every HAZ sub-zone. These microstructural differences are discussed later in this section.
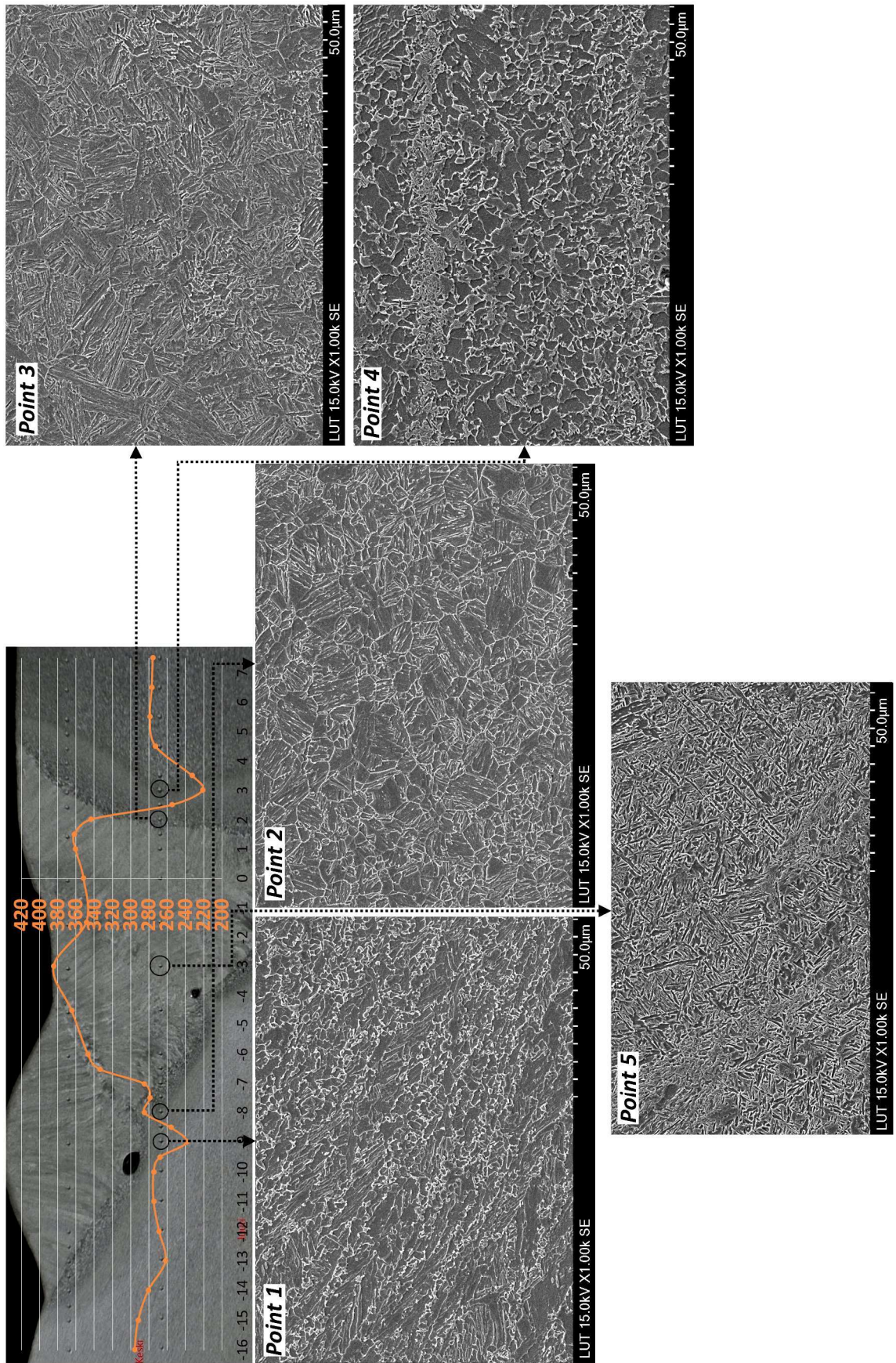
Figure 33. Hardness values and microstructures from the weld center line into the HAZ (S700MC; *r*/*t*=2).

As shown in figures 28 to 31, hardness values of cold-formed base metals were higher than their virgin counter parts. According to the previous studies, mentioned in section 2.3.1, these higher values can be attributed to the higher dislocation densities of cold-formed metals and their strain hardening as the consequences of their earlier cold-forming. Although the hardness trends were the same for all the cold-formed and virgin materials, the range of hardness fluctuations were quite different.

Microstructures of sub-zones with the hardness peak values (next to the weld metal) are presented in figure 34. According to this figure, the hardest region on the virgin side was a mixture of martensite and bainite, while its counterpart region on the cold formed side was mainly made of bainite. These different microstructures resulted in different peak hardness values on each side (higher hardness on the virgin side with the martensite-bainite mixture). These different values can be attributed to the effects of prior cold-forming, multi-pass welding, or both simultaneously.

In current study, areas next to the fusion lines experienced full austenitizing and rapid subsequent cooling. Studies show that prior deformation results in smaller austenite grains after austenitization, and the finer austenitic microstructure decreases both martensite and bainite start temperatures. Therefore, under a specific cooling rate, fine grain austenite can be more favorable toward austenite to bainite transformation and hinder martensite formation. (Yang & Bhadeshia 2009, pp. 1-6; Kundu & Chakraborti 2014, pp. 1141-1147; Goli-Oglu, Éfron & Morozov 2013, pp. 294-297.) In conclusion, areas next to the fusion line in the pre-strained side included more bainite and were relatively softer in comparison to the virgin side. According to figure 35, by increasing the degree of cold forming and pre-strain, these adjacent areas became softer consequently, which is in agreement with the previous evaluation.

Both prior deformation and thermal cycles caused by multi-pass welding can have a role in the differences between peak hardness values on the cold formed sides of the joints. It should be noted that the samples with the highest level of pre-strain ($r/t = 0.5$ and $r/t = 1$) also had the lowest peak hardness values, although they were welded by a lower heat input (table 19). Thus, regarding the hardness peak values, the role of prior deformation on them was more prominent than the effect of welding heat input.
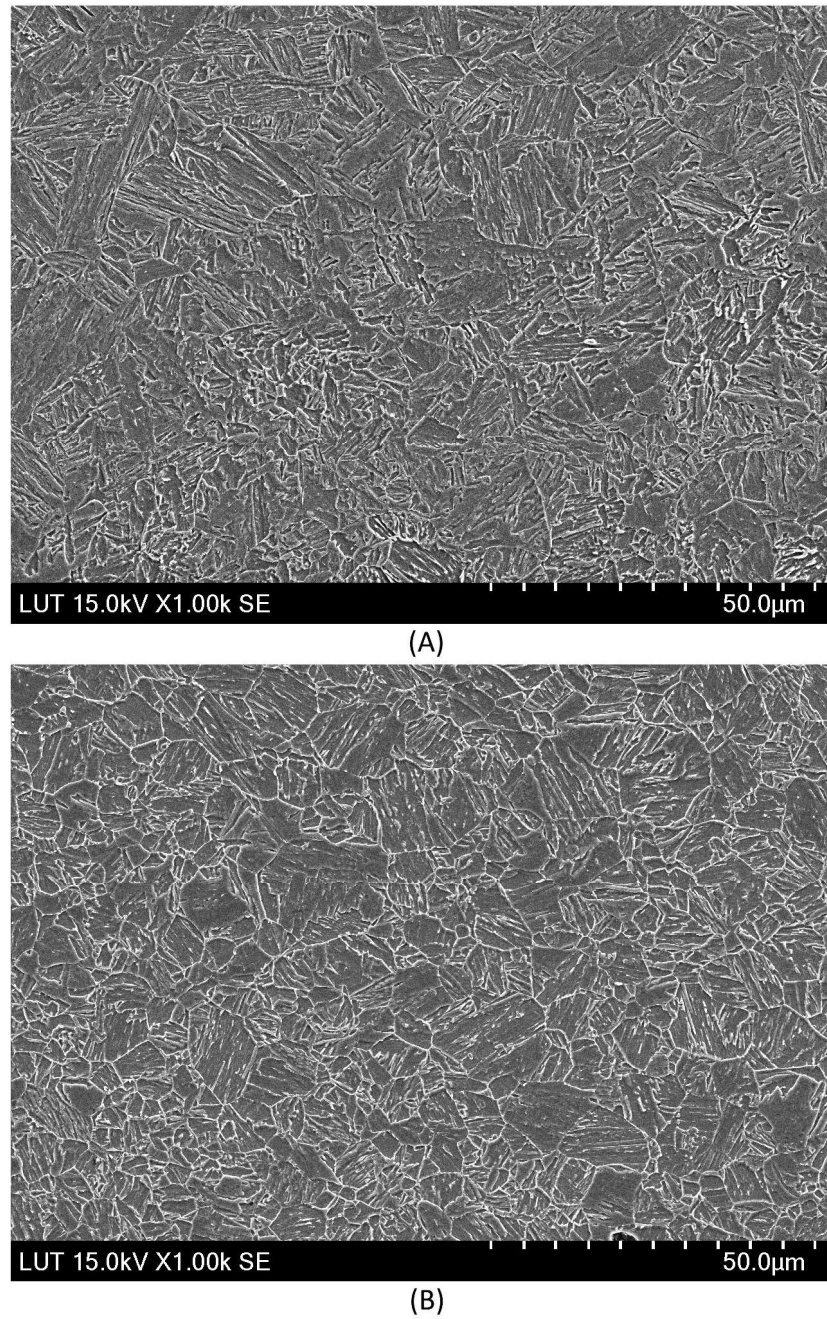
Figure 34. Microstructural features of HAZ sub-zones with the highest hardness values (next to the fusion line) of: (A) Virgin base metal; (B) cold-formed base metal with $r/t = 2$ (middle section).
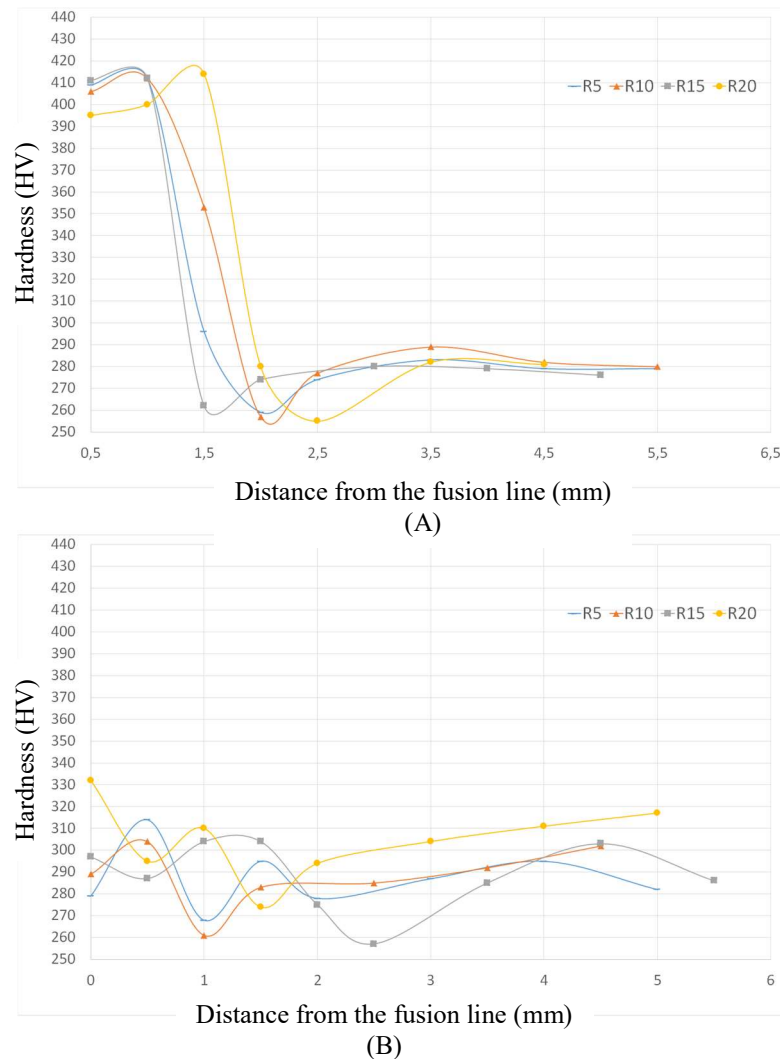
Figure 35. Hardness profiles of HAZs on the different sides of the joints: (A) virgin base metals; (B) cold formed base metals (S700MC, upper sections).

Microstructures of the softened zones are depicted in figure 36 in more details and higher magnifications. According to this figure, microstructures of the softened zones was a mixture of martensite, bainite, and small blocks of retained austenite (which are entrapped along the prior austenite boundaries). In this figure, some of the bainite laths and small islands of retained austenite are marked by white arrows and ovals respectively, and the rest of the background phase is considered as islands of martensitic/austenite (M/A), based on Navarro-López et al. (2017, p. 250) evaluations.

In addition to M/A, these granular shaped features are described as granular bainite in some other literature (Aydin 2014, pp. 15-22; Koo et al. 2003, pp. 10-17). Górka & Stano (2018, p. 8) also simply reported them as ferrite. However, considering the continuous cooling of

these sub-regions and their more moderate thermal gradient in comparison to areas closer to the fusion lines, granular bainite seems to be a more accurate description for these features. However, discovering the true nature of these granules requires more study and more sophisticated methods, such as electron backscatter diffractometry (EBSD) and transmission electron microscopy (TEM).
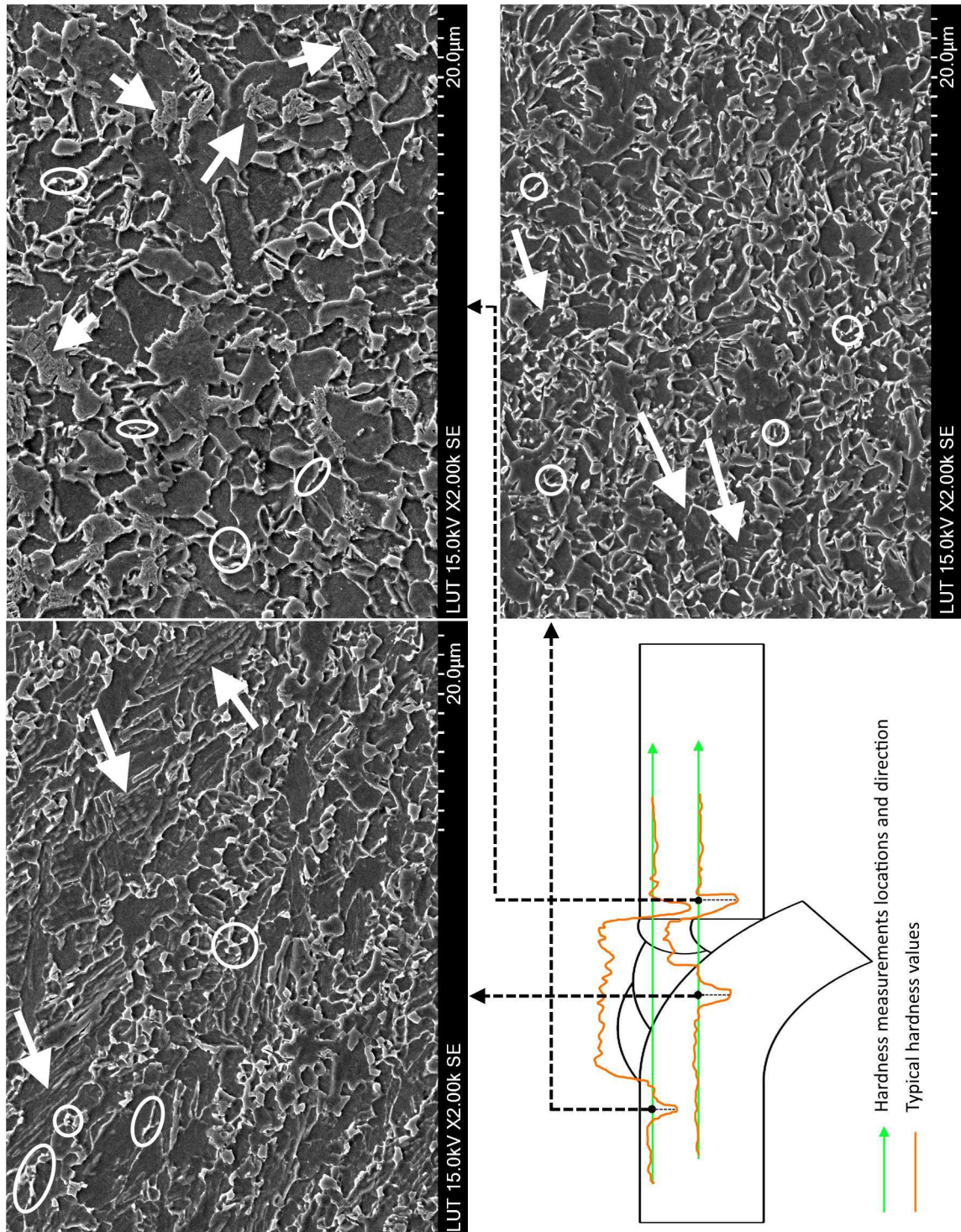

Figure 36. Microstructures of the softened zones (S700MC, *r*/*t* =2).

Although the softened regions on both sides of the welded joints comprised of a mixture of bainite and martensite, the ratio of these phases and the texture sizes of the microstructures were different on each side. In comparison to the cold-formed material, the virgin base metal had a higher martensite to bainite ratio, but its microstructural texture was coarser. This coarser microstructure may be the reason of more severe softening in the virgin side of the welded joints. In addition, some coarse precipitates were also visible inside of some sub-grain features (figure 36). According to Górka & Stano (2018, p.4), these phases might be (Ti,Nb)(C,N) particles.

In conclusion, pre-strained base metals had higher hardness values on their softened zones, while they had lower peak hardness values. This contradiction can be attributed to the partial transformation of the softened regions (unlike the zones with the peak hardness values, which undergo fully austenitization). Furthermore, to completely evaluate the reasons behind the different hardness profiles of cold-formed and virgin base metals, the role of different thermal cycles must also be considered. Thus, further study is required to have a thorough understanding of this matter.

Another microstructural feature, as can be seen in figure 36, was the different sizes of microstructural textures from the middle section and the upper section of the welded sample. The upper section, which did not experience reheating, showed a finer microstructure and also had a higher average hardness. These different hardness values and microstructures can be attributed to either prior cold-forming or multi pass welding. In conclusion, further study is required to evaluate, understand, and distinguish the effects of cold forming and heating on the hardness of the cold formed base metals.

Figure 37 shows the microstructural features along the fusion line on the virgin side of the joint. According to this figure, fully martensitic microstructure of the fusion zone (left side of the picture) changed into a feather like bainitic ferrite on the fusion line (dashed area). Next, the microstructure became a mixture of acicular ferrite (white arrows) and islands of martensite (black arrows) in the heat affected zone. The feathery shape of bainite (long parallel thin lines of bainitic ferrite) near the fusion line is attributed to the morphology of upper bainite in some literature (Bhadeshia & Christian 2015, pp. 1-15; Jayanti, 2018). Considering the carbon content of UHSSs, very high thermal gradients neat the fusion line,

and peak temperatures of this region, appearance of upper bainite along the fusion line was expected. Although both upper bainite and martensite were supposed to deteriorate the mechanical properties of HAZ, they did not aggravate plastic characteristics of the joint due to the low carbon content of S700MC (Górka & Stano 2018, p.8).
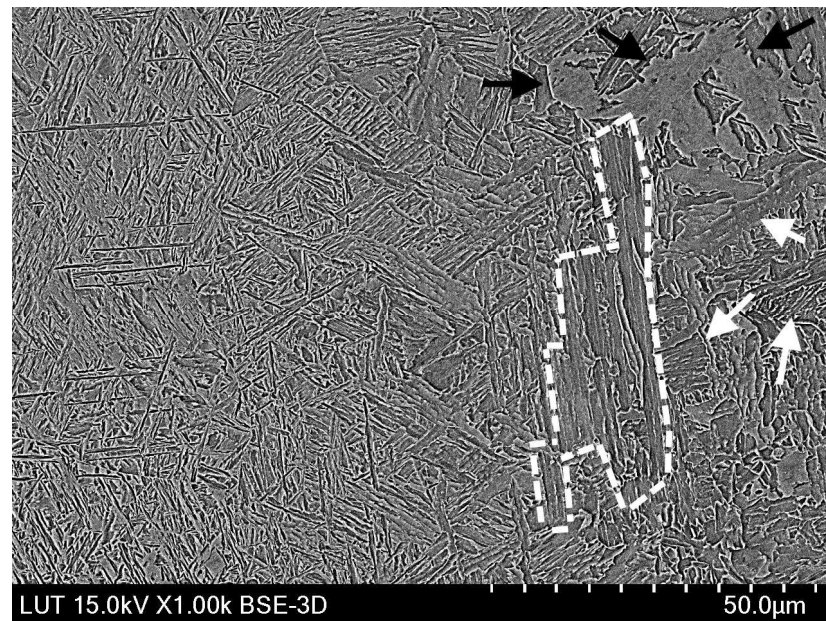

Figure 37. Microstructural features along the fusion line.

4.1.1 Uniaxial tensile tests of S700MC samples

Numerical results of the tensile tests carried out on S700MC welded samples are summarized in table 20, and their true stress-strain curves are presented in figure 38. In addition, visual data from ARAMIS DIC system are presented in figure 39 to measure the total displacements at the fracture moments. As can be seen in figure 39, none of the specimens failed from their weld metals. Furthermore, according to the table, welded samples with bending radii of 5 mm, 10 mm, and 15 mm fractured from the bended base metal, while the specimen with the bending radius of 20 mm fractured from the virgin side of the joint. It can be concluded specimens with the bending radii higher than the allowable values, as mentioned in the manufacturer specifications (parameter bendability in table 7)[4], had a premature failure. Their fracture was considered as premature and unfavorable due to their lower elongations (figures 38 and 39).

---

[4] According to EN 10149-2, Bendability of S700MC for bend angles equal to or less than 90° is $r = 2.5 \times t$; However, in this study, samples with $r = 2 \times t$ did not fracture from the bended side. Thus values recommended by the manufacturer (SSAB) seem to be more practical and less conservative.

According to table 20, yield strengths of the samples fractured from the bended side are higher than the virgin material, as expected according to section 2.3.1. However, they do not follow Karren's and its subsequent equations (equations 15 to 18). This contradiction can be attributed to the excess deformation of the bended base metals and/or recognized as a consequence of the welding process. Thus, using this approach to calculate the strengths of welded structures made of this type of steel in pre-strained condition is not recommended. Applicability of these equations and allowance criteria of such calculations in the structures made of S700MC require further study.

Table 20. Uniaxial tensile properties of the S700MC welded samples.

r/t on the deformed side of the weld	Yield strength (MPa)	Tensile strength (MPa)	Fracture displacement (mm)	Elongation (%)	Predicted yield strength according to Karren's equation (MPa)	Area of fracture
5	800	844	6.9	13.8	1070	Pre-strained base metal
10	812	864	7.0	14.0	970	Pre-strained base metal
15	815	880	6.9	13.8	920	Pre-strained base metal
20	795	871	7.6	15.2	880	Virgin base metal
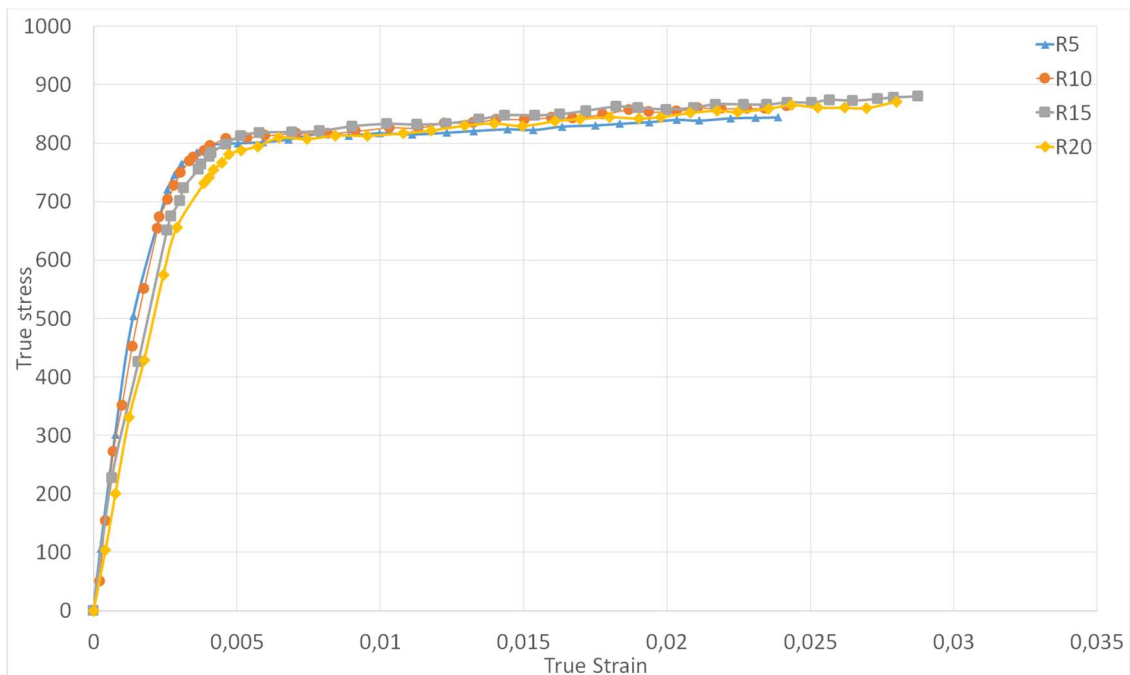
Figure 38. True stress-strain curves of welded S700MC specimens until their necking points, according to the bending radii of their bended base metals.
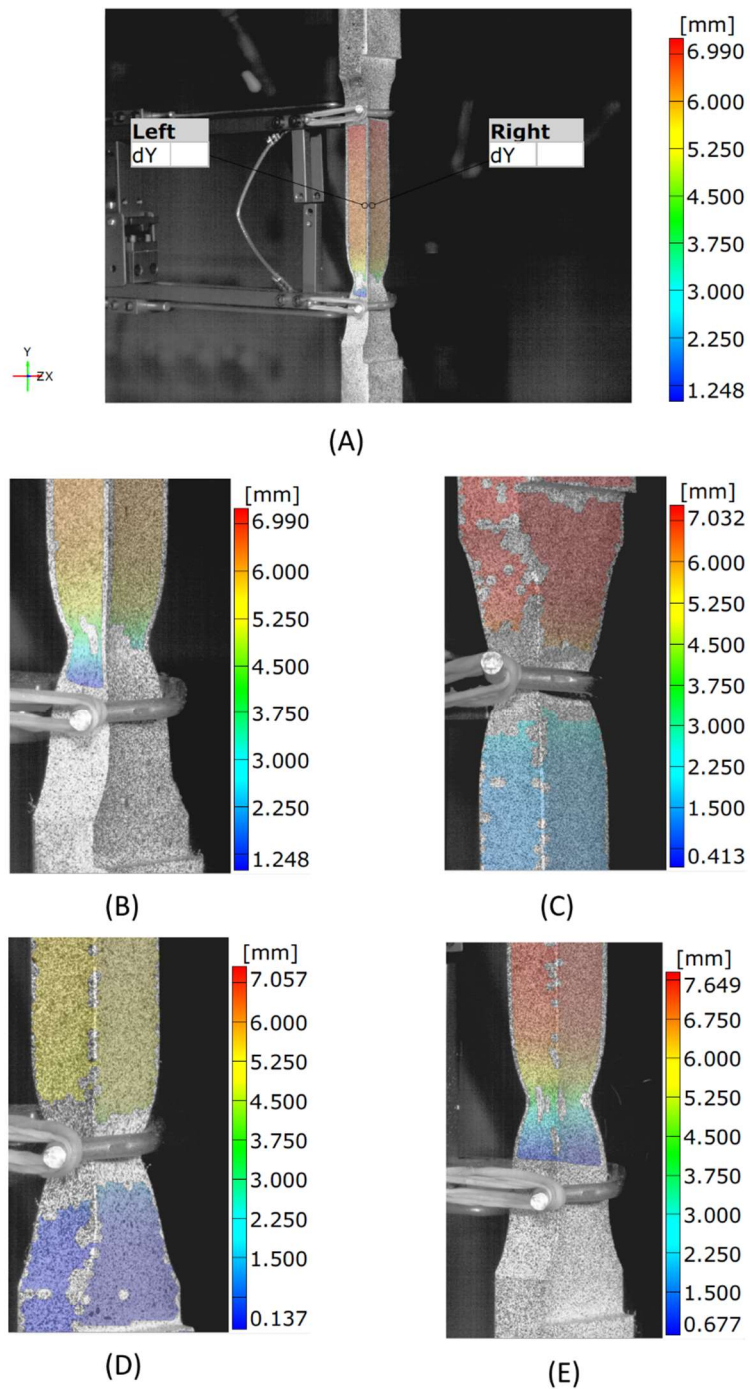
Figure 39. DIC data from ARAMIS, according to the bending radii of the pre-strained sides: (A) overal view of sample with 5 mm bending radius (B) focused view of $r = 5$ mm, (C) $r = 10$ mm, (D) $r = 15$ mm, (E) $r = 20$ mm

4.1.2 Notch toughness of S700MC samples

In this study, Charpy notch toughness test was carried out with notch positions in the HAZs, virgin base metals, and pre-strained base metals. The results are summarized in figure 40. According to this figure, bended materials had the lowest notch toughness, as expected according to section 2.3.1. Furthermore, notch toughness of the bended base metals increased by decreasing their r/t (degree of cold-forming or pre-strain). Similar conclusion can be caught from figure 41, since the sample with the least bending radius had the largest brittle area on its fracture surface and vice versa. However, correction factor ($s/S = 0.5$) did not seem to give some rational notch toughness values here, specifically for straight base metal (87 J). Thus, presented results in figure 40 are reliable just for comparison.
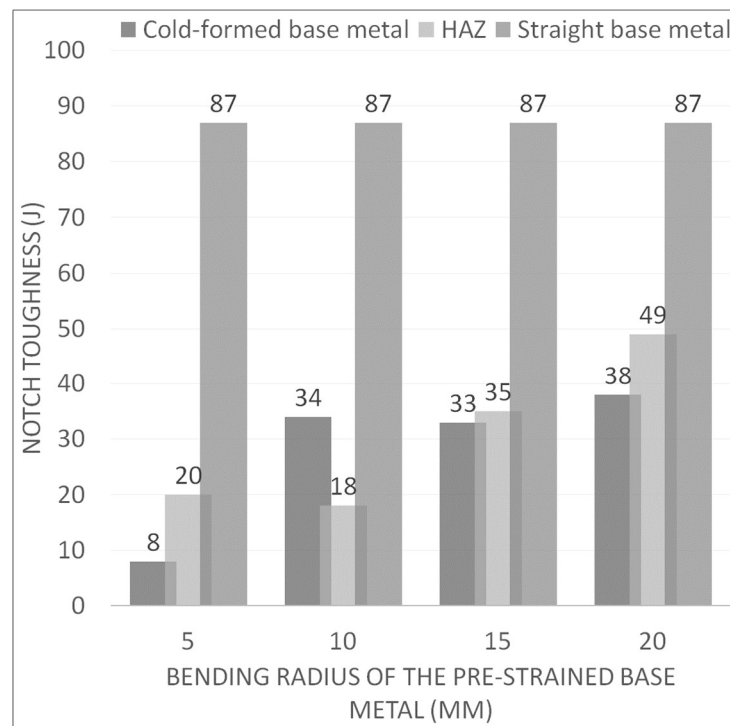
Figure 40. Notch toughness of different areas of the welded joints made of S700MC (notch root was 1 mm and 5 mm away from the fusion line for HAZ and base metal respectively).
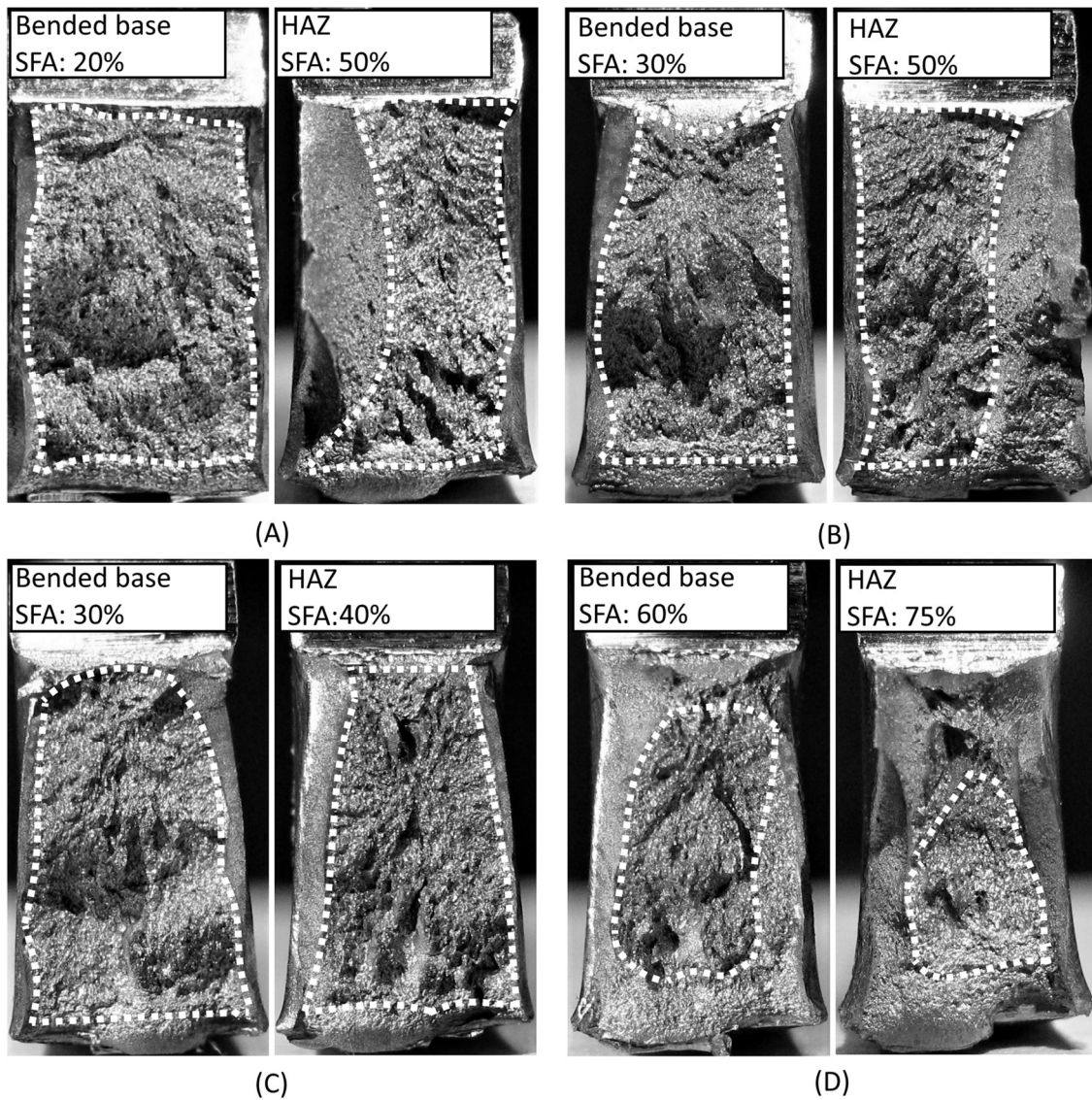
Figure 41. Fracture surfaces and proportion of shear fracture areas (SFA) for the bended sides of the welded joints according to their bending radius: (A) $r = 5$ mm, (B) $r = 10$ mm, (C) $r = 15$ mm, (D) $r = 20$ mm. Brittle fracture areas are indicated by white dashed lines.

4.2 S1100

Microstructure of S1100 in its as received condition is presented in figure 42. According to this figure, S1100 is a mixture of martensite and bainite, which consists of islands of martensite elongated according to the rolling direction and surrounded within a fine texture of acicular bainitic ferrite. By increasing the magnification to 5000×, small islands of retained austenite also appear along the prior austenite grain boundaries or between the bainitic ferrite acicular laths. These islands are indicated by white ovals in figure 42.B.

Microstructure of a bended specimen with $r/t = 3.25$ is presented in figure 43. According to this figure, unlike S700MC shown in figure 27, prior bending had some less significant effects on the density and orientation of the microstructural features in S1100, which can be due to the higher bending radii of S1100 specimens. As shown in figure 43, microstructure of the bended S1100 consisted of a mixture of martensite and bainite, similar to its as received condition. In addition, this martensitic-bainitic microstructure did not show a significant difference between the areas near the upper surface of the material (under maximum tensile strain) and the ones on its neutral axis (areas with minimum amount of strain).

Another microstructural feature of S1100, which is shown in figure 43.F with white dotted lines, was the existence of some lath shaped elongated morphologies containing irregular patterns of sporadic carbides within them. According to Navarro-López et al. (2017, p. 250), this type of morphology has a martensitic origin and, due to the presence of carbides, can be considered as tempered martensite. However, scarcity and small lath size of this morphology make it difficult to detect in magnifications lower than 10000×; thus, its effect on the mechanical properties of S1100 can be neglected.
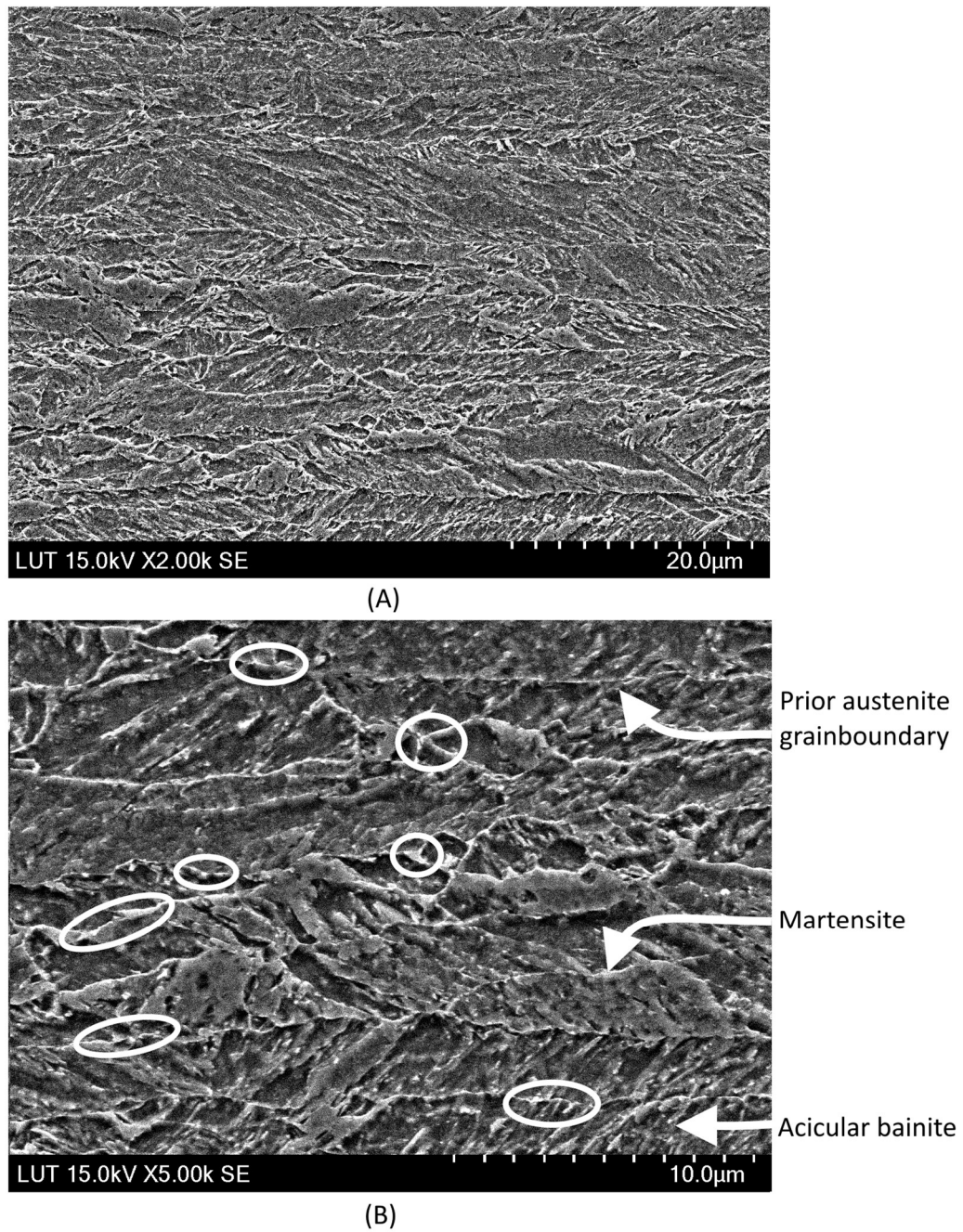
Figure 42. Microstructure of S1100 in its as received condition: (A) 2000×; (B) 5000×.
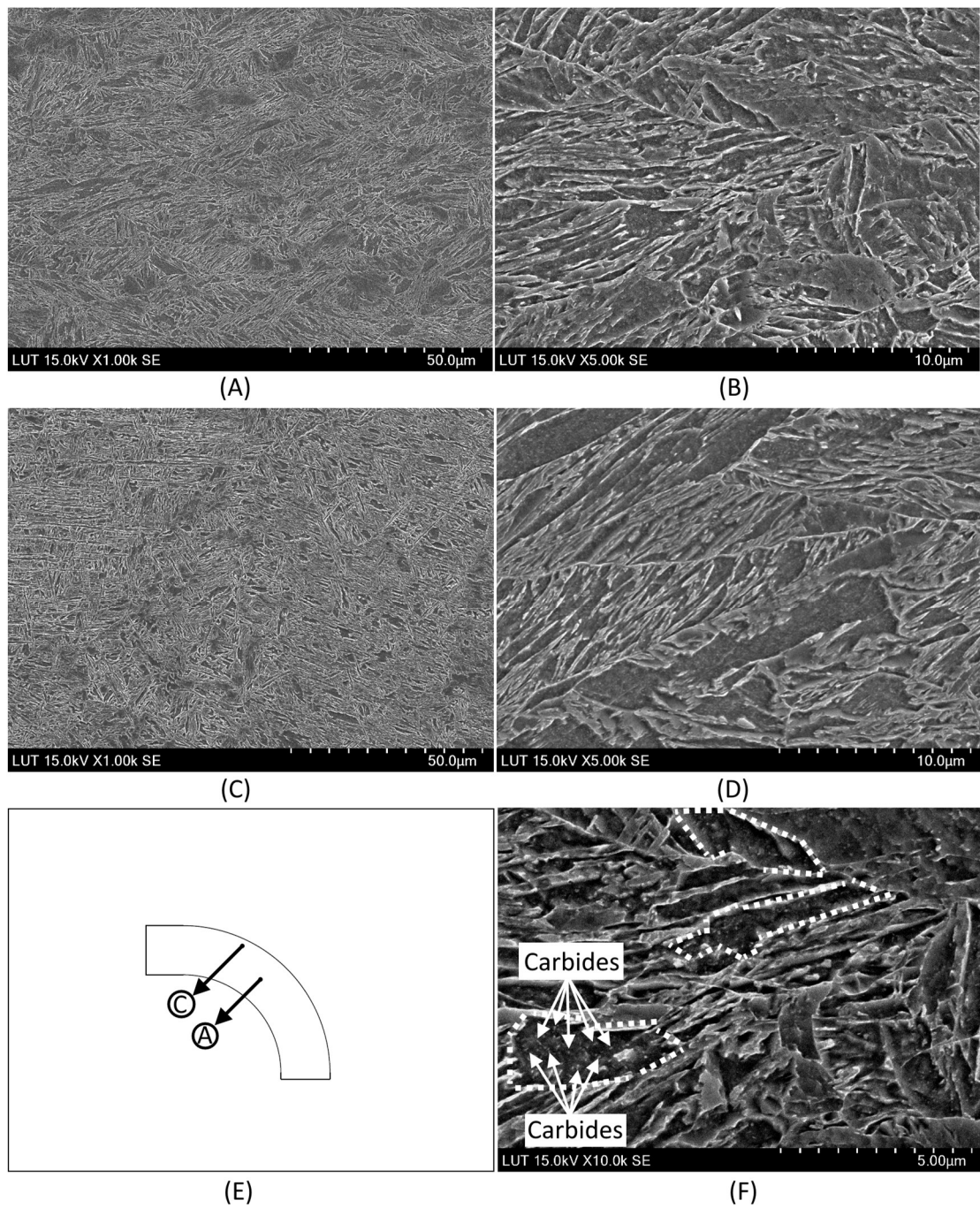
Figure 43. Microstructural features of the bended base metal with r/t = 3.25: (A & B) on the neutral axis; (C & D) near the outer surface; (E) schematic views of locations of the investigated points; (F) microstructure of S1100 in magnification 10000x.

Hardness profiles of the welded samples are presented in figures 44 to 50. According to these figures, in all welded samples, average hardness values of the bended base metals were higher than other parts of the joints. These higher values were more apparent along the final welding passes of the joints, which did not experience reheating unlike the earlier ones. As discussed in section 2.3.1, higher average hardness of the bended base metals in comparison to their virgin counter parts can be attributed to the effects of prior cold work on their mechanical properties. In addition, average hardness values of the fusion zones were lower than the bended base metals. This trend was expected since an undermatching filler material was used for the welding procedure.

According to figures 44 to 50, hardness profiles of S1100 along the cross sections of the welded joints are more uniform than the ones belonging to S700MC. In addition, average hardness values in the middle sections (reheated zones) and upper sections were similar to each other in the base materials (virgin and cold-formed). However, average hardness of the fusion zones decreased along the middle sections. This decrease in the hardness might be due to the effects of reheating during multi-pass welding.

Hardness profile of middle section of the welded sample with $r/t = 3.25$ is presented in figure 50, accompanied with the microstructures of its sub-zones. According to this figure, microstructure of the fusion zone (Union X96) was a mixture of fine textured bainite and martensite. In addition, microstructures of the HAZs, on both sides of the joint, were a mixture of bainite and martensite. However, majority of the bainitic ferrite in the base metals seemed to be coarser than the one in the fusion zone, and based on its rough appearance, it could be considered as acicular ferrite.

Similarity of microstructures in the HAZ sub-zones and the FZ, as shown on figure 50, might be a reason for the more uniform hardness fluctuations in S1100 welded samples (in comparison to S700MC welded samples discussed earlier). Another reason for this matter might be the lower degrees of cold-forming for S1100 specimens (their higher r/t ratios). Regarding the HAZ sub-zones, there were some differences between the ratio and texture size of the phases belonging to the ones with the highest hardness values (points 2 and 3 in figure 50) and the ones with the lowest hardness values (points 1 and 4 in figure 50). These differences are discussed in more details later in this section.
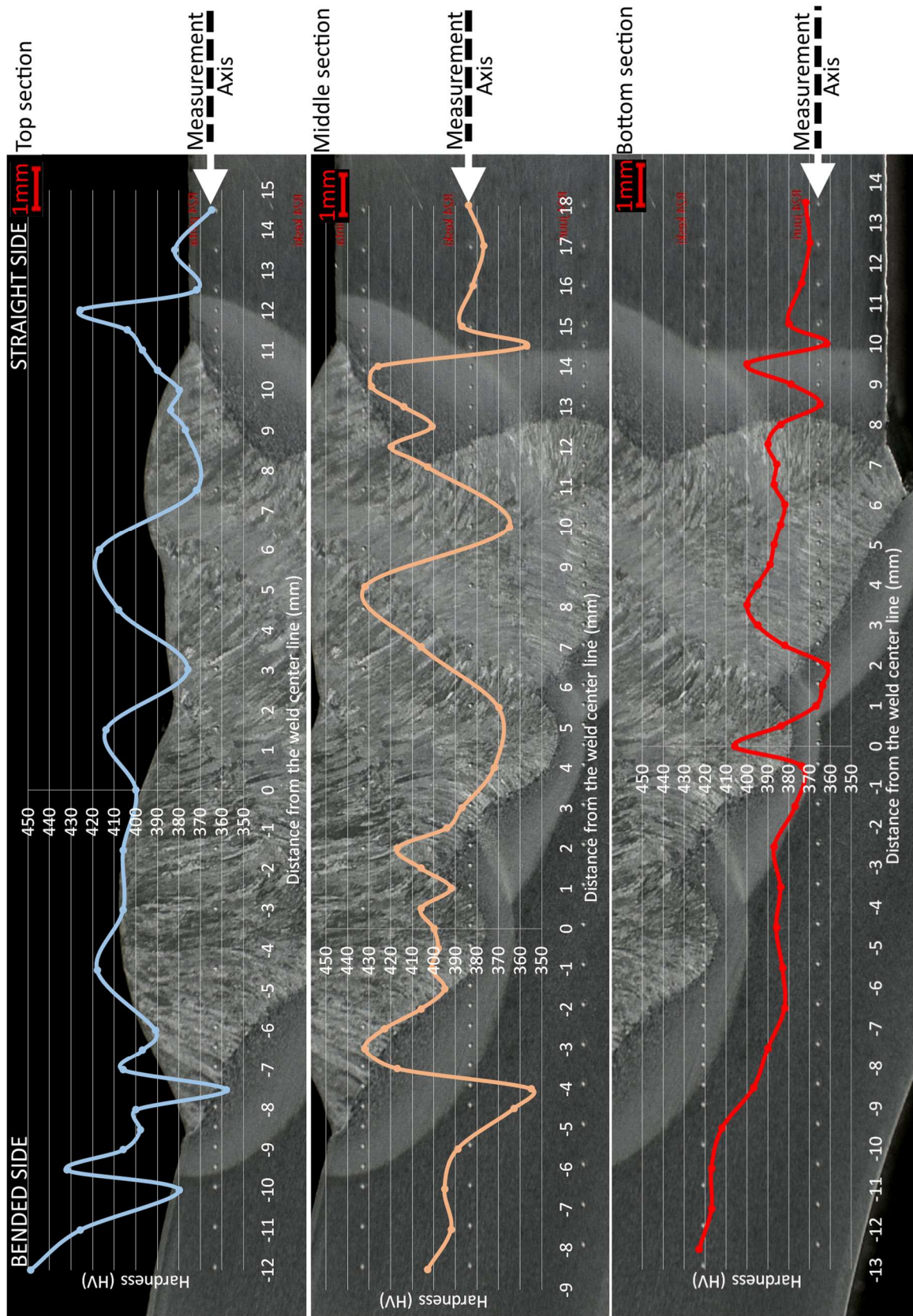
Figure 44. Hardness profiles of S1100 welded sample with *r* = 24 mm and *r/t* = 3 on its bended side.
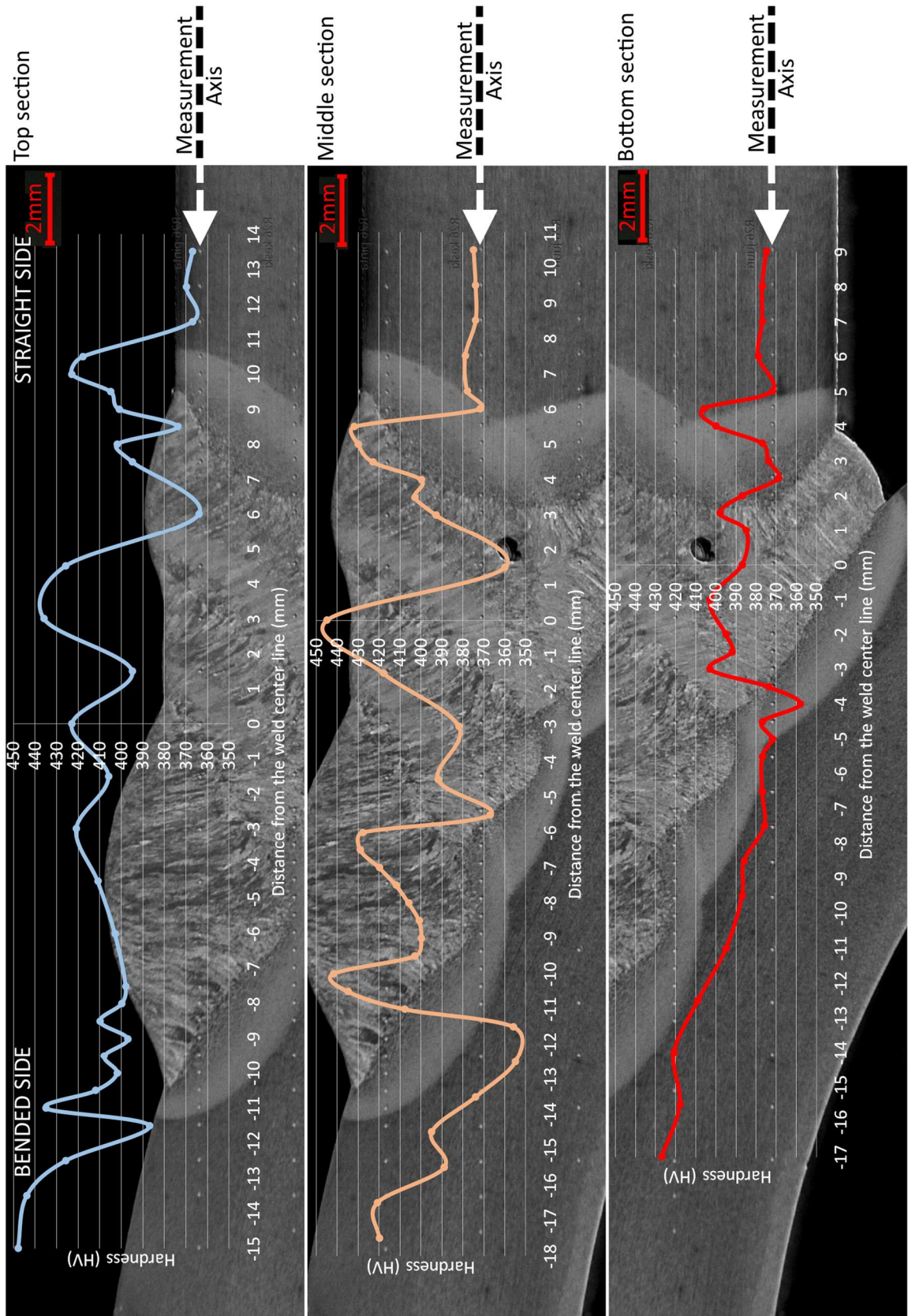
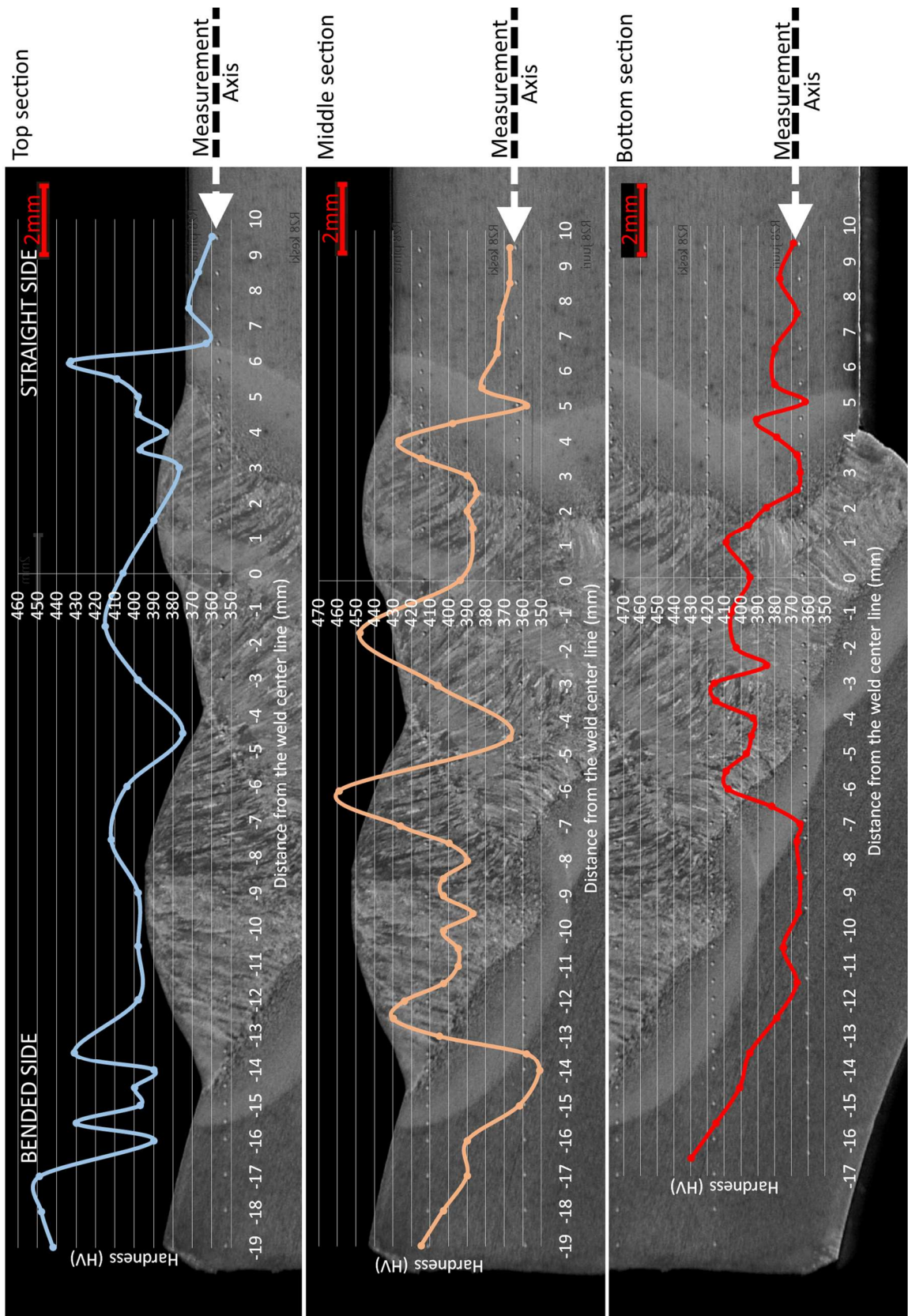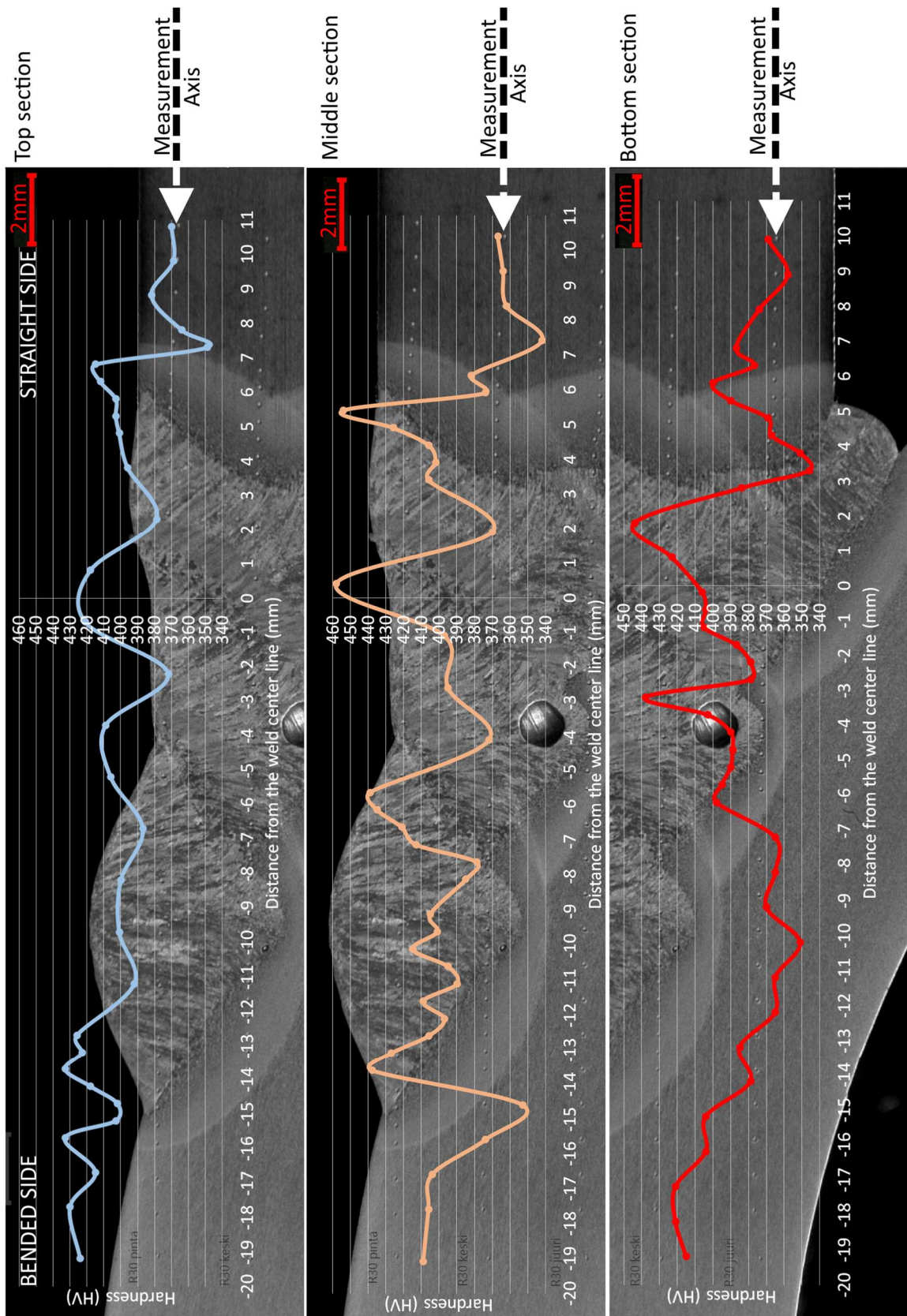**Figure 45.** Hardness profiles of S1100 welded sample with *r* = 26 mm and *r/t* = 3.25 on its bended side.

72

Figure 46. Hardness profiles of S1100 welded sample with *r* = 28 mm and *r*/*t* = 3.50 on its bended side.

Figure 47. Hardness profiles of the S1100 welded sample with *r* = 30 mm and *r*/*t* = 3.75 on its bended side.
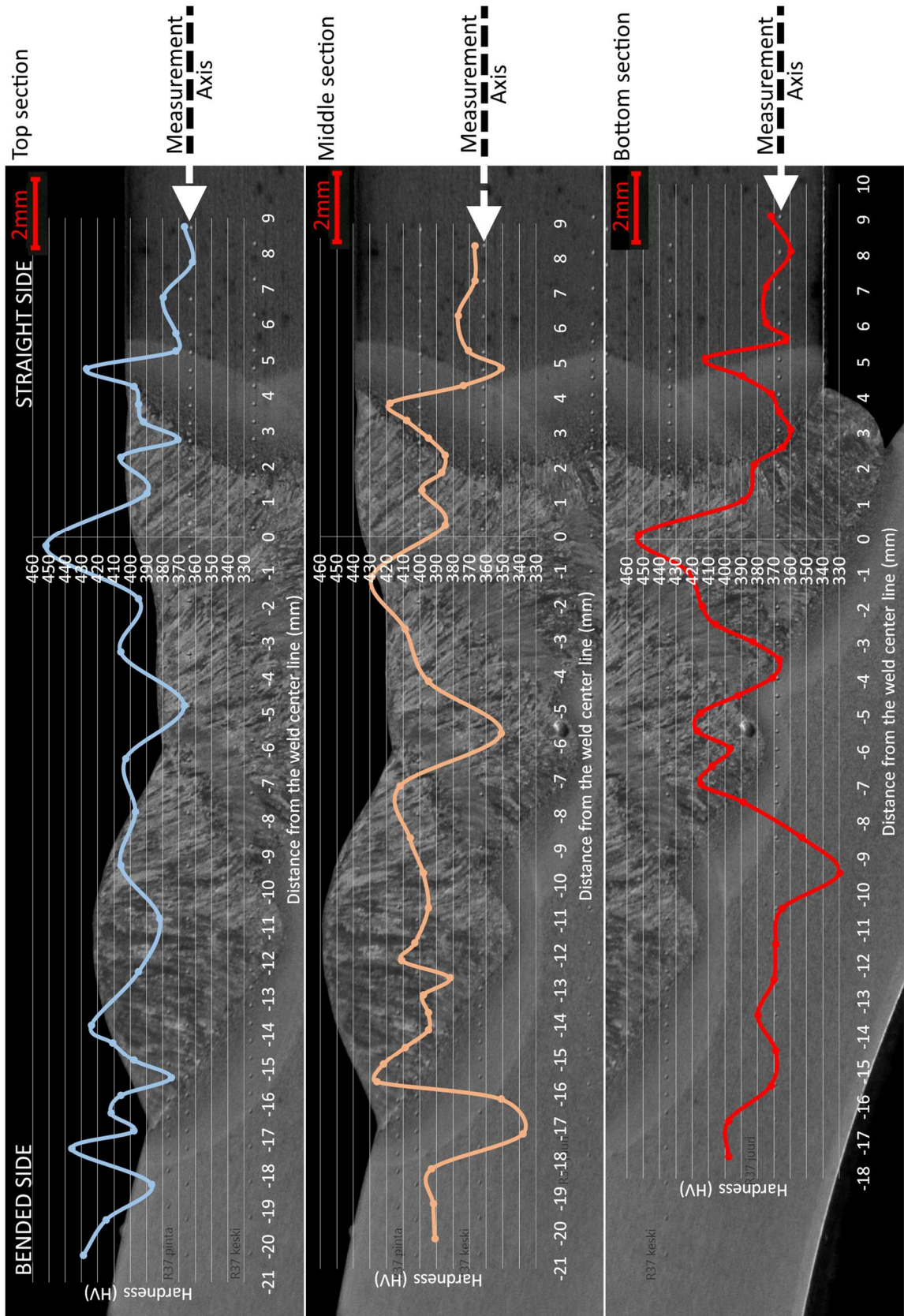
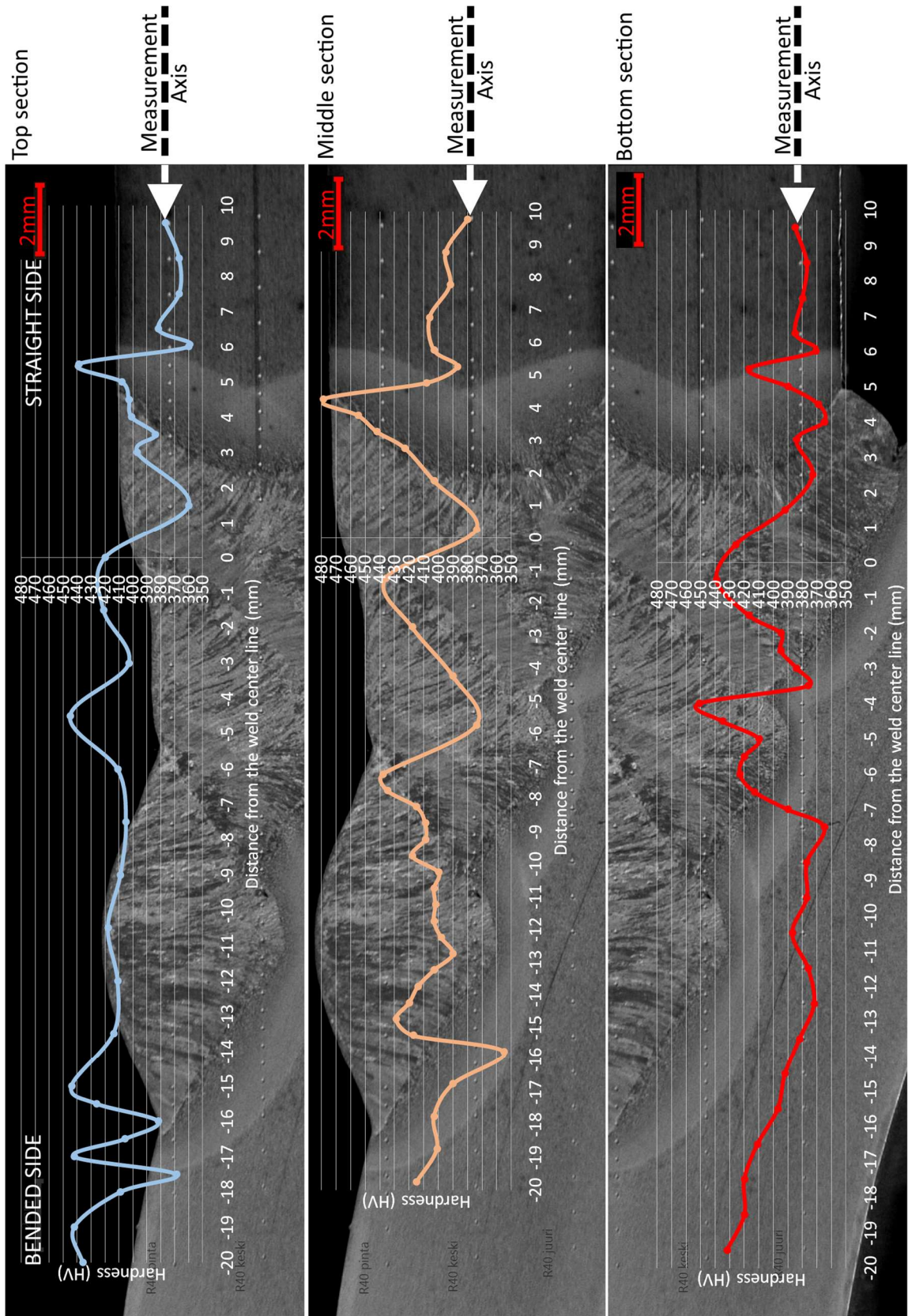**Figure 48.** Hardness profiles of the S1100 welded sample with *r* = 37 mm and *r/t* = 4.60 on its bended side.

Figure 49. Hardness profiles of the S1100 welded sample with *r* = 40 mm and *r*/*t* = 5.00 on its bended side.
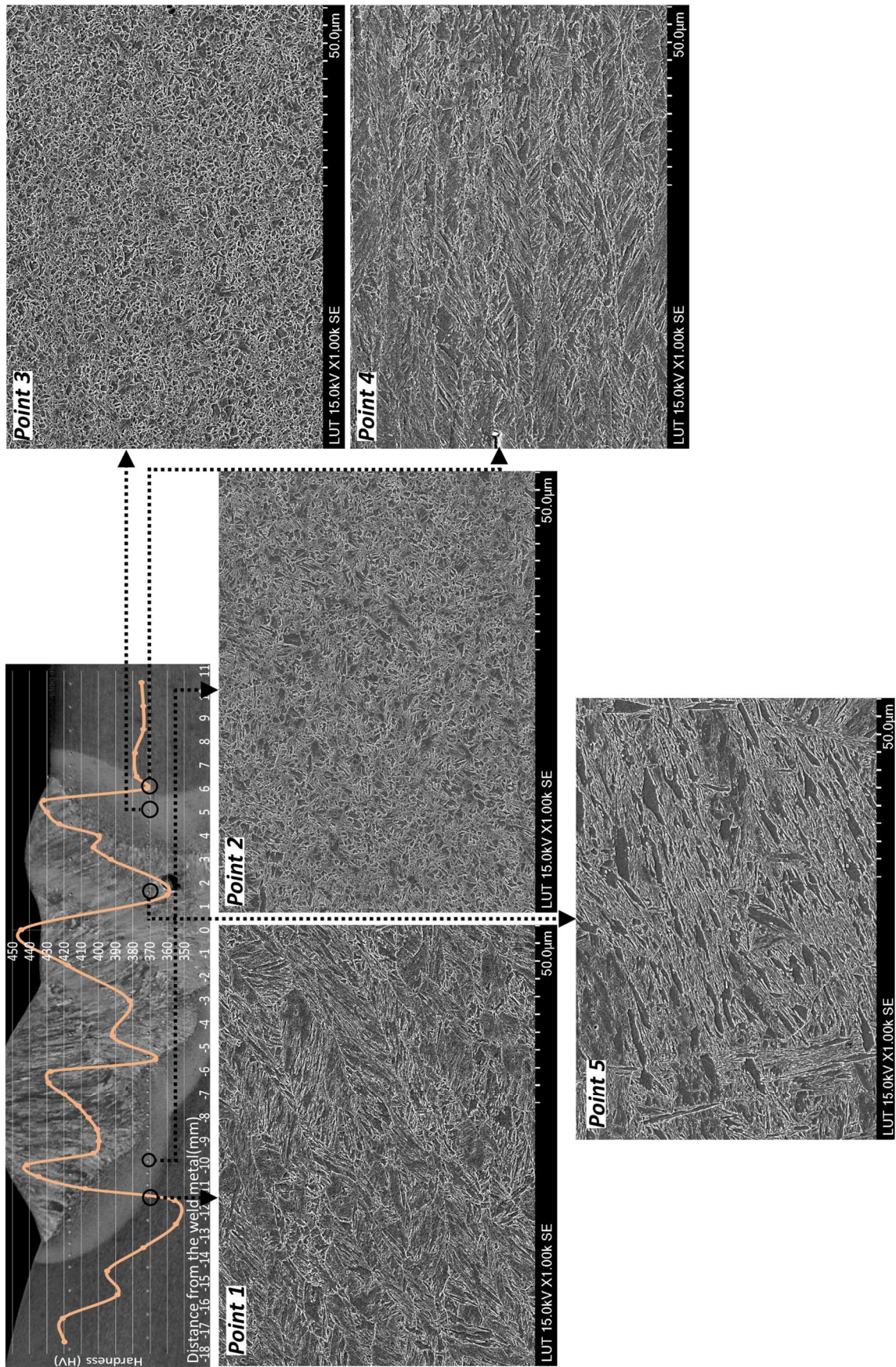
76

Figure 50. Hardness and microstructures of different HAZ sub-zones (S1100; *r/t* = 3.25).

Microstructure of the sub-zones next to the fusion lines are presented in figure 51. As shown in this figure, microstructures of these sub-zone consisted of some sparse laths of bainite surrounded by a coarse martensitic background, which was not much different from the microstructure of the weld metal or the base materials. This microstructural similarity might be a reason for welded S1100 samples showing a more moderate drop of hardness by crossing over their fusion lines (in comparison to welded S700MC).

By comparing different hardness profiles presented in figure 52, it can be concluded that the hardness drops in welded S1100 samples with different pre-strains did not have significant differences. By comparing hardness profiles of figure 52.a and 55.b, it can also be seen that the hardness drops were not significantly different even between the pre-strained and virgin materials. These similar trends can be attributed to the similar microstructures of different regions of welded joints and stability of S1100 microstructure. However, bended base metal with the highest degree of cold forming ($r/t = 3$) had the highest hardness drop.

Microstructures of HAZ sub-zones with the highest and the lowest hardness values are presented in higher magnifications in figures 53 and 54 respectively. According to these figures, points with the peak hardness values had a normalized microstructure with a very fine martensitic texture including sparse islands of bainite. In comparison to other HAZ sub-zones, the higher hardness values of these regions (points 2 and 3 in figure 50) can be attributed to their very fine microstructural features. On the other hand, type of microstructures belonging to the softened zones was not significantly different from their base metals; however, their texture features were slightly coarser. Thus, their decrease in hardness can be attributed to their larger microstructural features.
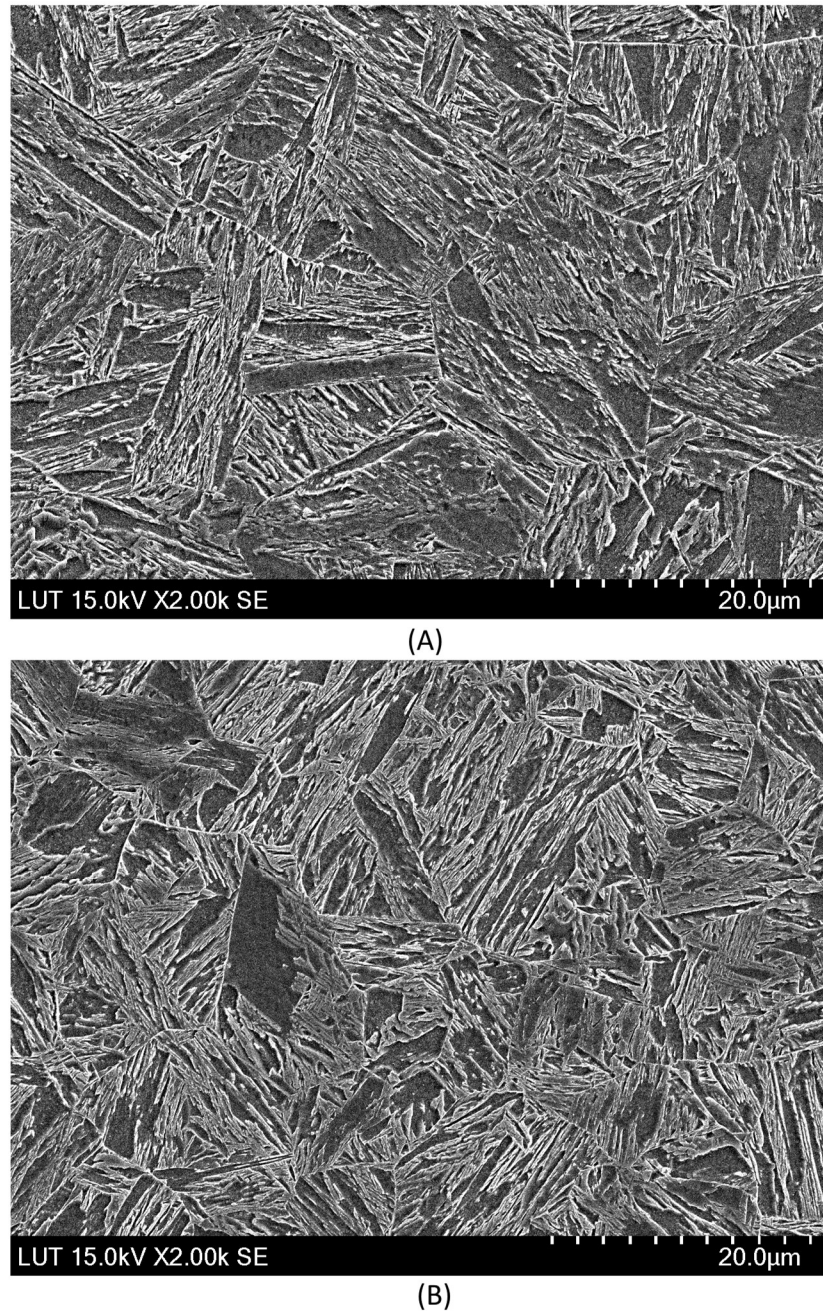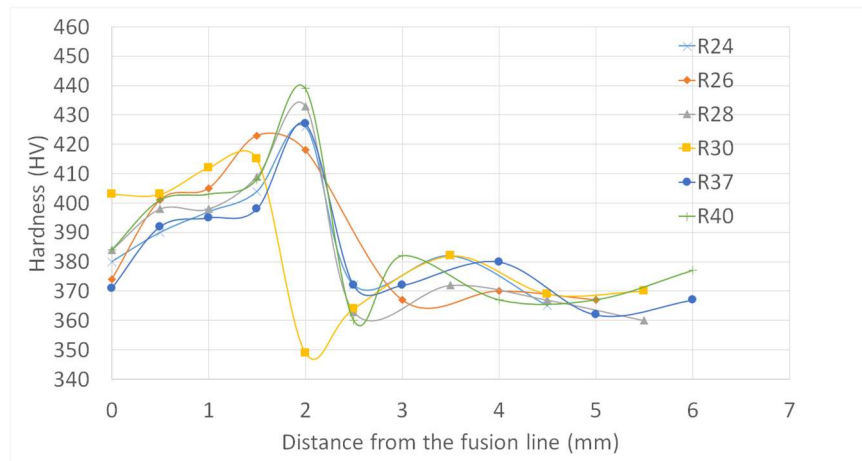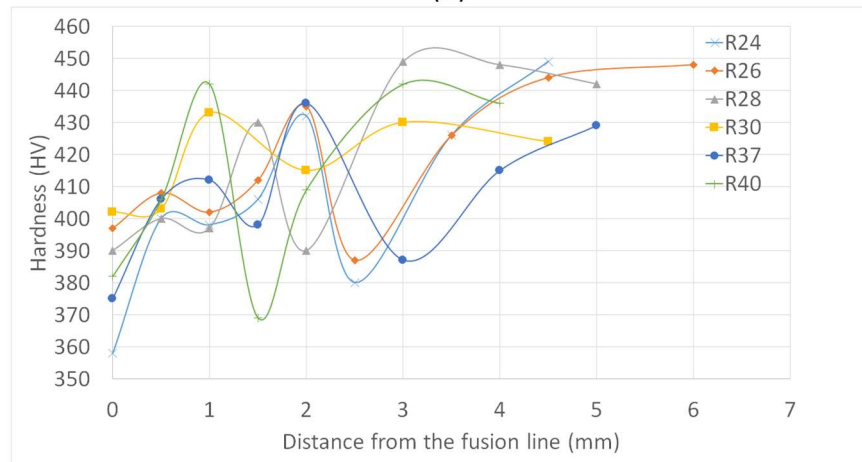
Figure 51. Microstructures of sub-zones next to the fusion lines: (A) on the virgin side; (B) on the bended side. Welded sample is made from S1100 and $r/t = 3.25$.

Figure 52. Hardness profiles of HAZs on different sides of the joints: (A) virgin base metals; (B) cold-formed base metals.
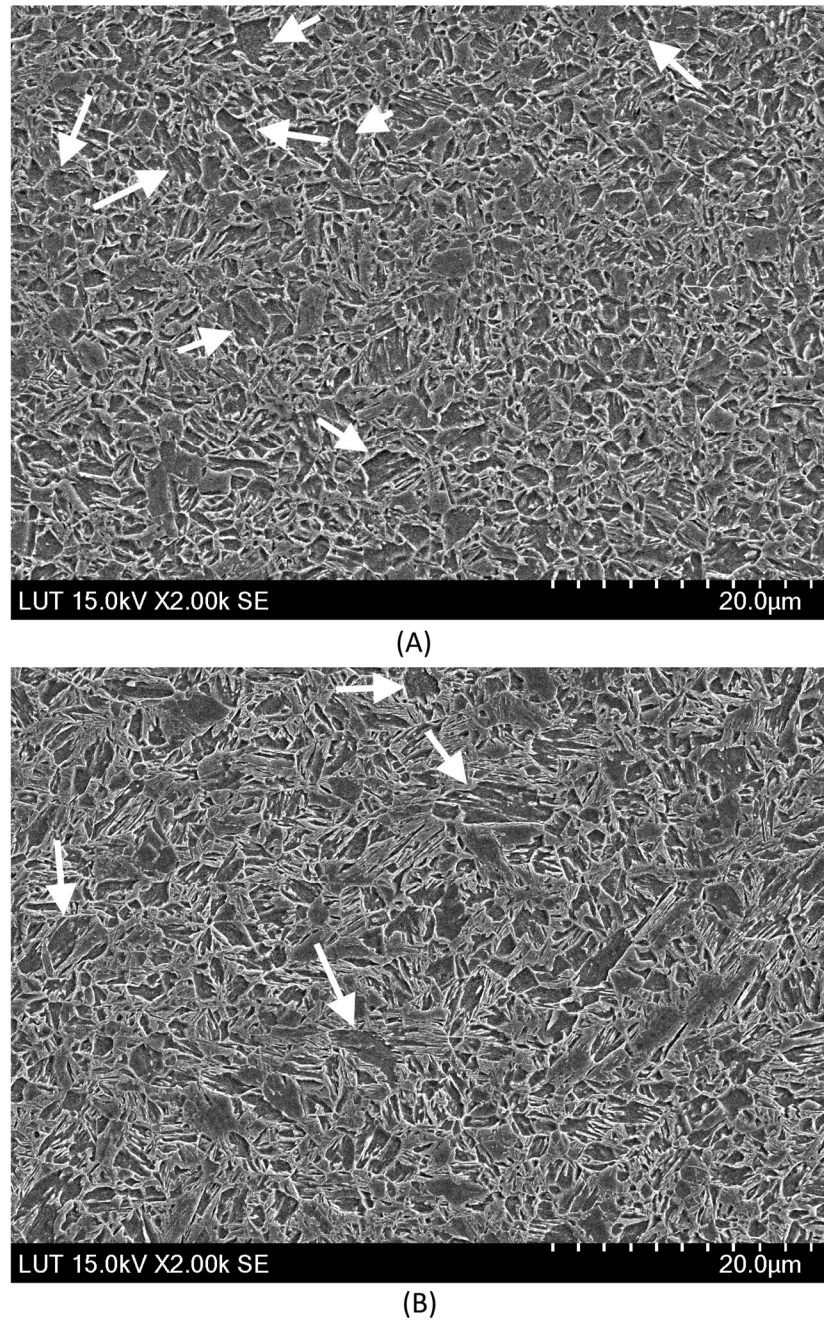
Figure 53. Microstructural features of the HAZ sub-zones with the highest hardness values of: (A) Virgin base metal; (B) cold formed base metal. Bainites are indicated by white arrows, and background phase is martensite (welded S1100 with $r/t = 3.25$).
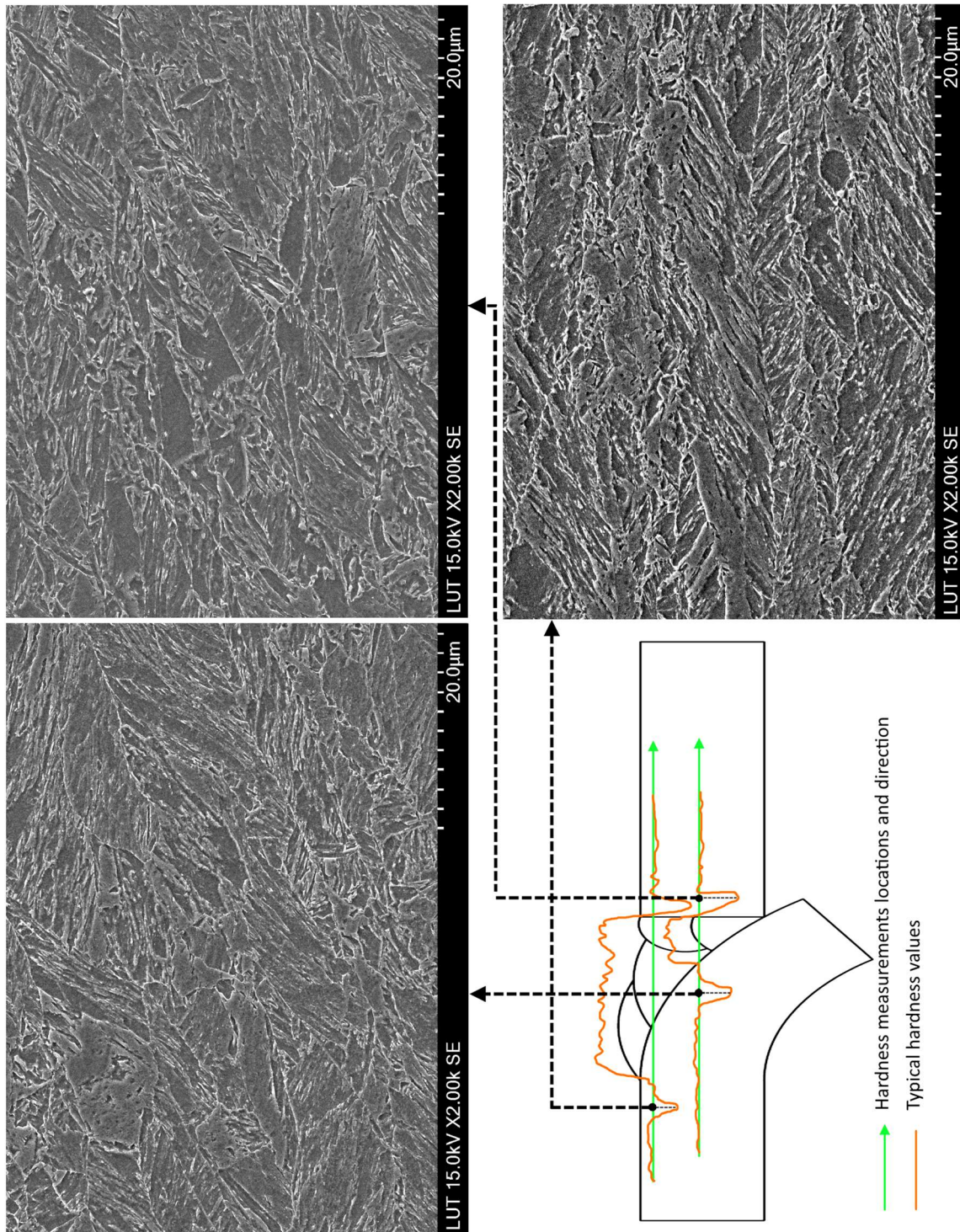
Figure 54. Microstructures of the softened zones (S1100; *r*/*t* = 3.25).

Tempered martensite was another microstructural feature, which was visible in all the sub-regions on both sides of the joints. Due to the scarcity and small sizes of the martensitic islands, their effect on the mechanical properties of the welded joints is neglected in this study. As an example, figure 55 shows some of these blocks near the fusion line of the welded S1100 sample with $r/t = 3.25$. Sparse carbide particles are indicated with white arrows in this figure.
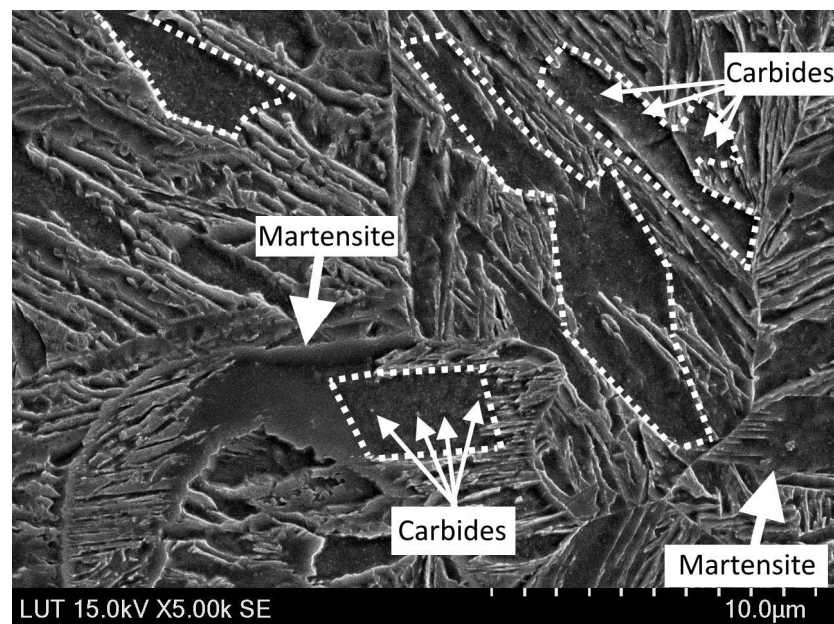

Figure 55. Microstructural features near the fusion line, on the final pass of the welding (welded S1100, $r/t = 3.25$).

4.2.1 Uniaxial tensile tests of S1100 samples

Static mechanical properties of the welded samples are summarized in table 21, and their true stress-strain curves are presented in figure 56. In addition, data obtained from ARAMIS DIC system used to calculate fracture displacements and elongations are shown in figure 57. According to figure 57, all the samples fractured from their virgin base metals (without pre-strains)[5]. Thus, results provided in table 21 and figure 56 represent mechanical properties similar to the base metal in its as received condition. Therefore, Karren's and its subsequent equations from Eurocode 3, EN 1993-1-3, cannot be used to evaluate the results.

---

[5] Macrographs of fractured tensile specimens are also presented in APPENDIX I as evidence of failure at the base metals.

Table 21. Uniaxial tensile properties of the S1100 welded samples.

| r/t on the deformed side of the weld	Yield strength (MPa)	Tensile strength (MPa)	Fracture displacement (mm)	Elongation (%)	Predicted yield strength according to Karren's equation (MPa)	Area of fracture
24	1030	1184	6.4	12.8	-	Virgin base metal
26	1095	1152	6.0	12.0	-	Virgin base metal
28	1115	1195	6.0	12.0	-	Virgin base metal
30	1080	1149	5.7	11.4	-	Virgin base metal
37	1110	1209	5.7	11.4	-	Virgin base metal
40	1090	1192	6.2	12.4	-	Virgin base metal
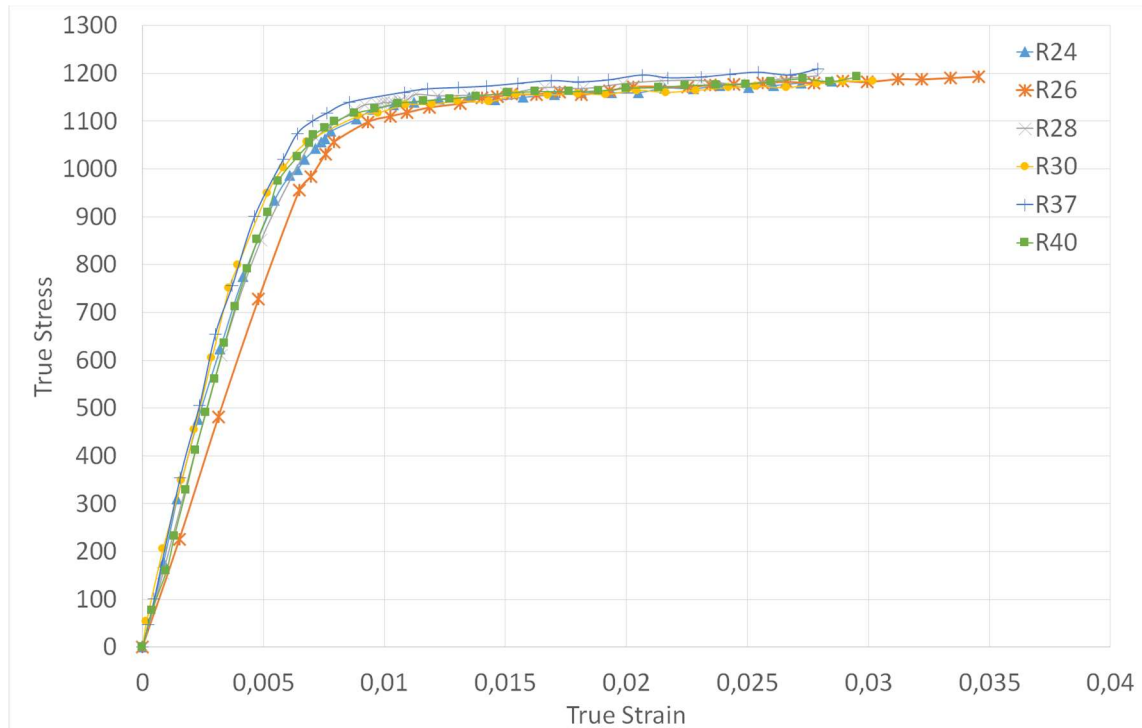
Figure 56. True stress-strain curves of the welded S1100 specimens until their necking point, according to the bending radius of their bended base metal.

Since all specimens failed and fractured from their virgin side, all data presented in table 21 and figure 56 belong to the same material (S1100 in its as received condition). Thus, regardless of the degree of cold-forming on the bended side of each welded sample, these results do not show any significant differences from each other and do not represent static mechanical properties of the bended base metals. However, static mechanical properties of

the bended steels can be accounted as acceptable after welding since none of the bended base metals failed and fractured prior to their corresponding welds and virgin base metals. The fracture from the virgin base metals can be attributed to the proper bending radii (degrees of cold-forming) of the pre-strained sides, since majority of them were bended following the manufacturer's recommendation ($r/t \geq 3$).
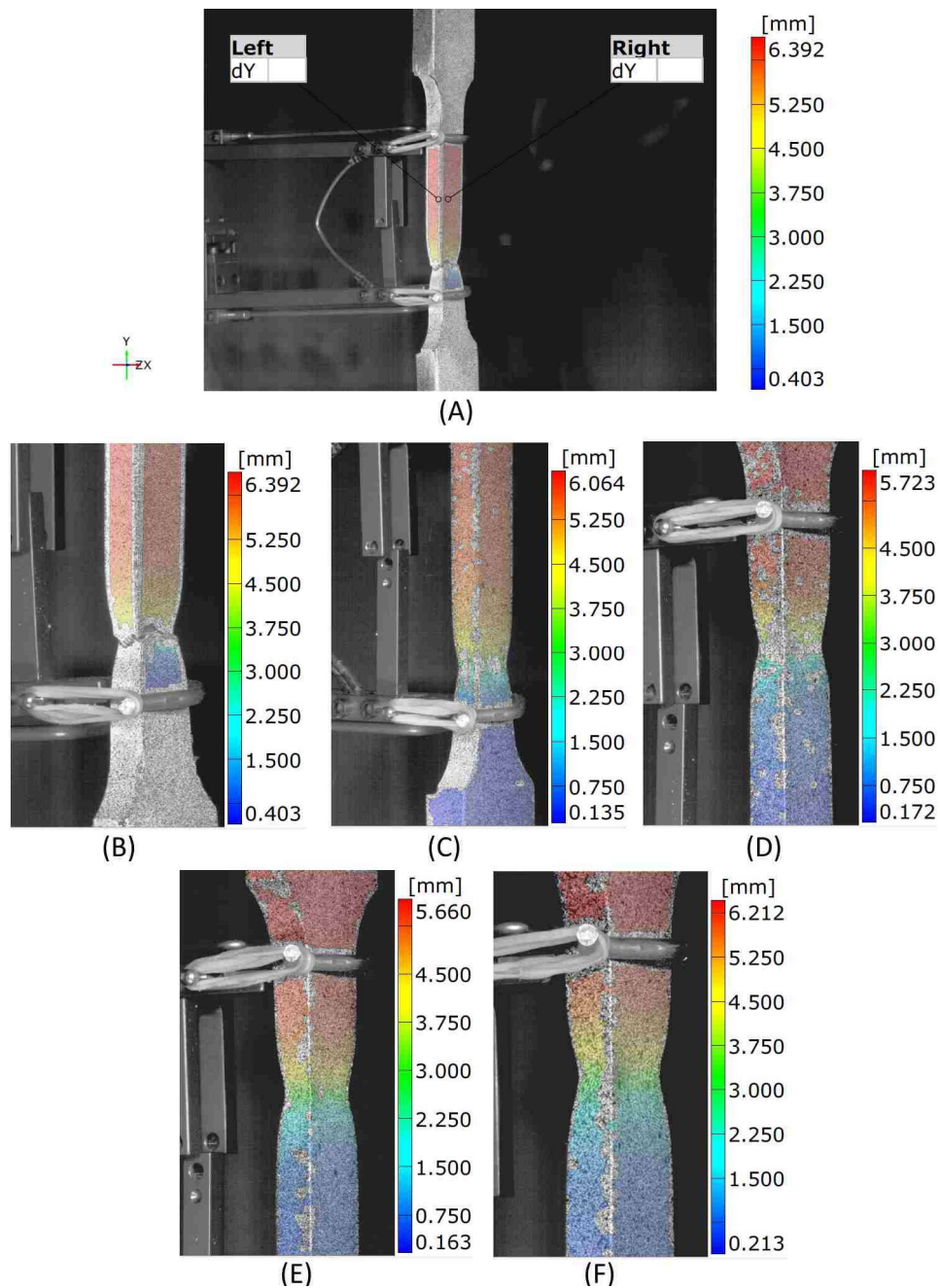

Figure 57. DIC data from the fracture moment, according to the bending radii of the pre-strained sides: (A) overall view of sample with r=24 mm, (B) focused views of $r = 24$ mm, (C) $r = 26$ mm, (D) $r = 30$ mm, (E) $r = 37$ mm, (F) $r = 40$ mm.

4.2.2 Notch toughness of S1100 samples

Notch toughness tests were carried out according to section 3.6, and the results are summarized in figure 58. According to this figure, sample with the highest pre-strain value (lowest *r/t*) had the lowest notch toughness. The value of notch toughness increased by decreasing the degree of cold-forming. Calculated by conversion factor (*s/S* = 0.5), samples consisting of bended base metals with *r/t* = 3, 3.25, and 3.5 (*r* = 24 mm, 26 mm, and 28 mm) seemed to have notch toughness values lower than acceptable criteria for S1100 (27J at -40˚C). Fractured areas of broken samples are presented in figure 59. As can be seen in this picture, bended base metal with the highest level of pre-strain (lowest *r/t*) has the smallest proportion of shear fracture surface.
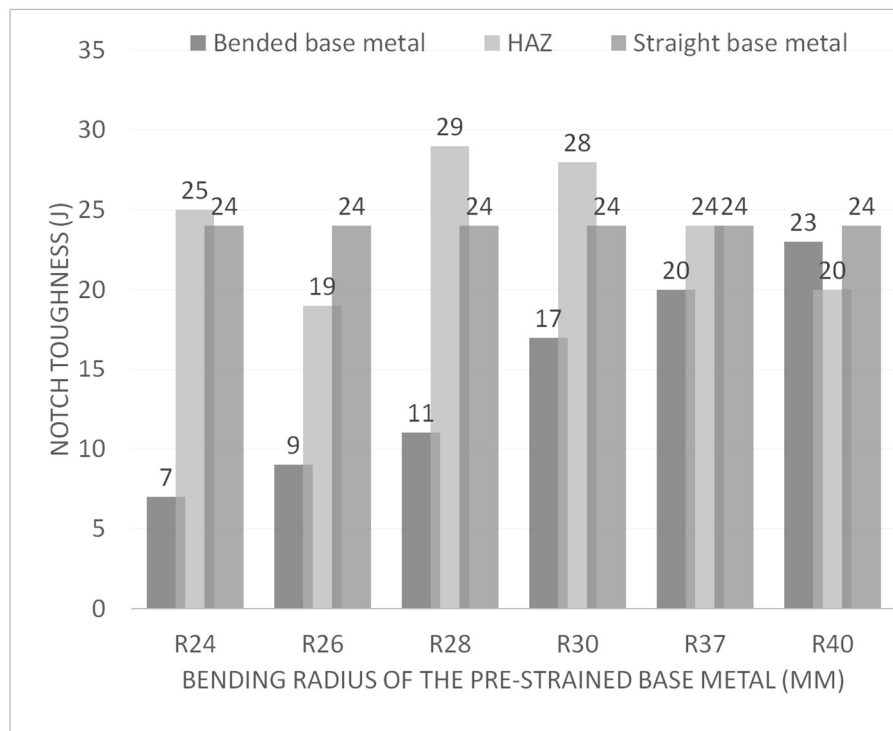

Figure 58. Notch toughness of different areas for the welded joints made of S1100.
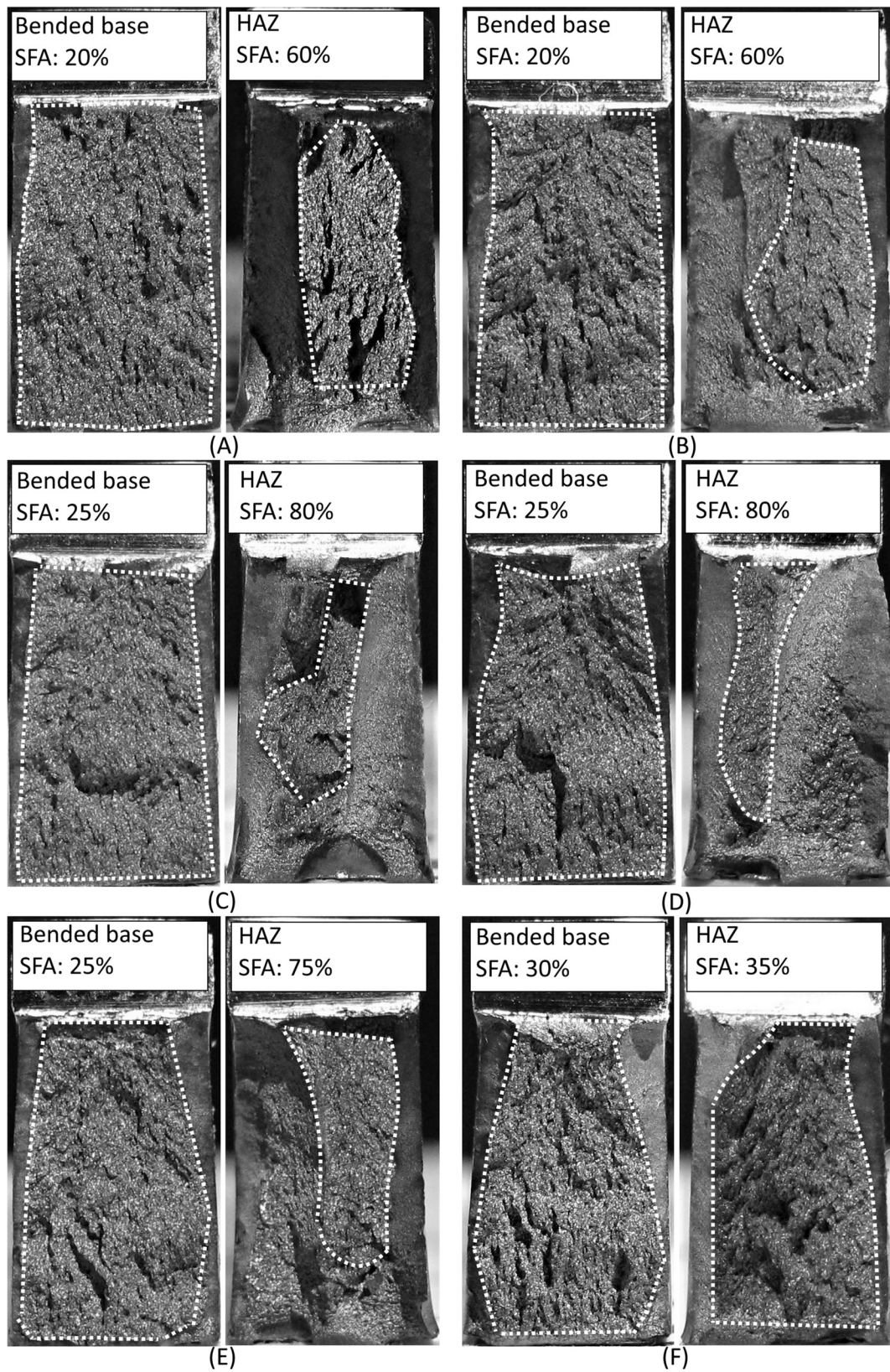
Figure 59. Fracture surfaces and SFAs for the bended sides of the joints: (A) $r = 20$ mm, (B) $r = 24$ mm, (C) $r = 28$ mm, (D) $r = 30$ mm, (E) $r = 37$ mm, (F) $r = 40$ mm. Brittle fracture areas are indicated by white dashed lines.

4.3   Evaluation of weldability

In this study, four criteria were considered to evaluate the weldability of cold-formed S700MC and S1100, which were their microstructures, hardness profiles, tensile properties, and fracture energies. Regarding the microstructure, S1100 did not have any disadvantageous phases along its HAZs and base metals after the welding trials, except for some small amounts of tempered martensite. However, sizes and distributions of tempered martensite islands were so small that this phase did not show any significant negative effect on the mechanical properties of the welded joints. For S700MC, although some undesirable phases, such as upper bainite and tempered martensite, were scattered from the fusion lines into their HAZs, they seemed to be not defective enough to alter their mechanical properties. Some studies attribute the neutrality of these phases on mechanical properties of the welded joints to the low carbon content of (U)HSSs (Górka & Stano 2018, p. 8).

Regarding the hardness values, SSAB (2016b, p. 34) considered hardness drops higher than 10% of the unaffected parent metal as soft zones. Table 22 summarizes the minimum hardness values of each heat affected zone and its parent material. The percentage of hardness drops are also calculated in this table to evaluate their severity. According to this table, in 700MC samples, majority of the reheated areas (middle sections) suffered from soft zone. In addition, soft zones were more frequent in pre-strained base metals. Regarding S1100, all pre-strained metals suffered from soft zones after welding, while none of the virgin materials experienced severe softening.

In conclusion, softening was more common in the bended materials. This result can be attributed to the interactions between the prior cold work and welding heat. Treatments which are consequences of welding heat, such as recovery, ease the effects of prior cold-forming and result in more sever and frequent softening in the pre-strained base metals. However, just existence of soft zones cannot be considered as a sign of low weldability. In other words, location of fracture in a welded joint is also a determining factor. Since none of the specimens fractured from their HAZs, soft areas did not have a significant effect on the mechanical properties of the welded joints. According to some studies, narrowness of soft zones prevents them from having a negative effect on the joint properties (Farrokhi, Siltanen & Salminen. 2015, pp. 1-10).

Table 22. Hardness evaluations of the welded joints.

Material	Bending radius (mm)	Area	Minimum hardness (HV)	Hardness of the parent metal (HV)	Hardness drop*
S700MC	5	Bended HAZ, upper section	268	295	9%
S700MC	5	Bended HAZ, middle section	245	284	14%
S700MC	5	Bended HAZ, lower section	263	308	15%
S700MC	5	Virgin HAZ, upper section	259	279	8%
S700MC	5	Virgin HAZ, middle section	228	279	18%
S700MC	5	Virgin HAZ, lower section	249	287	14%
S700MC	10	Bended HAZ, upper section	261	300	13%
S700MC	10	Bended HAZ, middle section	254	285	10%
S700MC	10	Bended HAZ, lower section	261	292	10%
S700MC	10	Virgin HAZ, upper section	257	280	9%
S700MC	10	Virgin HAZ, middle section	229	279	8%
S700MC	10	Virgin HAZ, lower section	254	283	10%
S700MC	15	Bended HAZ, upper section	257	286	8%
S700MC	15	Bended HAZ, middle section	239	284	15%
S700MC	15	Bended HAZ, lower section	252	285	11%
S700MC	15	Virgin HAZ, upper section	262	276	5%
S700MC	15	Virgin HAZ, middle section	204	279	16%
S700MC	15	Virgin HAZ, lower section	263	284	7%
S700MC	20	Bended HAZ, upper section	274	317	14%
S700MC	20	Bended HAZ, middle section	239	292	18%
S700MC	20	Bended HAZ, lower section	267	287	7%
S700MC	20	Virgin HAZ, upper section	255	277	7%
S700MC	20	Virgin HAZ, middle section	221	277	20%
S700MC	20	Virgin HAZ, lower section	252	279	9%
S1100	24	Bended HAZ, upper section	358	448	18%
S1100	24	Bended HAZ, middle section	355	403	12%
S1100	24	Bended HAZ, lower section	374	417	11%
S1100	24	Virgin HAZ, upper section	379	382	10%
S1100	24	Virgin HAZ, middle section	357	384	8%
S1100	24	Virgin HAZ, lower section	362	372	3%
S1100	26	Bended HAZ, upper section	387	448	14%
S1100	26	Bended HAZ, middle section	356	420	15%
S1100	26	Bended HAZ, lower section	358	427	16%
S1100	26	Virgin HAZ, upper section	367	370	2%
S1100	26	Virgin HAZ, middle section	372	374	2%
S1100	26	Virgin HAZ, lower section	369	375	2%
S1100	28	Bended HAZ, upper section	390	442	11%
S1100	28	Bended HAZ, middle section	351	415	15%
S1100	28	Bended HAZ, lower section	365	430	15%
S1100	28	Virgin HAZ, upper section	363	367	7%
S1100	28	Virgin HAZ, middle section	358	367	3%
S1100	28	Virgin HAZ, lower section	362	369	2%
S1100	30	Bended HAZ, upper section	402	424	5%
S1100	30	Bended HAZ, middle section	353	409	14%
S1100	30	Bended HAZ, lower section	351	415	16%
S1100	30	Virgin HAZ, upper section	349	370	5%
S1100	30	Virgin HAZ, middle section	342	367	6%
S1100	30	Virgin HAZ, lower section	346	369	6%
S1100	37	Bended HAZ, upper section	375	429	13%
S1100	37	Bended HAZ, middle section	351	391	11%
S1100	37	Bended HAZ, lower section	330	398	11%
S1100	37	Virgin HAZ, upper section	372	380	2%
S1100	37	Virgin HAZ, middle section	351	367	4%
S1100	37	Virgin HAZ, lower section	360	372	3%
S1100	40	Bended HAZ, upper section	369	436	15%
S1100	40	Bended HAZ, middle section	355	415	15%
S1100	40	Bended HAZ, lower section	365	432	15%
S1100	40	Virgin HAZ, upper section	360	377	5%
S1100	40	Virgin HAZ, middle section	387	395	2%
S1100	40	Virgin HAZ, lower section	369	385	4%
* Red: higher than 10%; Green: Lower than 10%					

Results of the uniaxial tensile tests showed the negative effect of excessive pre-strain on weldability. According to the results provided in sections 4.1.1 and 4.2.1, samples with bending radii smaller than the recommended values fractured from their pre-strained base metals. Thus, it can be concluded that S700MC and S1100 had acceptable weldability as far as they were cold-formed in accordance with their manufacturer's recommended specifications (table 7). results of the Charpy impact tests also lead to a similar conclusion. Bended samples with maximum pre-strains (r/t= 0.5 for S700MC; r/t= 3, 3.25, and 3.5 for S1100) estimated to have notch toughness values lower than acceptable criteria by the manufacturer (27 J at -40 ˚C). Thus, welding their cold-formed sections with these r/t ratios is not recommended, especially for cryogenic applications

5   CONCLUSION

This study investigated microstructures and mechanical properties of cold-formed S700MC and S1100 after welding to evaluate their weldability. According to the test results, following conclusion can be made:

1- Visual inspection of welds showed no defects. However, some porosities were visible between the second and the third welding passes on the bended base materials. These porosities might be due to improper torch angle.

2- Both S700MC and S1100 had bainitic-martensitic microstructures in their as-received and cold-formed conditions.

3- All welded samples showed patterns of hardness fluctuations typical for (U)HSSs, including soft zones and sub-regions with the highest hardness values near the fusion lines.

4- Hardness values were higher on the cold-formed sides of the welded joints of S700MC.

5- For S1100, regardless of its degree of cold-forming, hardness values were similar for pre-strained and virgin base metals after its welding.

6- According to tensile tests, materials with excessive pre-strains fractured prematurely. In addition, their notch toughness was lower than acceptable values.

In conclusion, pre-strained S700MC and S1100 showed acceptable weldability and satisfactory mechanical properties after welding. However, degree of cold-forming has a determining role in their post welding behaviour. Excessive deformation and pre-strains result in premature fractures in the cold-formed materials. Regarding this matter, following the deformation limits provided by the manufacturer and standards are highly recommended. Furthermore, acceptance criteria provided by EN 1993-1-8 seems to be quite effective in welding cold-formed S700MC and S1100.

5.1   Further study

Although this study investigated weldability of cold-formed S700MC and S1100, weldability of some other (U)HSSs (such as S900QC or UHSSs with strength levels higher than 1100MPa) still requires more inquiry. In addition, although welding criteria provided by Eurocode 3 for cold-formed steels seems to be applicable for S700MC and S1100, applicability of some of the equations seems to need more investigation. Possibly, some new equations need to be developed to estimate theoretical strengths of steel structures containing welded cold-formed (U)HSSs.

To have a better understanding and more accurate estimation on weldability of (U)HSSs, it is a better approach to devise a research plan to distinguish effects of cold-forming and welding heat from each other. To do so, a welding process with more control over its heat input, such as GTAW, and bead on plate technique are recommended for future studies. As an example, a welding set up is presented in figure 60. By this set up, it is possible to use different heat inputs on a constant bending radius to investigate effects of welding heat. Then it is possible to use a constant welding heat input on different bending radii to study effects of cold-forming.
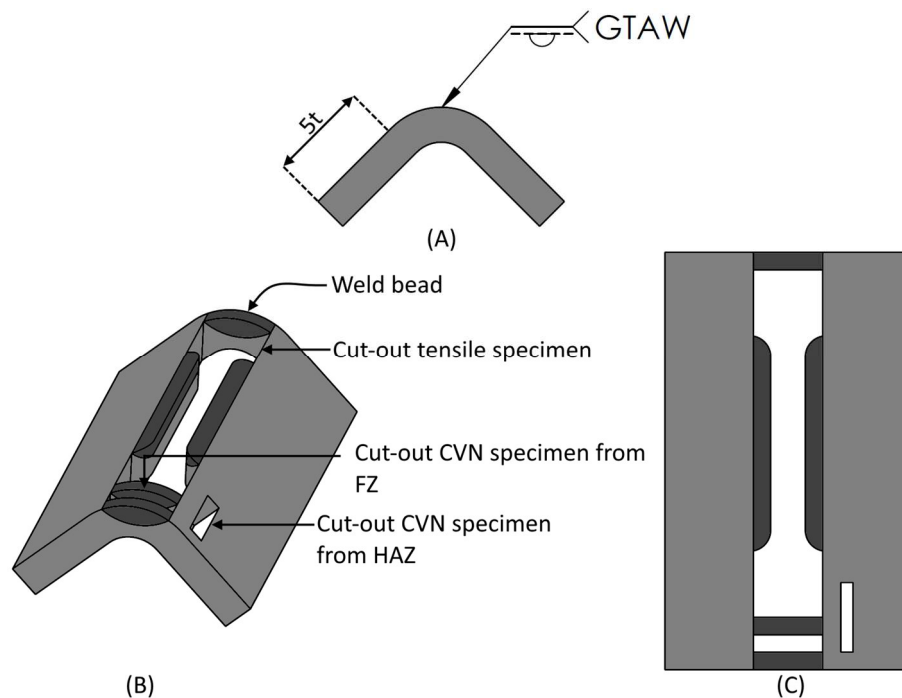

Figure 60. Suggested welding set-up and specimens to investigate effects of cold-forming and welding heat individually.

LIST OF REFERENCES

Abson, D. J. & Rothwell, J. S. 2013. Review of type IV cracking of weldments in 9–12%Cr creep strength enhanced ferritic steels. International Materials Reviews, 58(8), Pp. 437-473.

Aksel, H. & Eren, Ö. 2015. A discussion on advantages of steel structures in the context of sustainable construction. International Journal of Contemporary Architecture, 2: 3. Pp. 47-53.

Androić, B., Dujmović, D. & Pišković, J. 2014. Application of cold formed hollow steel sections. Građevinar, 66: 10. Pp. 929-935.

Arreola-Herrera, R., Cruz-Ramírez, A., Suárez-Rosales, M. Á. & Sánchez-Álvarado, R. G. 2014. The effect of cold forming on structure and properties of 32 CDV 13 steel by radial forging process. Materials Research. 17: 2. Pp. 445-450.

Ashraf, M., Gardner, L. & Nethercot, D. A. 2005. Strength enhancement of the corner regions of stainless steel cross-sections. Journal of Constructional Steel Research. 61: 1. Pp. 37-52.

Aydin, H. 2014. Relationship between a bainitic structure and the hardness in the weld zone of the friction-stir welded X80 API-grade pipe-line steel. Materials and Technology. 45. Pp. 15-22.

AZOM, 2018. In: AZO Materials [web database]. AZOM. [referred 19.4.2018]. Available: https://www.azom.com/. Limited service is free of charge

Bhadeshia, H. K. & Christian, J. W. 2015. [Chapter 1:] Introduction. In: Bhadeshia, H. K. & Christian, J. W. Bainite in steels: Theory and Practice. 3rd ed. Leeds, UK: Maney Publishing.

Brockenbrough, R. L. & Merritt, F. S. 1999. Structural steel shapes and plates. In: Brockenbrough, R. L. Structural steel designer's handbook. New York: McGraw-Hill, Pp. 1-40.

Cosham, A., Hopkins, P. & Palmer, A. 2004. An experimental and numerical study of the effect of pre-strain on the fracture toughness of line pipe steel. International Pipeline Conference, Alberta, USA: American Society of Mechanical Engineers.

Crawford, R. H. 2011. Global environmental issues and the built environment. In: LIfe cycle assessment in the built environment. New York: Spon Presss, Pp. 1-24.

Diegel, O. 2002. The fine-art of sheet metal bending. [web document]. Published 2002, [Referred 15.3.2018]. Available: http://www.micromachineshop.com/Sheet%20Metal%20Bending.pdf

EN 1011-2. 2001. Recommendation for welding of metallic materials. Part 2: arc welding of ferritic steels. EUROPEAN COMMITTEE FOR STANDARDIZATION. 59 p.

EN 1993-1-8. 2005. Eurocode 3: Design of steel structures - Part 1-8: Design of joints. EUROPEAN COMMITTEE FOR STANDARDIZATION. 138 p.

EN 1993-1-10. 2005. Eurocode 3: Design of steel structures – Part 1-10: Material toughness and through-thickness properties. EUROPEAN COMMITTEE FOR STANDARDIZATION. 20 p.

EN 1993-1-12. 2005. Eurocode 3: Design of steel structures - Part 1-12: Additional rules for the extension of EN 1993 up to steel grades S 700. EUROPEAN COMMITTEE FOR STANDARDIZATION. 12 p.

Evans, P. 2010. *22 possible causes of weld metal porosity.* [web document]. Published 2010, [Referred 23.4.2018]. Available: https://www.thefabricator.com/article/arcwelding/22-possible-causes-of-weld-metal-porosity

Farrokhi, F., Siltanen, J. & Salminen, A. 2015. Fiber laser welding of direct-quenched ultrahigh strength steels: evaluation of hardness, tensile strength, and toughness properties at subzero temperatures. Journal of Manufacturing Science and Engineering, 137:6, Pp. 1-10.

Garašić, I., Ćorić, A., Kožuh, Z. & Samardžić, I. 2010. Occurrence of cold cracks in welding of high-strength S960 QL steel. Tehnički vjesnik, 17:3, Pp. 327-335.

Gerhards, B., Reisgen, U. & Olschok, S. 2016. Laser welding of ultrahigh strength steels at subzero temperatures. Physics Procedia, 83, Pp. 352-361.

Goli-Oglu, E. A., Éfron, L. I. & Morozov, Y. D. 2013. Effect of Deformation Regime in Main Stages of Controlled Rolling on Pipe Steel Microstructure. Metal Science and Heat Treatment, 55:5-6, Pp. 294-297.

Górka, J. 2015. Study of structural changes in S700MC steel thermomechanically treated under the influence of simulated welding thermal cycles. Indian Journal of Engineering & Materials Science, 22, Pp. 497-502.

Górka, J. 2016. Microstructure and properties of the high-temperature (HAZ) of thermo-mechanically treated S700MC high-yield-strength steel. Materiali in tehnologije, 50: 4, Pp. 617-621.

Górka, J. & Stano, S. 2018. Microstructure and Properties of Hybrid Laser Arc Welded Joints (Laser Beam-MAG) in Thermo-Mechanical Control Processed S700MC Steel. Metals, 8: 2, Pp. 1-15.

Guo, W., Liu, Q., Francis, J, A., Crowther, D., Thompson, A., Liu, Z., Li, L. 2015. Comparison of laser welds in thick section S700 high-strength steel manufactured in flat (1G) and horizontal (2G) positions. CIRP Annals, 64: 1, Pp. 197-200.

Guo, W., Li, L., Crowther, D., Dong, S., Francis, J., A., Thompson, A. 2016. Laser welding of high strength steels (S960 and S700) with medium thickness. Journal of Laser Applications, 28: 2, Pp. 1-12.

Guo, W., Li, L., Dong, S., Crowther, D., Thompson, A. 2017. Comparison of microstructure and mechanical properties of ultra-narrow gap laser and gas-metal-arc welded S960 high strength steel. Optics and Lasers in Engineering, 91, Pp. 1-15.

Hamedon, Z., Mori, K. & Abe, Y. 2014. Hemming for joining high strength steel sheets. Procedia Engineering, 81, Pp. 2074-2079.

Hubmer, G. et al., 2017. Roll-formed hf welded tubes and sections made from ultra-high strength martensitic steels with yield strength 960 MPA-and Beyong. [web document]. Published 2017,[Referred 25.4.2018]. Available: http://www.voestalpine.com/division_s tahl/content/download/52622/655434/file/VAST-W17008A%20White%20Paper%20Roll-formed.pdf

Javidan, F., Heidarpour, A., Zhao, X. L. & Hutchinson, C. R. M. J. 2016. Effect of weld on the mechanical properties of high strength and ultra-high strength steel tubes in fabricated hybrid sections. Engineering Structures, 118, Pp. 16-27.

Jayanti, S. 2018. Bainite: Morphology and Characteristics. [web document]. Published 2018, [Referred 29.4.2018]. Available: http://www.engineeringnotes.com/metallurgy/bainite/b ainite-morphology-and-characteristics-steel-metallurgy/26960

Jiang, Q. M., Zhang, X. Q. & Chen, L. Q. 2016. Weldability of 1000 MPa grade ultra-low carbon bainitic steel. Journal of Iron and Steel Research, 23: 7, Pp. 705-710.

Kah, P., Pirinen, M., Suoranta, R. & Martikainen, J. 2014. Welding of ultra high strength steels. Advanced Materials Research, 849, Pp. 357-365.

Keeler, S., Kimchi, M. & Mooney, P. 2017. Forming and Manufacturing. In: Advanced high-strength steels application guidelines: Version 6. s.l., World Auto Steel, Pp. 80-91.

Klein, M., Rauch, R., Spindler, H. & Stiaszny, P. 2012. Ultra High Strength Steels Produced by Thermomechanical Hot Rolling–Advanced Properties and Applications. BHM Berg-und Hüttenmännische Monatshefte, 157: 3, Pp. 108-112.

Koo, J. Y., Luton, M. J., Bangaru, N. V. & Petkovic, R. A. 2003. Metallurgical Design of Ultra-High Strength Steels for Gas Pipelines. International Offshore and Polar Engineering Conference, Honolulu, USA, International Society of Offshore and Polar Engineers, Pp. 10-18.

Kou, S., 2003. Gas-Metal Arc Welding. In: Welding metallurgy. New Jersey, USA: JOHN WILEY & SONS, Pp. 19-22.

Kundu, A. & Chakraborti, P. C. 2014. Effect of Austenite Grain Size and Composition on Matrix Microstructure and Properties of Steel. Procedia Materials Science, 5, Pp. 1141-1147.

Kurc-Lisiecka, A. 2017. Impact toughness of laser-welded butt joints of the new steel grade strenx 1100MC. Materiali in Tehnologije, 41: 4, Pp. 643-649.

Kurc-Lisiecka, A., Piwnik, J. & Lisiecki, A. 2017. Laser Welding of New Grade of Advanced High Strength Steel STRENX 1100 MC. Archives of Metallurgy and Materials, 62: 3, Pp. 1651-1657.

Lee, J. H. et al., 2014. Laser, tungsten inert gas, and metal active gas welding of DP780 steel: comparison of hardness, tensile properties and fatigue resistance. Materials and Design, Volume 64, Pp. 559-565.

Lucon, E., Mc Cowan, C. N. & Santoyo, R. L., 2016. Overview of NIST Activities on Subsize and Miniaturized Charpy Specimens: Correlations With Full-Size Specimens and Verification Specimens for Small-Scale Pendulum Machines. Journal of Pressure Vessel Technology, 138: 3, Pp. 1-42.

Macdonald, M., Taylor, G. T. & Rhodes, J. 1997. The effect of cold forming on the yield strength of thin gauge steel—hardness test approach. Thin-walled structures, 29: 1-4, Pp. 243-256.

Maity, S. K. & Kawalla, R. 2011. Ultrahigh strength steel: Development of mechanical properties through controlled cooling. In: Vikhrenko, V., S. Heat transfer engineering applications. Rijeka, Croatia: Intech, Pp. 309-337.

Mandal, S., Tewary, N., K., Ghosh, S., K., Chakrabarti, D., Chatterjee, S. 2016. Thermo-mechanically controlled processed ultrahigh strength steel: Microstructure, texture and mechanical properties. Materials Science and Engineering: A, 663, Pp. 126-140.

Matsuoka, S., Hasegawa, K. & Tanaka, Y. 2007. Newly-developed ultra-high tensile strength steels with excellent formability and weldability, JFE Technology Report, 10, Pp. 13-18.

Mojarad, S. 2017. What are bend allowance, bend deduction and k-factor. [web document]. Published 2017, [Referred 15.3.2018]. Available: http://www.javelintech.com/blog/201 7/06/sheet-metal-design-terminology/

Navarro-López, A., Hidalgo, J., Sietsma, J. & Santofimia, M. J. 2017. Characterization of bainitic/martensitic structures formed in isothermal treatments below the Ms temperature. Materials Characterization, 128, Pp. 248-256.

Němeček, S., Mužík, T. & Míšek, M. 2012. Differences between laser and arc welding of HSS steels. Physics Procedia, 36, Pp. 67-74.

Nesic, S., Krupp, U. & Michels, W. 2014. Monotonic and cyclic loading behavior of closed-cell aluminum foams and sandwich structures. Procedia Materials Science, 4, Pp. 269-273.

Nicholas, J. M. & Abson, D. J. 2008. The prediction of maximum HAZ hardness in various regions of multiple pass welds. Proceedings of the 17th International Conference Computer Technology in Welding and Engineering, Cranfield: TWI. Pp. 18-19.

Ochodek, V. & Boxan, P. 2014. Weldability of carbon steel processed by multiple plastic deformation. Archives of Materials Science and Engineering, 69: 2, Pp. 88-93.

Porter, A., 2015. Weldable high-strength steels: Challenges and engineering applications. Helsinki, Finland: IIW, 4, Pp. 26-28.

Puthli, R. & Packer, J. A. 2013. Structural design using cold-formed hollow sections. Steel Construction, 6: 2, Pp. 150-157.

Rauch, R., Kapl, S., Posch, G. & Radlmayr, K. 2012. High strength low alloy steel weldments with accommodated qualities to the base metal. BHM Berg-und Hüttenmännische Monatshefte, 157:3, Pp. 102-107.

Ritakallio, P. & Björk, T. 2014. Low-temperature ductility and structural behaviour of cold-formed hollow section structures–progress during the past two decades. Steel construction, 7:2, Pp. 107-115.

Schuler, 1998. Bending. In: Metal Forming Handbook. Berlin, Germany: Springer-Verlag, Pp. 366-373.

Shome, M. & Tumuluru, M. 2015. Introduction to welding and joining of advanced high-strength steels (AHSS). In: Shome, M. & Tumuluru, M. Welding and Joining of advanced high strength steels (AHSS). Cambridge: Woodhead publishing, Pp. 1-8.

Siltanen, J., Tihinen, S. & Kömi, J. 2015. Laser and laser gas-metal-arc hybrid welding of 960 MPa direct-quenched structural steel in a butt joint configuration. Journal of Laser Applications, 27: S2, Pp. 1-9.

Sloof, P. A. & Schuster, R. M. 2000. Yield Strength Increase of Cold Formed Sections Due to Cold Work of Forming. 15th International Specialty Conference, Rolla, USA: Missouri University of Science and Technology.

Spindler, H., Klein, M., Rauch, R., Pichler, A., Stiaszny, P. 2005. High strength and ultra high strength hot rolled steel grades-Products for advanced applications. Rome, Italy: Associazione Italian di Metallurgica.

SSAB, 2015a. Welding Strenx and Hardox. [web document]. Published 2015, [Referred 15.3.2018]. Available: http://www.winfa.sk/wp-content/uploads/2017/03/zvar2016-9-8.pdf

SSAB, 2015b. Welding of Strenx: advanced high strerngth steels. [web document]. Published 2015, [Referred_15.3.2018]. Available at: http://www.aemach.com/strenx/pd f/299-en-Welding-of-Strenx-Advanced-High-Strength-Steels.pdf

SSAB, 2016a. The beauty of Strenx: Stronger and Lighter. [web document]. Published 2016, [Referred 12.3.2018]. Available: http://www.italautocar.com/images/informazioni_tecnic he/pdf/en/materials/high_strength_steel/strenx_en.pdf

SSAB, 2016b. Welding Handbook: A Guide to Better Welding of Hardox and Weldox. 1 ed. Oxelösund, Sweden: SSAB. 133 p.

SSAB, 2017. Welding of Strenx. [web document] Published 2017, [Referred 15.3.2018]. Available: https://ssabwebsitecdn.azureedge.net//media/files/en/strenx/ssabstrenxwelding-brochure-2017.pdf

Tasalloti, H., Kah, P. & Martikainen, J. 2017. Effect of heat input on dissimilar welds of ultra high strength steel and duplex stainless steel: Microstructural and compositional analysis. Materials Characterization, 123, Pp. 29-41.

Yang, H. S. & Bhadeshia, H. K. D. H. 2009. Austenite Grain Size and the Martensite-Start Temperature. Scripta Materialia, 60, Pp. 493-495.

Yun, P., Peng, X., N., Zhang, X., M., Tian, Z., L., Tao, W., A. 2014. Microstructure and mechanical properties of GMAW weld metal of 890 MPa class steel. Journal of Iron and Steel Research, 51: 5, Pp. 539-544.
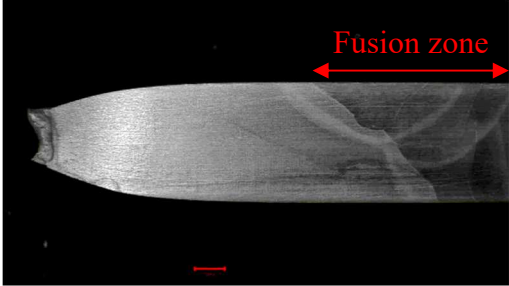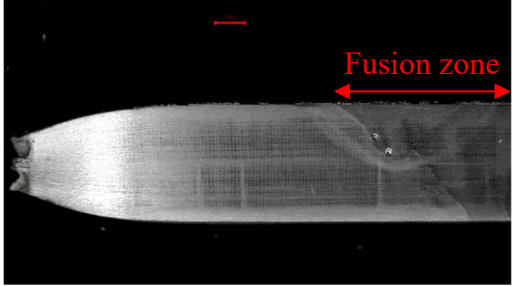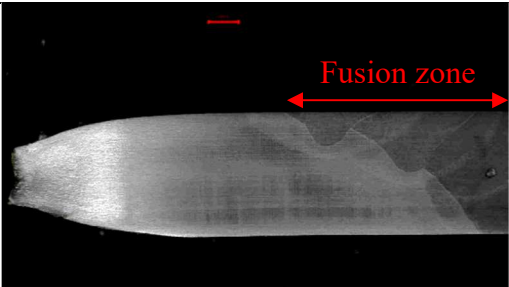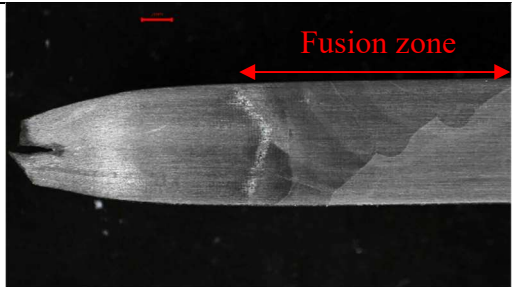
Yurioka, N. 2004. Comparison of preheat predictive methods. Welding in the World, 48: 1-2, Pp. 21-27.

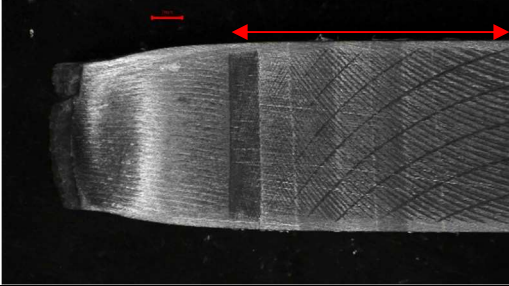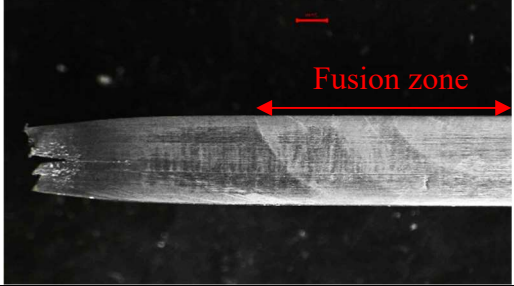Yu, W. W., 2000. [Chapter 1:] Introduction In: Cold-formed steel design. New York, USA: John Wiley & Sons, Pp. 1-30.
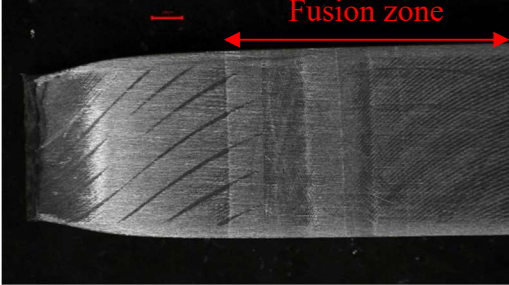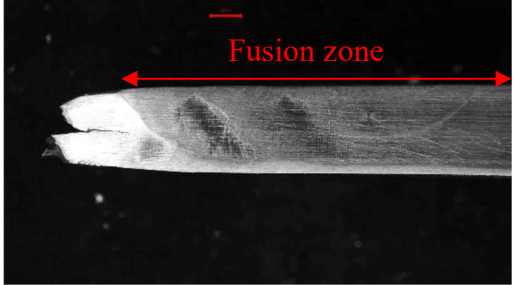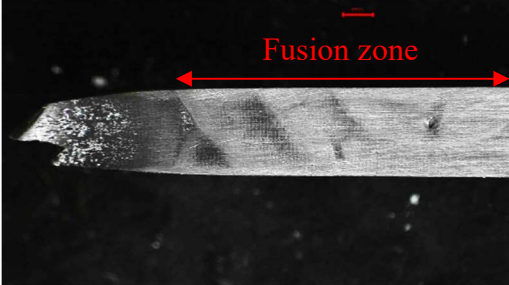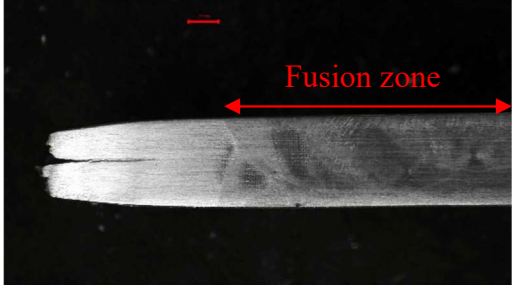
Yu, W. W., 2000. [Chapter 2:] Materials Used in Cold-Formed Steel Construction In: Cold-formed steel design. New York, USA: John Wiley & Sons, Pp. 39-70.

Macrographs of the fractured tensile specimens:

Fractured tensile specimens made of S700MC:

S700MC, $r/t = 0.5$; fractured from the bended base metal.	S700MC, $r/t = 1.0$; fractured from the bended base metal.
S700MC, $r/t = 1.5$; fractured from the bended base metal.	S700MC, $r/t = 2.0$; fractured from the virgin base material

Fractured tensile specimens made of S1100:

S1100, *r/t* = 3.0; fractured from the virgin base material	S1100, *r/t* = 3.25; fractured from the virgin base material
S1100, *r/t* = 3.5; fractured from the virgin base material	S1100, *r/t* = 3.75; fractured from the virgin base material
S1100, *r/t* = 4.6; fractured from the virgin base material	S1100, *r/t* = 5.0; fractured from the virgin base material